SCATTERING FROM A CHIRAL CYLINDER OF ARBITRARY CROSS-SECTION ABOVE A GROUND PLANE

A DISSERTATION SUBMITTED TO

THE GRADUATE SCHOOL OF

ENGINEERING AND NATURAL SCIENCES

OF ISTANBUL MEDIPOL UNIVERSITY

IN PARTIAL FULFILLMENT OF THE REQUIREMENTS FOR

THE DEGREE OF

DOCTOR OF PHILOSOPHY

IN

ELECTRICAL, ELECTRONICS ENGINEERING AND CYBER SYSTEMS

By

Ahsan Altaf

January, 2021

Scattering from a Chiral Cylinder of Arbitrary Cross-Section Above a Ground Plane
By Ahsan Altaf
January, 2021

We certify that we have read this dissertation and that in our opinion it is fully adequate, in scope and in quality, as a dissertation for the degree of Doctor of Philosophy.

Prof. Dr. Ercümend Arvas(Advisor)

Prof. Dr. Cengiz Özzaim (Co-Advisor)

Prof. Dr. Şehabeddin Taha Imeci

Prof. Dr. Fatih Erdoğan Sevılgen

Assoc. Prof. Dr. Hamid Torpi

Assoc. Prof. Dr. Mehmet Kemal Özdemir

Approved by the Graduate School of Engineering and Natural Sciences:

Assoc. Prof. Dr. Yasemin Yüksel Durmaz
Director of the Graduate School of Engineering and Natural Sciences

Foreword

The topic I have selected is a very special one. It has numerous benefits lying in the industrial sector as well as the defense sector in the form of warfare technology. The amount of specific knowledge, I have gained during the research on *chiral* materials especially the "*interaction of electromagnetic waves with chiral materials*" has undoubtedly elevated my theoretical knowledge in the field of electromagnetics. Moreover, learning a numerical method; the method of moments and then, applying it to solve electromagnetic scattering problems involving chiral materials has enhanced my skill set in terms of knowledge, computer programming, and hands-on experience in problem-solving. I expect that this topic will greatly contribute to the science and technology field in the future.

I believe no success is possible without the relentless support of your family and the people you love by your side. I have found solace in their understanding and patience during the research. The timely advice by my great supervisor and co-advisor have also ensured that I remain on track throughout the research. I am indebted to them for this achievement.

I hereby declare that all information in this document has been obtained and presented in accordance with academic rules and ethical conduct. I also declare that, as required by these rules and conduct, I have fully cited and referenced all material and results that are not original to this work.

Name, Last Name: AHSAN ALTAF

Signature :

Acknowledgement

No words will do justice to the amount of respect that I have for my supervisor Dr. Ercümend Arvas for gracing me with an opportunity that has turned a new leaf in my life and molded it for the better. I would like to express my deepest gratitude to him for believing in me during times when ambivalence prevailed, putting up with my follies with exemplary grace, and guiding me through the most fulfilling journey of my life. The knowledge exuded by him with his unique ability to provide meaningful solutions to persistent problems with his natural flair kept me motivated throughout the research.

I would like to express sincere gratitude to my co-supervisor Dr. Cengiz Özzaim for his guidance throughout the thesis. His command over the subject is unparalleled. He took a keen interest in my research and provided great advice that wrinkled out a few research limitations.

It is with extreme sorrow that I salute my late Baba, Altaf Hussain who couldn't see me through this journey. Although, I lost him during the way but hope that he is watching upon me with utmost pride. I can never forget the fighting spirit he instilled in me.

I am obliged to Dr. Serhend Arvas for providing smart key solutions to most of my problems. I couldn't have found a better mentor than him. His calm demeanor and relentless attention were inspiring and helped me focus. I can never thank him enough for all his friendship, guidance, and support.

I would like to thank the members of my dissertation committee, Professors Mehmet Kemal Özdemir, Hamid Torpi, Şehabeddin Taha Imeci, and Fatih Erdoğan Sevılgen.

I express my heartfelt thanks to all my professors at Medipol University. Throughout my doctoral studies, all the staff members were extremely cooperative.

Lastly, the blessings of my mother and mother-in-law allayed the nights of doubts and fear. I will forever be indebted to them for all their care, love, and support. I would also like to thank my wife Madiha and daughter Aabish for all the encouragement and support during these years. For them to allow me space and time to grow was an inexplicable blessing.

To my wife Madiha ...

Contents

List of Figures

List of Tables

List of Symbols

ϵ_0	Free-space permittivity
ϵ_r	Relative dielectric permittivity
ϵ	Dielectric permittivity
η_0	Free-space impedance
η	Impedance
γ	Chiral admittance
$\hat{a}_\phi$	Unit vector in the phi-direction
$\hat{t}_n$	Unit vector in the lateral-direction
$\hat{z}$	Unit vector in the z-direction
λ_0	Free-space wavelength
λ	Wavelength
$\mathbf{A}$	Magnetic potential
$\mathbf{B}$	Magnetic flux density
$\mathbf{D}$	Electric flux density
$\mathbf{E}$	Electric field
$\mathbf{F}$	Electric potential
$\mathbf{H}$	Magnetic field

$\mathbf{J}$	Electric surface current
$\mathbf{M}$	Magnetic surface current
$\mathrm{E_x}$	x-component of the electric field
$\mathrm{E_y}$	y-component of the electric field
$\mathrm{E_z}$	z-component of the electric field
$\mathrm{H_x}$	x-component of the magnetic field
$\mathrm{H_y}$	y-component of the magnetic field
$\mathrm{H_z}$	z-component of the magnetic field
$\mathrm{J_L}$	Lateral component of electric surface current
$\mathrm{J_z}$	Longitudinal component of electric surface current
L	Side length
$\mathrm{M_L}$	Lateral component of magnetic surface current
$\mathrm{M_z}$	Longitudinal component of magnetic surface current
P	Unit pulse function
$\tan\delta_e$	Electric loss tangent
$\tan\delta_m$	Magnetic loss tangent
μ_0	Free-space permeability
μ_r	Relative permeability
μ	Magnetic permeability
∇	nabla
Ω	Ohm
ω	Angular Frequency

ϕ	phi
C	Contour
d	Distance
f	Frequency
$H_0^{(2)}$	Hankel function of zeroth order and second kind
$H_1^{(2)}$	Hankel function of first order and second kind
h_1	Wave number for RHCP
h_2	Wave number for LHCP
k_0	Free-space wavenumber
k	Wavenumber
log	logarithmic
l	Length
m	meter
r	Radius
S	Surface
V	volt

Abbreviations

PEC	Perfect Electric Conductor
2D	Two-Dimensional
3D	Three-Dimensional
EM	Electromagnetic
MoM	Method of Moments
TM	Transverse Magnetic
TE	Transverse Electric
ind	induced
RCS	Radar Cross-Section
EFIE	Electric Field Integral Equation
RHCP	right-hand circularly polarized
LHCP	left-hand circularly polarized
GHz	Gigahertz
MHz	Megahertz
BIE	Boundary Integral Equations
MATLAB	matrix laboratory
inc	incident
tan	tangential

ÖZET

MÜKEMMEL İLETKEN BİR YER DÜZLEMİNİN ÜZERİNDE KEYFİ KESİTE SAHİP KIRAL BİR SİLİNDİRDEN SAÇILMA

Ahsan Altaf
Elektrik-Elektronik Mühendisliği ve Siber Sistemler, Doktora
Tez Danışmanı: Prof. Dr. Ercümend Arvas
Tez Eş Danışmanı: Prof. Dr. Cengiz Özzaim
Ocak, 2021

Bu tezde, mükemmel iletken (PEC) bir yer düzleminin üzerinde keyfi enine kesite sahip kiral bir silindirden saçılma problemi için basit, doğru ve etkili bir çözüm sunulmuştur. Hem TM hem de TE uyarımları dikkate alınmıştır. PEC düzlemi üzerindeki bu nesnenin görüntüsü biliniyorsa, bu nesneden saçılma problemi prensip olarak görüntü yöntemiyle çözülebilir. Bu nedenle, görüntü metodu kullanılarak, PEC bir düzleminin üzerindeki bir silindirden saçılma problemi, serbest uzayda iki farklı kiral silindirden saçılma problemine indirgenir. Bu iki silindirli problemden üç farklı eşdeğer problem elde etmek için yüzey denklik prensipleri kullanılır. Daha sonra bu eşdeğer problemleri sayısal olarak çözmek için moment metodu kullanılır. Bu iki silindirli problem için moment matrisi gereksiz yere büyüktür.

Kiral bir cismin PEC bir zemin üzerindeki görüntüsünün, aynı elektrik ve manyetik geçirgenliğe ancak zıt kiraliteye sahip başka bir kiral cisim olduğu bilinmektedir. Bu özelliği kullanarak, görüntü yöntemindeki iki farklı cisim problemi, karmaşık bir moment matrisi ile tek cisim problemine indirgenebilir. Bu prosedür, Geliştirilmiş Moment Matrisi olarak adlandırılır.

Kiral bir cismin görüntüsünün özelliğini doğrulamak için, ilk olarak üç kanonik problem tam olarak analitik tekniklerle çözülmüştür. Bir PEC düzleminin üzerindeki kiral cismin görüntüsünün aynı elektrik ve manyetik geçirgenliğe sahip kiral bir cisim olduğu doğrulanmıştır. Bununla birlikte, kiral cismin görüntüsünün kiralitesi, orijinal cismin kiralitesinin eksi işaretlisidir.

Hesaplanan sayısal sonuçlar, saçılan alanları ve silindir üzerindeki eşdeğer yüzey akımlarını içermektedir. Kiralitenin saçılan alanlar üzerindeki etkisini incelemek için çeşitli parametrik analizler yapılmıştır. Ayrıca, önerilen formülasyonun bazı avantajları ve dezavantajları ve bunların çözümleri kısaca

tartışılmıştır.

Anahtar sözcükler: Kiral cismin görüntüsü, moment methodu, iletken düzlem üzerindeki kiral cisimden saçılma.

ABSTRACT

SCATTERING FROM A CHIRAL CYLINDER OF ARBITRARY CROSS-SECTION ABOVE A GROUND PLANE

Ahsan Altaf
Ph.D. in Electrical, Electronics Engineering and Cyber Systems
Advisor: Prof. Dr. Ercümend Arvas
Co-Advisor: Prof. Dr. Cengiz Özzaim
January, 2021

In this dissertation, a simple, accurate, and efficient solution is presented for the problem of scattering from a chiral cylinder of arbitrary cross-section above a ground plane. Both TM and TE excitations are considered. In theory, scattering from an object above a perfectly conducting (PEC) plane can be found in principle if the image of this object through the PEC is known. Hence, using image theory, the problem of scattering from a cylinder above a PEC plane is reduced to two chiral cylinders in free-space. The surface equivalence principle is used to obtain three different equivalent problems for this two-cylinder problem. Then, the method of moments is used to solve these equivalent problems numerically. The moment matrix for this two-cylinder problem is unnecessarily large.

It is known that the image of a chiral body through a ground plane is another chiral body with the same permittivity and permeability but opposite chirality. Using this property, the two-body problem in the image method may be reduced to a one-body problem with a complicated moment matrix. This procedure is named the Enhanced Moment Matrix.

To verify the property of the image of a chiral body, first, three canonical problems are solved exactly using analytical techniques. It is verified that the image of a chiral body above a PEC plane is a chiral body with the same permittivity and permeability. However, the real chiral admittance of the image body is negative of the chiral admittance of the original body.

Computed numerical results include scattered fields and equivalent surface currents on the cylinder. Various parametric analyses are conducted to study the effect of chirality admittance on the scattered fields. Furthermore, some advantages and drawbacks for the proposed formulation and their solutions are briefly discussed.

Keywords: Image of chiral material, moments method, scattering from chiral cylinders above a ground plane.

Chapter 1

Introduction

1.1 The Purpose

The main purpose of this work is to solve the problem of electromagnetic scattering from a two dimensional (2-D) homogeneous chiral cylinder of arbitrary cross-section above an infinite perfect electric conducting (PEC) plane. The scattering behavior of a chiral cylinder above a PEC plane can be very different than the scattering behavior in free-space. Therefore, a detailed numerical study is required in order to understand the electromagnetic (EM) waves interaction with such materials. In this work, first, using image theory, the original problem is reduced to two chiral cylinders in free-space. The method of moments (MoM) is used to solve this equivalent problem numerically. It is known that the image of a chiral body through a ground plane is another chiral body with the same permittivity and permeability but opposite chirality. Using this property, the two-body problem in the method of images method may be reduced to a one-body problem with a complicated moment matrix. This procedure is named as Enhanced Moment Matrix. Both TM and TE plane wave excitations are considered. Computed numerical results include scattered fields and equivalent surface currents on the cylinder. The results obtained by the enhanced moment matrix procedure are in excellent agreement with those obtained by the method

of images.

To verify the property of the image of a chiral body, first, three canonical problems are solved exactly using analytical techniques, and for the sake of completeness, a brief summary of plane waves in an unbounded chiral medium is also given.

1.2 The Motivation

The term *chiral* is derived from the Greek word *cheir* meaning "hand" and chirality refers to handedness. Chirality or handedness is an in-ability of an object into alignment with its mirror images through rotation and/or translation. From atoms to human beings, chirality can be found across a variety of organic or biological substances. Golf clubs, helices, and gloves are examples of man-made chiral objects while butterfly wings, snails, proteins, and amino acids are natural chiral bodies. Chirality provides an extra degree of freedom. The positive chirality ($\gamma > 0$) specifies right-handedness while the negative chirality ($\gamma < 0$) defines left-handedness. When chirality is zero ($\gamma = 0$), the medium is simply dielectric or achiral.

In a chiral medium, the uniform plane wave cannot be linearly or elliptically polarized. It has to be circularly polarized. Within a chiral medium, this circularly polarized wave is divided into two waves of opposite handedness. These waves have different wave numbers, unequal phase velocity, and different attenuation rates. Outside the body, these waves combine to form a linearly polarized wave. In other words, the fields scattered by a chiral body have coupled TM and TE components.

Electromagnetic scattering by different materials such as conductors, dielectrics, chiral, and open cavities have been addressed by many researchers in the applied mathematical and engineering communities. Knowledge about the fields scattered by a chiral material in the far-field region is important for many

applications in the defense and industrial sectors. Chiral materials have been studied extensively over the last couple of decades and are still being analyzed in different scenarios due to their attractive properties. Over the last half-century, chiral media have been extensively investigated by many researchers. However, the problem of scattering from a chiral cylinder of arbitrary cross-section above a perfectly conducting ground plane has not been solved. In order to further study on chiral materials and their applications, it is important to study the work done by other researchers. Given below is a brief summary of the previous studies.

The optical activity was first observed during the early studies of propagation of light through optically active bodies [1] in 18^{th} century. The optical activity phenomenon in quartz plates was discovered by Biot [2–5]. He demonstrated that the optical activity depends on the thickness of the quartz plates and it can be removed by combining two plates of the same thickness but opposite handedness. From Biot's experiments, Pateur [6] concluded that the atoms are arranged in an asymmetrical order in the chiral medium. In other words, it is related to an unbalance of the right- and left-handed molecules in the medium. This is where the electromagnetic chirality saga begins.

Wave interaction with chiral objects was studied for the first time by Karl F. Lindman in $1920-22$ and Pickering in 1945. Lindman used helices to demonstrate the phenomenon of optical activity in the microwave (1-3 GHz) regime. Through his experiment, he concluded that the angle of rotation of a wave depends upon the number of helices within a medium, and the optical activity can be made absent by using an equal number of opposite handedness helices [7, 8]. Lindman compared his results with an existing optical model, and his work is summarized in [9]. Later, his work was experimentally proved by Winkler [10], and Tinoco and Freeman [11].

In the second half of the 19^{th} century, Drude established the constitutive relations for chiral objects [12]. However, the modern history of electromagnetic chirality dates to 1979, when Jaggard presented a macroscopic model of helices-loaded material and proposed theory to describe the chemistry between electromagnetic waves and chiral structures [13]. The next study on chirality

appeared in 1982 by Engheta and Mickelson [14], where they considered transition radiation from a chiral plate. In 1986, Silverman studied scattering from chiral/achiral interfaces [15]. From 1986 to 1990, Lakhtakia worked on scattering from chiral and achiral interfaces in [16–18]. The same authors also studied scattering by mirror-conjugated chiral interface and scattering by a periodic chiral/achiral interface in [19, 20]. Similarly, scattering from chiral slabs and infinitely backed chiral materials have also been presented in [21–26]. These studies helped in demonstrating scattering from flat surfaces, but the practical problems are more complex which demanded further investigations.

Objects of cylindrical and spherical shapes are encountered frequently in EM problems, which led to Bohren's research on problems involving scattering from homogeneous spheres [27], spherical shells [28], and cylinders [29]. He solved these problems using eigenfunction solutions. Varadan investigated the eigenmodes of a chiral coated conducting sphere in order to explore the practical aspects of chiral media [30]. In a similar study, Latktakia *et al*. demonstrated a microwave resonator by studying a chiral filled conducting sphere [31]. Varadan and other researchers presented different techniques to construct an artificial chiral object [32–37]. Kluskens and Newman [38,39] extended Bohren's work, and presented a method of moments solution of problems involving single layer and multilayer chiral cylinders using volume equivalence principle. Engheta and Jaggard presented constitutive relations for different models of chiral media [40,41]. They studied reflection, transmission, and refraction of an electromagnetic wave from finite and infinite chiral mediums. In-addition, radiation problems from a point and distributed sources in an infinite chiral medium were also investigated [42,43]. Alkanhal [44] presented the method of moment solution for a chiral cylinder using the surface equivalence principle. The scattering behavior of a chiral coated conducting cylinder is studied by Buber et al [45]. A method of moment solution of 3-dimensional chiral body of arbitrary cross-section is solved by Worasawate [46], and Yuceer [47] used the same method to study scattering by a chiral body of revolution.

Achiral bodies above a ground plane are investigated by many researchers. Valle [48] and Madrazo [49] used the extinction theorem to find electromagnetic

scattering from a conducting cylinder above a PEC plane. A conducting body of an arbitrary cross-section above a conducting half-plane, excited by TM or TE wave is extensively studied [50–53].

Chao [54] solved a dielectric sphere above a perfectly conducting plane using Boundary Integral Equation (BIE) with modified Greens functions. Gorden and Ngo [55] solved a cylinder above a lossy half-space. They investigated a quartz fiber on an aluminum substrate and results were verified with the experimental results. In a similar study, Borghi [56] used a cylindrical wave approach to solve a conducting cylinder above a half-space. Wang [57] and Lee [58, 59] used hybrid techniques to solve cylindrical objects above a conducting surface. In [60], Kizilay presented a decomposition method solution of a conducting body above an infinite periodic surface. Most recently, Cengiz [61, 62] presented a method of moment solution for a dielectric body above a perfectly conducting plane and a perfectly conducting body above a lossy half-space using the perturbation method.

The above-mentioned studies gave an insight into the scattering behavior of conducting and dielectric materials above a ground plane. The reason behind studying chiral material case separately is that the scattering behavior of chiral objects cannot be predicted by the simple theory as one can predict for conducting and/or dielectric materials.

The plane wave scattering from a 2D and 3D chiral object is solved by Alkanhal [44] and Worasawate [46], respectively. They used surface equivalence principle and method of moments. These studies show that this method can be used effectively to solve a chiral body above a PEC plane. Therefore, in this work, we will use the same procedure as discussed in the above two studies to solve the problem of scattering from a chiral cylinder above a ground plane.

Despite the immense amount of research on chiral materials the case of a chiral body of arbitrary cross-section above a perfectly conducting ground plane has not been investigated, which is the proposed topic. This study is very important for variety of applications in the semiconductor industry such as contamination of particles on the surfaces of the optical systems [63, 64], design

of optical launchers for the plasma waves [65, 66], analysis of optical microscopy procedures [67–69], solar light and/or photodetectors in photo-voltics [70–74], electromagnetic interference [75, 76], and chemical sensing [77]. This study also has vast applications in monitoring mirror contamination in the optical systems, which not only degrades the systems' performance but also causes local heating. Therefore, it is reasonable to study chiral material placed near the ground plane and observe the behavior of different quantities such as the induced surface currents on the cylinder and the resulting scattered fields.

1.3 The Solution Method

In this dissertation, the formulation is based on the surface equivalence principle [78, Chapter 2]. In the surface equivalence principle, the region of interest is replaced by a surface with some appropriate equivalent surface currents placed on the boundary of the region. These equivalent surface currents radiate in an unbounded medium with the material parameters of the region of interest. By satisfying the continuity of the tangential components of the fields, a set of coupled integral equations is obtained. Then using MoM, these integral equations are transformed into a matrix equation. The right-hand side of this matrix equation contains the incident field and the column vector of the unknowns determines the equivalent surface currents. Once the currents are known, then the other parameters like bi-static radar cross-section, near-fields, and currents on the cylinder can be found easily.

1.4 The Structure of the Dissertation

In Chapter 2, image theory for chiral materials is developed. Unlike conductors and dielectrics, the image of the chiral material is not the same as the original [79]. Therefore, it is presented that the image of a chiral body above a PEC plane is a chiral body with the same permittivity (ϵ) and permeability (μ). However, the

real chiral admittance (γ) of the image body is negative of the chiral admittance of the original body. This is verified by using three simple examples. These examples are first solved exactly by finding the reflected and/or transmitted fields using analytical techniques. Then the image theory is used to remove the PEC and again the reflected and/or transmitted fields are found exactly using analytical techniques. The source in these examples is an infinite surface current sheet parallel to the ground plane.

In Chapter 3, image theory developed in the previous chapter is used to solve the problem of scattering from a chiral cylinder of arbitrary cross-section above a ground plane numerically by using two different procedures, i.e.

1. Method of Images
2. Enhanced Moment Matrix Method

In the method of images, the image theory is used and the original problem is reduced to a two-cylinder problem in free-space. In other words, it is a two-body problem with two external sources. However, the resulting moment matrix is unnecessarily large. Therefore, the properties of the image body and the image source are used to reduce the size of the moment matrix. Using image theory, the two-body problem in the image method may be reduced to a one-body problem with a complicated moment matrix. This procedure is named the Enhanced Moment Matrix. A general MoM solution method is also explained in this chapter.

In Chapter 4, the numerical results obtained from the formulation discussed in Chapter 3 are presented. The computed results are presented for the cylinder of different cross-sections, material parameters, the polarization of the incident waves, and incident angles. The computed results include currents on the cylinder and the scattered field in the near- and far-regions.

Chapter 4 contains a brief summary of this work.

Chapter 2

Image of Chiral Material

In this chapter, the image theory for a chiral material is presented. Three examples are solved exactly. These examples have two purposes. First, they are applications of the theory of plane waves given in Appendix A. The reflection and the transmission of plane waves at interfaces involving chiral and non-chiral materials are introduced. The second and the more important purpose is to verify that the image of a lossless chiral body has a real chirality equal to the negative of the chirality of the original chiral body.

In [79], it is proven, by using the volume equivalence principle, that the image of a chiral body above a PEC plane is a chiral body with the same permittivity (ϵ) and permeability (μ). However, the real chiral admittance (γ_2) of the image body is negative of the chiral admittance (γ_1) of the original body. The purpose here is to verify this, by solving three canonical problems. These problems are solved exactly by analytical means. In other words, these problems are first solved exactly by finding the reflected and/or transmitted fields using analytical techniques. Then the image theory is used to remove the PEC and again the reflected and/or transmitted fields are found exactly using analytical techniques. The source in these examples is an infinite surface current sheet parallel to the ground plane.

The first problem is shown in Fig. 2.1. Here, the infinite electric current sheet $\mathbf{J}_1$ is at $z = -d$ and is inside a chiral half-space ($z < 0$). The currents sheet is radiating in a chiral half-space bounded by a PEC plane. The PEC occupies the $z = 0$ plane. The chiral material has parameters $(\epsilon, \mu, \gamma_1)$. It is shown that this problem is equivalent to the one shown in Fig. 2.2 for $z \leq 0$ when γ_2 is equal to $-\gamma_1$, and $\mathbf{J}_2$ (at $z = +d$) is negative of $\mathbf{J}_1$.

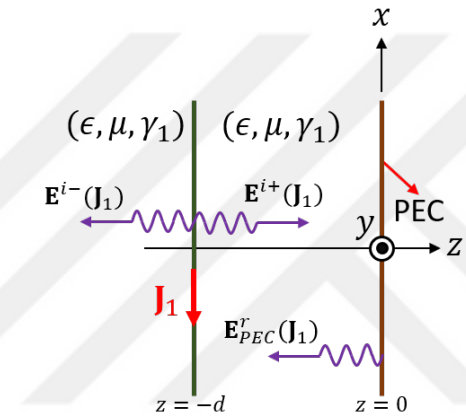

Figure 2.1: An infinite current sheet (in a chiral half-space) parallel to a PEC plane.

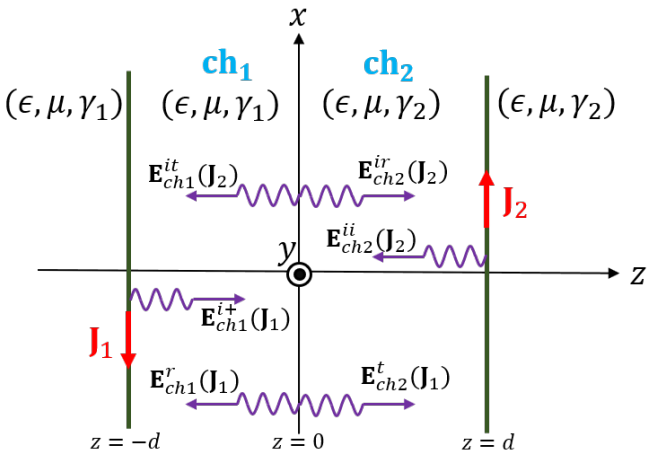

Figure 2.2: The field for $z \leq 0$ here are equal to the field in Fig. 2.1 when γ_2 and $\mathbf{J}_2$ are properly chosen.

The second problem shown in Fig. 2.3 includes a grounded chiral slab of

thickness t. The source in this problem is the current sheet $\mathbf{J}_1$ and is placed in a regular dielectric (ϵ, μ) outside the chiral slab. It is shown that this problem is equivalent to the one shown in Fig. 2.4 (for $z \leq 0$) if γ_2 is $-\gamma_1$ and $\mathbf{J}_2$ is $-\mathbf{J}_1$.

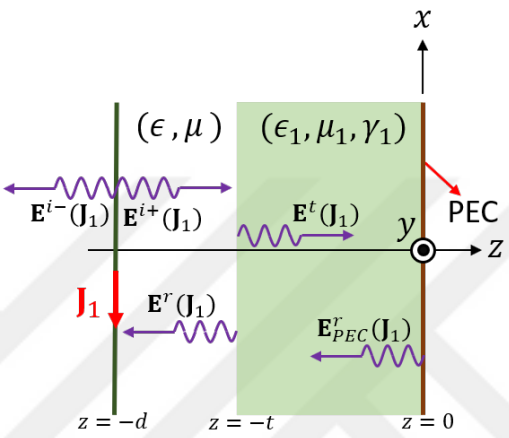

Figure 2.3: Grounded chiral slab excited by a current sheet $\mathbf{J}_1$.

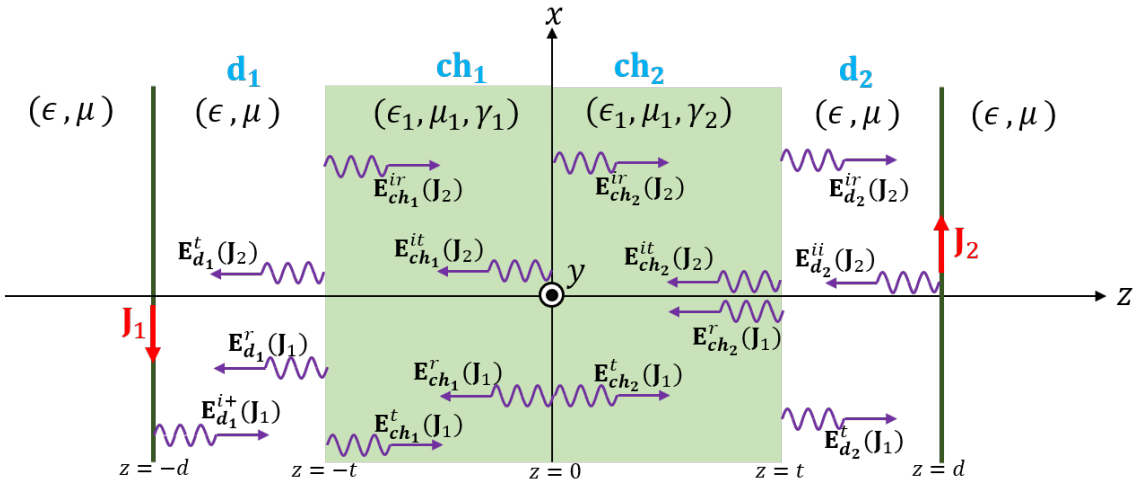

Figure 2.4: The field for $z \leq 0$ here are equal to the field in Fig. 2.3 when γ_2 and $\mathbf{J}_2$ are properly chosen.

In the third problem shown in Fig. 2.5 the chiral slab is not grounded. The chiral slab is placed between the source $\mathbf{J}_1$ and the PEC plane. It is shown that this problem is equivalent to the one in Fig. 2.6 if γ_2 is $-\gamma_1$ and $\mathbf{J}_2$ is $-\mathbf{J}_1$.

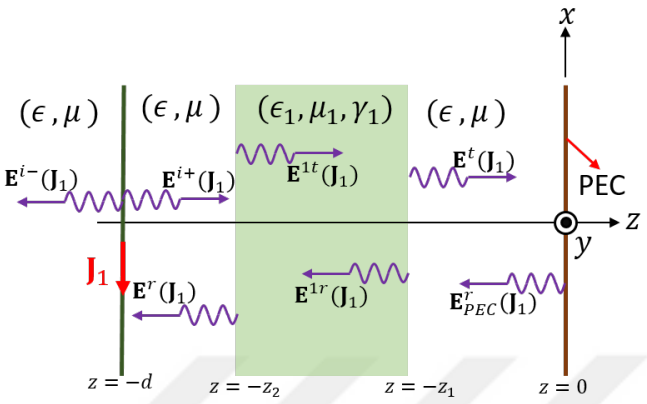

Figure 2.5: A chiral slab parallel to a PEC plane and excited by a current sheet $\mathbf{J}_1$.

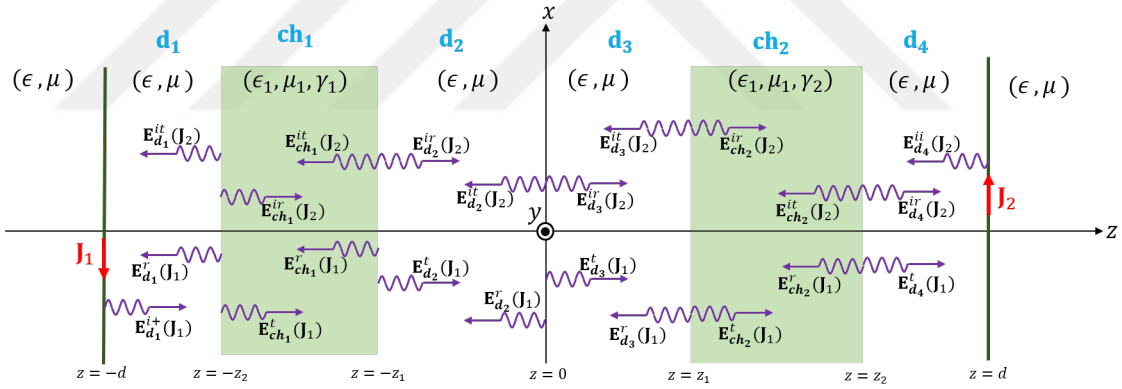

Figure 2.6: The field for $z \leq 0$ here are equal to the field in Fig. 2.5 when γ_2 and $\mathbf{J}_2$ are properly chosen.

The above three problems are solved exactly. Before solving these problems, a brief summary of results for plane waves in an unbounded chiral medium are given in Appendix A. For details and much more the reader is referred to elegant papers [80–82].

2.1 Example-1

2.1.1 The Original Problem

In this section, the problem shown in Fig. 2.1 is considered. Here, a current sheet carrying a surface current $\mathbf{J}_1$ is placed in a chiral medium at a distance d away from a PEC plane. The chiral medium, region $z < 0$, is characterized by $(\epsilon, \mu, \gamma_1)$ where ϵ is permittivity, μ is permeability, and γ_1 is chiral admittance of the medium. If the surface current $\mathbf{J}_1$ is defined as

$$\mathbf{J}_1 = -4J_0\hat{x} \tag{2.1}$$

Then the incident field produced by this current for region $z < -d$ is given by

$$\mathbf{E}^{i-}(\mathbf{J}_1) = \eta_{c_1} J_0 \Big\{ (\hat{x} + j\hat{y}) e^{jh_1(z+d)} + (\hat{x} - j\hat{y}) e^{jh_2(z+d)} \Big\} \tag{2.2}$$

$$\mathbf{H}^{i-}(\mathbf{J}_1) = J_0 \Big\{ (-\hat{y} + j\hat{x}) e^{jh_1(z+d)} + (-\hat{y} - j\hat{x}) e^{jh_2(z+d)} \Big\} \tag{2.3}$$

Where,

$$h_1 = \omega\mu\gamma_1 + \sqrt{k^2 + (\omega\mu\gamma_1)^2} \tag{2.4}$$

$$h_2 = -\omega\mu\gamma_1 + \sqrt{k^2 + (\omega\mu\gamma_1)^2} \tag{2.5}$$

$$\eta_{c_1} = \frac{\eta}{\sqrt{1 + (\eta\gamma_1)^2}} \tag{2.6}$$

The superscript $i-$ represents the incident field traveling in $-z$ direction.

Similarly, the incident field produced by $\mathbf{J}_1$ for region $z > -d$ can be written as follows.

$$\mathbf{E}^{i+}(\mathbf{J}_1) = \eta_{c_1} J_0 \Big\{ (\hat{x} - j\hat{y}) e^{-jh_1(z+d)} + (\hat{x} + j\hat{y}) e^{-jh_2(z+d)} \Big\} \tag{2.7}$$

$$\mathbf{H}^{i+}(\mathbf{J}_1) = J_0 \Big\{ (\hat{y} + j\hat{x}) e^{-jh_1(z+d)} + (\hat{y} - j\hat{x}) e^{-jh_2(z+d)} \Big\} \tag{2.8}$$

Note that,

$$\mathbf{E}^{i+}(\mathbf{J}_1) = \mathbf{E}^{i-}(\mathbf{J}_1) \quad at \quad z = -d, \tag{2.9}$$

and

$$\hat{z} \times [\mathbf{H}^{i+}(\mathbf{J}_1) - \mathbf{H}^{i-}(\mathbf{J}_1)] = \mathbf{J}_1 \quad at \quad z = -d. \tag{2.10}$$

The reflected field can be written as follow.

$$\mathbf{E}^r_{PEC}(\mathbf{J}_1) = \eta_{c_1} J_0 \Big\{ a(\hat{x} + j\hat{y}) e^{jh_1 z} + b(\hat{x} - j\hat{y}) e^{jh_2 z} \Big\} \tag{2.11}$$

$$\mathbf{H}^r_{PEC}(\mathbf{J}_1) = J_0 \Big\{ a(-\hat{y} + j\hat{x}) e^{jh_1 z} + b(-\hat{y} - j\hat{x}) e^{jh_2 z} \Big\}. \tag{2.12}$$

Here, a and b are constants to be determined, and the superscript r represents reflected field. The argument $\mathbf{J}_1$ is used in (2.11) and (2.12) to remind us that these fields are reflections of the incident fields produced by $\mathbf{J}_1$. The subscript PEC is used to remind us that the field is being reflected from the PEC plane.

The total electric field (the sum of (2.7) and (2.11)) must be zero at $z = 0$. This gives

$$a = -e^{-jh_2 d} \quad , \quad b = -e^{-jh_1 d} \tag{2.13}$$

Thus, the reflected field is given by

$$\mathbf{E}^r_{PEC}(\mathbf{J}_1) = \eta_{c_1} J_0 \Big\{ -e^{-jh_2 d}(\hat{x} + j\hat{y}) e^{jh_1 z} - e^{-jh_1 d}(\hat{x} - j\hat{y}) e^{jh_2 z} \Big\} \tag{2.14}$$

and

$$\mathbf{H}^r_{PEC}(\mathbf{J}_1) = J_0 \Big\{ -e^{-jh_2 d}(-\hat{y} + j\hat{x}) e^{jh_1 z} - e^{-jh_1 d}(-\hat{y} - j\hat{x}) e^{jh_2 z} \Big\}. \tag{2.15}$$

The induced surface current on the conductor is given by

$$\mathbf{J}^{ind} = -\hat{z} \times \mathbf{H}^T \Big|_{z=0} \tag{2.16}$$

where, $\mathbf{H}^T$ is total magnetic field. Using (2.8) and (2.15) $\mathbf{J}^{ind}$ is found to be

$$\mathbf{J}^{ind} = 2J_0 \Big\{ \hat{x} \big[e^{-jh_1 d} + e^{-jh_2 d} \big] - j\hat{y} \big[e^{-jh_1 d} - e^{-jh_2 d} \big] \Big\}. \tag{2.17}$$

Note that the reflected field given by (2.14) and (2.15) is the same as the field produced by $\mathbf{J}^{ind}$ in an unbounded chiral medium $(\epsilon, \mu, \gamma_1)$.

2.1.2 The Equivalent Image Problem

To use image theory, the ground plane in Fig. 2.1 is removed and the half-space $z > 0$ is filled with an "image" material $(\epsilon, \mu, \gamma_2)$ and an image source $\mathbf{J}_2 = -\mathbf{J}_1$ is placed at $z = +d$. The resulting problem is shown in Fig. 2.2. The incident field produced by the image current $\mathbf{J}_2$ in the region $z < d$ is given by

$$\mathbf{E}^{ii}_{ch_2}(\mathbf{J}_2) = \eta_{c_2} J_0 \Big\{ (-\hat{x} - j\hat{y}) e^{jh_3(z-d)} + (-\hat{x} + j\hat{y}) e^{jh_4(z-d)} \Big\} \tag{2.18}$$

$$\mathbf{H}^{ii}_{ch_2}(\mathbf{J}_2) = J_0 \Big\{ (\hat{y} - j\hat{x}) e^{jh_3(z-d)} + (\hat{y} + j\hat{x}) e^{jh_4(z-d)} \Big\} \tag{2.19}$$

The superscript ii represents the incident field produced by the image source $\mathbf{J}_2$. Here, h_3 and h_4 are the right- and left-handed wave numbers, and η_{c_2} is the wave impedance for the chiral material $(\epsilon, \mu, \gamma_2)$ given by

$$h_3 = \omega\mu\gamma_2 + \sqrt{k^2 + (\omega\mu\gamma_2)^2} \tag{2.20}$$

$$h_4 = -\omega\mu\gamma_2 + \sqrt{k^2 + (\omega\mu\gamma_2)^2} \tag{2.21}$$

$$\eta_{c_2} = \frac{\eta}{\sqrt{1 + (\eta\gamma_2)^2}} \tag{2.22}$$

In Fig. 2.2, $\mathbf{E}^r_{ch_1}(\mathbf{J}_1)$ and $\mathbf{E}^t_{ch_2}(\mathbf{J}_1)$ represent the fields reflected and transmitted at the interface at $z = 0$. This interface is between two chiral half-spaces $(\epsilon, \mu, \gamma_1)$ and $(\epsilon, \mu, \gamma_2)$. The subscript ch_1 is used to remind us that the field exists in region ch_1 while the subscript ch_2 is used to remind us that the field exists in region ch_2. The source of these waves are assumed to be $\mathbf{J}_1$. Similarly, $\mathbf{E}^{ir}_{ch_2}(\mathbf{J}_2)$ and $\mathbf{E}^{it}_{ch_1}(\mathbf{J}_2)$ represent the fields reflected and transmitted at the interface at $z = 0$. The source of these waves are assumed to be the image source $\mathbf{J}_2$. The image problem in Fig. 2.2 will be correct only if the reflected field $\mathbf{E}^r_{PEC}(\mathbf{J}_1)$ in Fig. 2.1 is equal to the sum of the reflected field $\mathbf{E}^r_{ch_1}(\mathbf{J}_1)$ and the transmitted field $\mathbf{E}^{it}_{ch_1}(\mathbf{J}_2)$ in Fig. 2.2. If γ_2 is chosen to be the same as γ_1, then obviously the two reflected fields will be zero and h_1 will be equal to h_3 and h_2 will be equal to h_4. Then it is easy to see that the transmitted field $(\mathbf{E}^{it}_{ch_1}(\mathbf{J}_2), \mathbf{H}^{it}_{ch_1}(\mathbf{J}_2))$ (which is identical to $(\mathbf{E}^{ii}_{ch_2}(\mathbf{J}_2), \mathbf{H}^{ii}_{ch_2}(\mathbf{J}_2))$ given by ((2.18) and (2.19)) in Fig. 2.2 is not

the same as the field $(\mathbf{E}^r_{PEC}(\mathbf{J}_1), \mathbf{H}^r_{PEC}(\mathbf{J}_1))$ (given by (2.11) and (2.12)) in Fig. 2.1. Therefore, the image of a chiral material can not be itself.

Assuming $\gamma_2 \neq \gamma_1$, the fields in Fig. 2.2 can be found as follows. Let

$$\mathbf{E}^{ir}_{ch_2}(\mathbf{J}_2) = \eta_{c_2} J_0 \Big\{ a_1(-\hat{x} + j\hat{y}) e^{-jh_3 z} + a_2(-\hat{x} - j\hat{y}) e^{-jh_4 z} \Big\} \tag{2.23}$$

$$\mathbf{H}^{ir}_{ch_2}(\mathbf{J}_2) = J_0 \Big\{ a_1(-\hat{y} - j\hat{x}) e^{-jh_3 z} + a_2(-\hat{y} + j\hat{x}) e^{-jh_4 z} \Big\} \tag{2.24}$$

$$\mathbf{E}^{it}_{ch_1}(\mathbf{J}_2) = \eta_{c_1} J_0 \Big\{ a_3(-\hat{x} - j\hat{y}) e^{jh_1 z} + a_4(-\hat{x} + j\hat{y}) e^{jh_2 z} \Big\} \tag{2.25}$$

$$\mathbf{H}^{it}_{ch_1}(\mathbf{J}_2) = J_0 \Big\{ a_3(\hat{y} - j\hat{x}) e^{jh_1 z} + a_4(\hat{y} + j\hat{x}) e^{jh_2 z} \Big\} \tag{2.26}$$

$$\mathbf{E}^{i+}_{ch_1}(\mathbf{J}_1) = \eta_{c_1} J_0 \Big\{ (\hat{x} - j\hat{y}) e^{-jh_1(z+d)} + (\hat{x} + j\hat{y}) e^{-jh_2(z+d)} \Big\} \tag{2.27}$$

$$\mathbf{H}^{i+}_{ch_1}(\mathbf{J}_1) = J_0 \Big\{ (\hat{y} + j\hat{x}) e^{-jh_1(z+d)} + (\hat{y} - j\hat{x}) e^{-jh_2(z+d)} \Big\} \tag{2.28}$$

$$\mathbf{E}^{r}_{ch_1}(\mathbf{J}_1) = \eta_{c_1} J_0 \Big\{ a_5(\hat{x} + j\hat{y}) e^{jh_1 z} + a_6(\hat{x} - j\hat{y}) e^{jh_2 z} \Big\} \tag{2.29}$$

$$\mathbf{H}^{r}_{ch_1}(\mathbf{J}_1) = J_0 \Big\{ a_5(-\hat{y} + j\hat{x}) e^{jh_1 z} + a_6(-\hat{y} - j\hat{x}) e^{jh_2 z} \Big\} \tag{2.30}$$

$$\mathbf{E}^{t}_{ch_2}(\mathbf{J}_1) = \eta_{c_2} J_0 \Big\{ a_7(\hat{x} - j\hat{y}) e^{-jh_3 z} + a_8(\hat{x} + j\hat{y}) e^{-jh_4 z} \Big\} \tag{2.31}$$

$$\mathbf{H}^{t}_{ch_2}(\mathbf{J}_1) = J_0 \Big\{ a_7(\hat{y} + j\hat{x}) e^{-jh_3 z} + a_8(\hat{y} - j\hat{x}) e^{-jh_4 z} \Big\} \tag{2.32}$$

Where a_1 - a_8 are unknown constants to be found. By satisfying the boundary conditions at the interface $z = 0$, one can show that

$$a_1 = \frac{(\eta_{c_1} - \eta_{c_2})}{(\eta_{c_1} + \eta_{c_2})} e^{-jh_4 d}\,, a_2 = \frac{(\eta_{c_1} - \eta_{c_2})}{(\eta_{c_1} + \eta_{c_2})} e^{-jh_3 d}\,,$$

$$a_3 = \frac{2\eta_{c_2}}{(\eta_{c_1} + \eta_{c_2})} e^{-jh_3 d} \, , a_4 = \frac{2\eta_{c_2}}{(\eta_{c_1} + \eta_{c_2})} e^{-jh_4 d} \, ,$$

$$a_5 = \frac{(\eta_{c_2} - \eta_{c_1})}{(\eta_{c_1} + \eta_{c_2})} e^{-jh_2 d} \, , a_6 = \frac{(\eta_{c_2} - \eta_{c_1})}{(\eta_{c_1} + \eta_{c_2})} e^{-jh_1 d} \, ,$$

$$a_7 = \frac{2\eta_{c_1}}{(\eta_{c_1} + \eta_{c_2})} e^{-jh_1 d} \, , a_8 = \frac{2\eta_{c_1}}{(\eta_{c_1} + \eta_{c_2})} e^{-jh_2 d} \, .$$

A simpler problem of a plane wave incident on achiral/chiral interface has been solved in detail by many researchers [15–21,23–26,35,83]. The above eight results agree with those in the literature for the special case of normal incidence on such an interface.

Note that the wave impedance of a chiral medium does not change when its chiral admittance changes sign. Therefore, if $\gamma_2 = -\gamma_1$ then $\eta_{c_2} = \eta_{c_1}$ and the reflection coefficients a_1, a_2, a_5, and a_6 are zero. Remember that this was the case when $\gamma_2 = \gamma_1$ as well. Now however, h_3 will be equal to h_2 and h_4 will be equal to h_1. Then it is easy to see that the field $(\mathbf{E}^{it}_{ch_1}(\mathbf{J}_2), \mathbf{H}^{it}_{ch_1}(\mathbf{J}_2))$ (given by (2.25) and (2.26)) in Fig. 2.2, is the same as the field $(\mathbf{E}^{r}_{PEC}(\mathbf{J}_1), \mathbf{H}^{r}_{PEC}(\mathbf{J}_1))$ (given by (2.11) and (2.12)) in Fig. 2.1. Therefore, it is proved that the correct image material in Fig. 2.2 has the parameters $(\epsilon, \mu, -\gamma_1)$.

2.1.3 Fields Computation

To demonstrate the behavior of the electric and magnetic fields in various parts of the problems, we have computed the fields for a special case of $\mathrm{J}_0 = 1(A/m)$, $\epsilon_r = 2$, $\mu_r = 1$, $\gamma_1 = 0.005$, $d = 1$ meter, and $f = 300$ MHz. The computed results are shown in Figs. 2.7 - 2.14. Figure 2.7 shows the real part of x-component of the total electric field. There are three curves in this figure. It is seen that when $\gamma_2 = -\gamma_1$, the fields of the image problem are the same as the fields in the original problem. Where as, these two fields are not the same when $\gamma_2 = \gamma_1$. Note that

total E_y is not zero at $z = 0$ interface, when $\gamma_2 \neq -\gamma_1$. This is clear from Figs. 2.9 and 2.10. The other six figures (2.7, 2.8, 2.11 - 2.14) also support the conclusion that the image chiral material must have $\gamma_2 = -\gamma_1$.

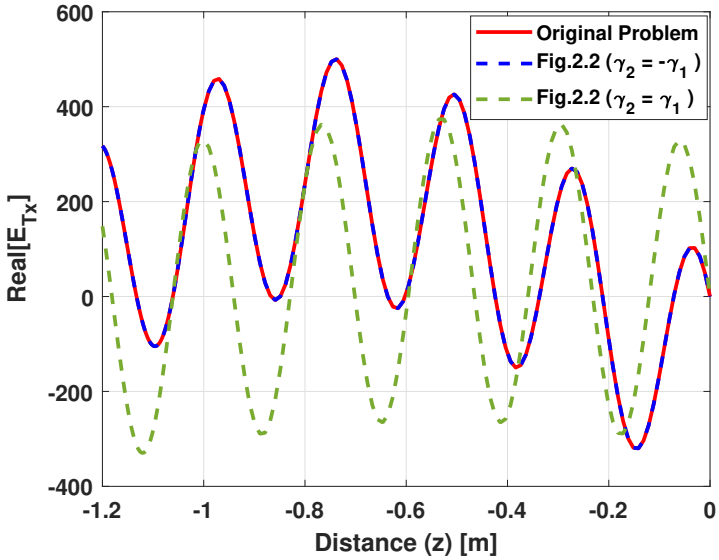

Figure 2.7: Real component of total E_x in Fig. 2.1 and Fig. 2.2 for a chiral-PEC interface problem.

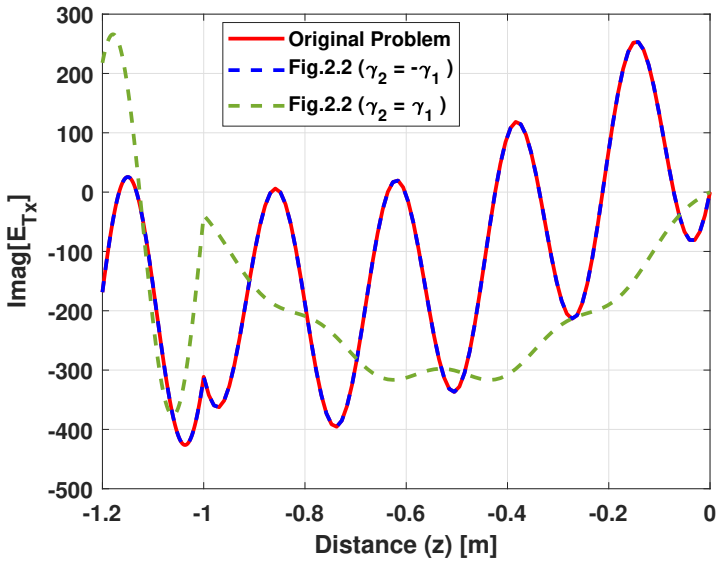

Figure 2.8: Imaginary component of total E_x in Fig. 2.1 and Fig. 2.2 for a chiral-PEC interface problem.

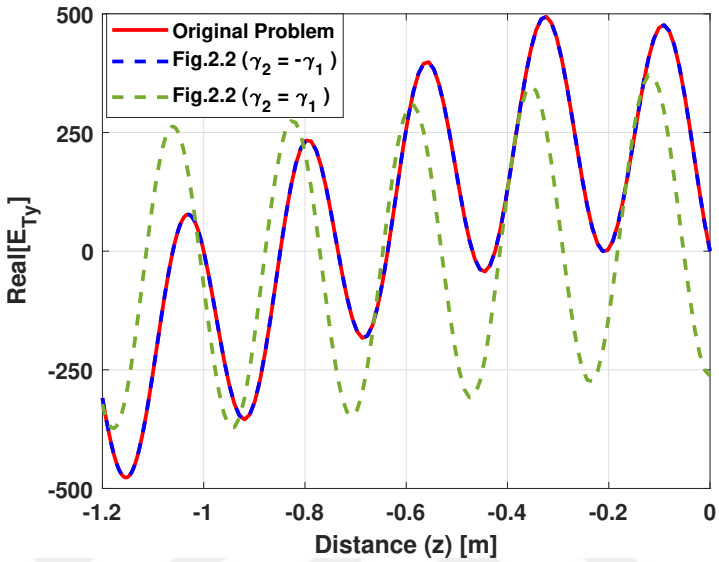

Figure 2.9: Real component of total E_y in Fig. 2.1 and Fig. 2.2 for a chiral-PEC interface problem.

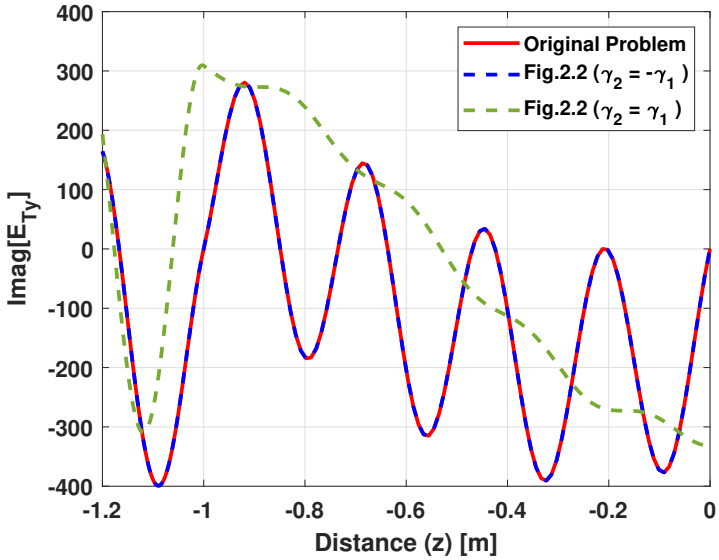

Figure 2.10: Imaginary component of total E_y in Fig. 2.1 and Fig. 2.2 for a chiral-PEC interface problem.

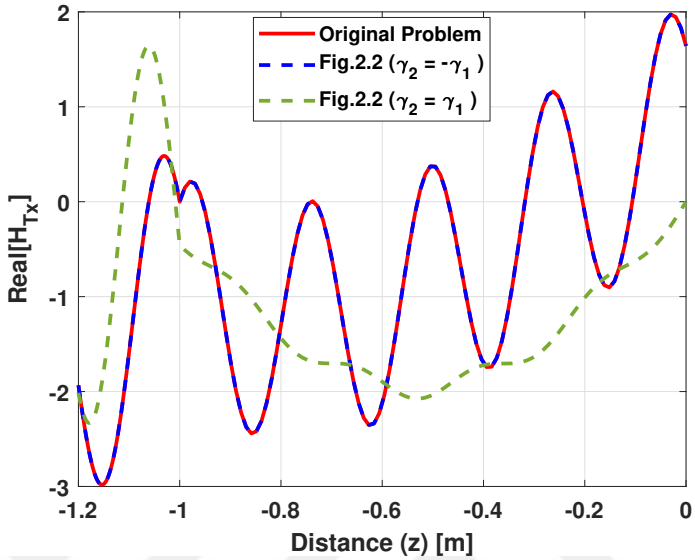

Figure 2.11: Real component of total H_x in Fig. 2.1 and Fig. 2.2 for a chiral-PEC interface problem.

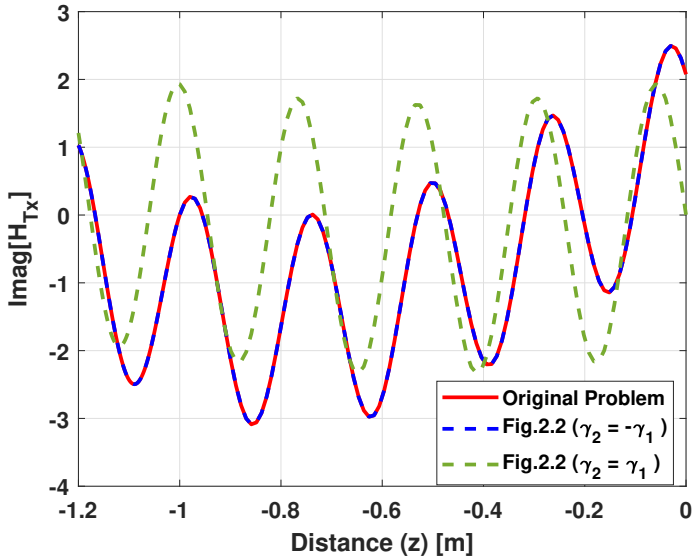

Figure 2.12: Imaginary component of total H_x in Fig. 2.1 and Fig. 2.2 for a chiral-PEC interface problem.

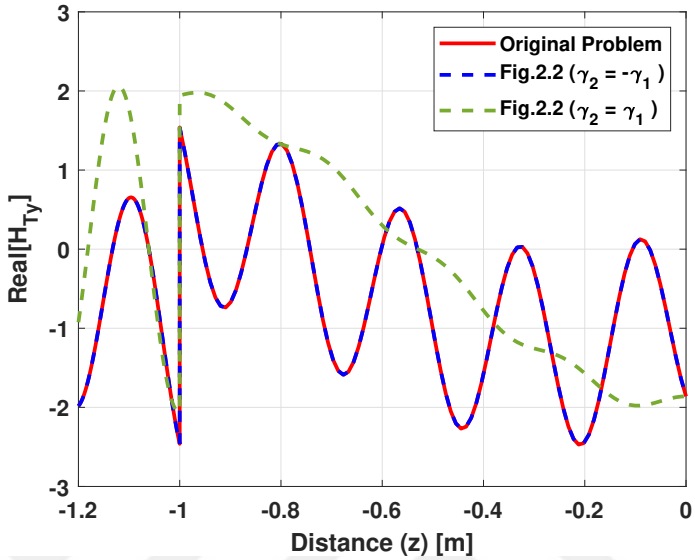

Figure 2.13: Real component of total H_y in Fig. 2.1 and Fig. 2.2 for a chiral-PEC interface problem.

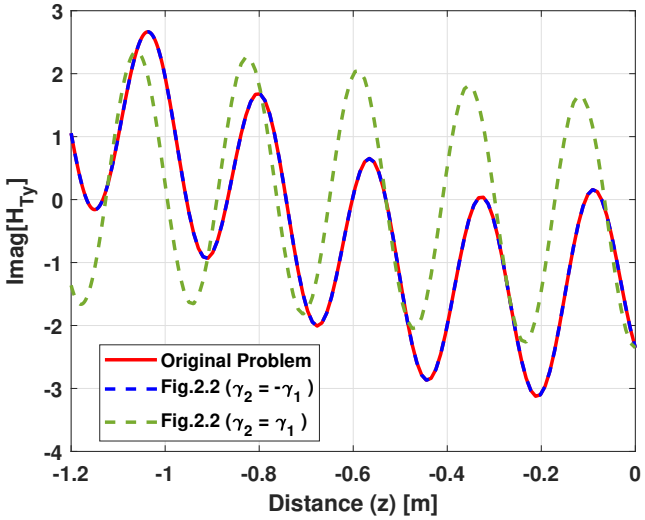

Figure 2.14: Imaginary component of total H_y in Fig. 2.1 and Fig. 2.2 for a chiral-PEC interface problem.

One can show that if $\gamma_2 = \pm\gamma_1 = 0$, then the chiral material behaves as a regular dielectric material and it is well known that the image of a dielectric body is itself.

2.2 Example-2

2.2.1 The Original Problem

In this section, a grounded chiral slab of finite thickness t is considered. The chiral slab is characterized by $(\epsilon_1, \mu_1, \gamma_1)$. The ambient medium is assumed to be a dielectric with material parameters (ϵ, μ). A current sheet carrying a surface current $\mathbf{J}_1$ is placed in the dielectric at a distance d away from a PEC plane. This original problem is shown in Fig. 2.3.

The surface current $\mathbf{J}_1$ is given by;

$$\mathbf{J}_1 = -2J_0\hat{x} \tag{2.33}$$

The incident field produced by this surface current $\mathbf{J}_1$ in the region $z < -d$ can be written as;

$$\mathbf{E}^{i-}(\mathbf{J}_1) = \hat{x}\eta J_0 e^{jk(z+d)} \tag{2.34}$$

$$\mathbf{H}^{i-}(\mathbf{J}_1) = -\hat{y}J_0 e^{jk(z+d)} \tag{2.35}$$

where the superscripts $i-$ represents that the field is traveling in $-z$ direction.

The incident field produced by the surface current $\mathbf{J}_1$ for region $z > -d$ are as follows;

$$\mathbf{E}^{i+}(\mathbf{J}_1) = \hat{x}\eta J_0 e^{-jk(z+d)} \tag{2.36}$$

$$\mathbf{H}^{i+}(\mathbf{J}_1) = \hat{y}J_0 e^{-jk(z+d)} \tag{2.37}$$

$$\eta = \sqrt{\frac{\mu}{\epsilon}} \quad , \quad k = w\sqrt{\mu\epsilon}\,. \tag{2.38}$$

Where k and η are the wavenumber and impedance of the dielectric, and the superscript $i+$ represents the incident field is traveling in the $+z$ direction in the dielectric. In the region $z < -t$, there may be a reflected field traveling in $-z$ direction given by;

$$\mathbf{E}^r(\mathbf{J}_1) = \eta J_0\Big\{\hat{x}b_1 + \hat{y}b_2\Big\}e^{jkz} \tag{2.39}$$

$$\mathbf{H}^r(\mathbf{J}_1) = J_0\Big\{ -\hat{y}b_1 + \hat{x}b_2\Big\}e^{jkz} \tag{2.40}$$

Where b_1 and b_2 are unknown constants. In the chiral medium ($-t < z < 0$), there will be a $+z$ traveling transmitted wave ($\mathbf{E}^t, \mathbf{H}^t$) and a $-z$ traveling reflected wave ($\mathbf{E}^r_{PEC}, \mathbf{H}^r_{PEC}$) given by

$$\mathbf{E}^t(\mathbf{J}_1) = \eta_{c_1} J_0\Big\{b_3(\hat{x} - j\hat{y})e^{-jh_1 z} + b_4(\hat{x} + j\hat{y})e^{-jh_2 z}\Big\} \tag{2.41}$$

$$\mathbf{H}^t(\mathbf{J}_1) = J_0\Big\{b_3(\hat{y} + j\hat{x})e^{-jh_1 z} + b_4(\hat{y} - j\hat{x})e^{-jh_2 z}\Big\} \tag{2.42}$$

$$\mathbf{E}^r_{PEC}(\mathbf{J}_1) = \eta_{c_1} J_0\Big\{b_5(\hat{x} + j\hat{y})e^{jh_1 z} + b_6(\hat{x} - j\hat{y})e^{jh_2 z}\Big\} \tag{2.43}$$

$$\mathbf{H}^r_{PEC}(\mathbf{J}_1) = J_0\Big\{b_5(-\hat{y} + j\hat{x})e^{jh_1 z} + b_6(-\hat{y} - j\hat{x})e^{jh_2 z}\Big\}. \tag{2.44}$$

Where $b_3 - b_6$ are also unknown constants to be found. To find these constant ($b_1 - b_6$) the following boundary conditions are used.

1. $\mathbf{E}^r_{PEC} + \mathbf{E}^t = 0$ at $z = 0$,
2. $\mathbf{E}^{i+} + \mathbf{E}^r = \mathbf{E}^t + \mathbf{E}^r_{PEC}$ at $z = -t$,
3. $\mathbf{H}^{i+} + \mathbf{H}^r = \mathbf{H}^t + \mathbf{H}^r_{PEC}$ at $z = -t$.

Then the unknown coefficients can be found as follows.

$$\begin{bmatrix} b_1 \\ b_2 \\ b_3 \\ b_4 \\ b_5 \\ b_6 \end{bmatrix} = Q^{-1} \begin{bmatrix} \eta e^{-jk(d-t)} \\ 0 \\ 0 \\ e^{-jk(d-t)} \\ 0 \\ 0 \end{bmatrix} \tag{2.45}$$

Where the matrix Q is given by Eqn. (2.46).

$$\mathbf{Q} = \begin{bmatrix} -\eta e^{-jkt} & 0 & \eta_{c_1} e^{jh_1 t} & \eta_{c_1} e^{jh_2 t} & \eta_{c_1} e^{-jh_1 t} & \eta_{c_1} e^{-jh_2 t} \\ 0 & -\eta e^{-jkt} & -j\eta_{c_1} e^{jh_1 t} & j\eta_{c_1} e^{jh_2 t} & j\eta_{c_1} e^{-jh_1 t} & -j\eta_{c_1} e^{-jh_2 t} \\ 0 & -e^{-jkt} & j e^{jh_1 t} & -j e^{jh_2 t} & j e^{-jh_1 t} & -j e^{-jh_2 t} \\ e^{-jkt} & 0 & e^{jh_1 t} & e^{jh_2 t} & -e^{-jh_1 t} & -e^{-jh_2 t} \\ 0 & 0 & 1 & 1 & 1 & 1 \\ 0 & 0 & -1 & 1 & 1 & -1 \end{bmatrix} \tag{2.46}$$

The coefficients $(b_1 - b_6)$ are as follows.

$$b_1 = \Big\{ e^{-jk(d-t)} - b_3 \big[e^{jh_1 t} + e^{-jh_2 t} \big] - b_4 \big[e^{jh_2 t} + e^{-jh_1 t} \big] \Big\} e^{jkt}$$

$$b_2 = \frac{j\eta_{c_1} e^{jkt}}{\eta} \Big\{ b_3 \big[e^{-jh_2 t} - e^{jh_1 t} \big] + b_4 \big[e^{jh_2 t} - e^{-jh_1 t} \big] \Big\}$$

$$b_3 = \frac{\eta e^{-jk(d-t)}}{e^{-jh_2 t}(\eta - \eta_{c_1}) + e^{jh_1 t}(\eta + \eta_{c_1})}$$

$$b_4 = \frac{\eta e^{-jk(d-t)}}{e^{-jh_1 t}(\eta - \eta_{c_1}) + e^{jh_2 t}(\eta + \eta_{c_1})}$$

$$b_5 = -b_4 \, , \quad b_6 = -b_3 \, .$$

2.2.2 The Equivalent Image Problem

In this problem, the ground plane is removed, and an image source $\mathbf{J}_2 = -\mathbf{J}_1$ is placed at $z = d$ and an image chiral slab with parameters $(\epsilon_1, \mu_1, \gamma_2)$ is placed between $z = 0$ and $z = t$ as shown in Fig. 2.4. Our purpose here is to show that when $\gamma_2 = -\gamma_1$, the total fields in the region $z < 0$ in Fig. 2.3 are identical to those in Fig. 2.4 in the same region.

There are four distinct regions in Fig. 2.4. The dielectric region $z < -t$ is named as d_1, while the dielectric region $z > t$ is denoted by d_2. Similarly, the chiral region $-t < z < 0$ is named as ch_1, while the chiral region $0 < z < t$ is denoted by ch_2.

The fields in Fig. 2.4 are produced by $\mathbf{J}_1$ and $\mathbf{J}_2$. Using the superposition principle, they can be computed separately. The fields produced by $\mathbf{J}_2$ are shown in the upper half of Fig. 2.4, and the fields produced by $\mathbf{J}_1$ are shown in the lower half of Fig. 2.4.

The incident field produced by $\mathbf{J}_2$ in region d_2 is given by.

$$\mathbf{E}^{ii}_{d_2}(\mathbf{J}_2) = -\hat{x}\eta J_0 e^{-jk(d-z)} \tag{2.47}$$

$$\mathbf{H}^{ii}_{d_2}(\mathbf{J}_2) = \hat{y} J_0 e^{-jk(d-z)} \tag{2.48}$$

The superscript ii represents the incident field, and the subscript d_2 is used to remind us that the field exists in region d_2. Part of this incident field is reflected at $z = t$ and can be written as follows.

$$\mathbf{E}^{ir}_{d_2}(\mathbf{J}_2) = \Big\{ -\hat{x}b_1^{'} + \hat{y}b_2^{'} \Big\} \eta J_0 e^{-jkz} \tag{2.49}$$

$$\mathbf{H}^{ir}_{d_2}(\mathbf{J}_2) = \Big\{ -\hat{y}b_1^{'} - \hat{x}b_2^{'} \Big\} J_0 e^{-jkz} \tag{2.50}$$

The other part is transmitted through the interface at $z = t$ and is given by;

$$\mathbf{E}^{it}_{ch_2}(\mathbf{J}_2) = \eta_{c_2} J_0 \Big\{ b_3^{'}(-\hat{x} - j\hat{y}) e^{jh_3 z} + b_4^{'}(-\hat{x} + j\hat{y}) e^{jh_4 z} \Big\} \tag{2.51}$$

$$\mathbf{H}^{it}_{ch_2}(\mathbf{J}_2) = J_0 \Big\{ b_3^{'}(\hat{y} - j\hat{x}) e^{jh_3 z} + b_4^{'}(\hat{y} + j\hat{x}) e^{jh_4 z} \Big\} \tag{2.52}$$

where $b_1^{'} - b_4^{'}$ are constants to be found. The superscripts ir and it represent the reflected and the transmitted fields at $z = t$ interface respectively.

There will also be reflected and transmitted fields at $z = 0$ interface (between two chiral media). These fields can be written as;

$$\mathbf{E}^{ir}_{ch_2}(\mathbf{J}_2) = \eta_{c_2} J_0 \Big\{ b_5^{'}(-\hat{x} + j\hat{y}) e^{-jh_3 z} + b_6^{'}(-\hat{x} - j\hat{y}) e^{-jh_4 z} \Big\} \tag{2.53}$$

$$\mathbf{H}^{ir}_{ch_2}(\mathbf{J}_2) = J_0\Big\{b^{'}_5(-\hat{y} - j\hat{x})e^{-jh_3z} + b^{'}_6(-\hat{y} + j\hat{x})e^{-jh_4z}\Big\} \tag{2.54}$$

$$\mathbf{E}^{it}_{ch_1}(\mathbf{J}_2) = \eta_{c_1}J_0\Big\{b^{'}_7(-\hat{x} - j\hat{y})e^{jh_1z} + b^{'}_8(-\hat{x} + j\hat{y})e^{jh_2z}\Big\} \tag{2.55}$$

$$\mathbf{H}^{it}_{ch_1}(\mathbf{J}_2) = J_0\Big\{b^{'}_7(\hat{y} - j\hat{x})e^{jh_1z} + b^{'}_8(\hat{y} + j\hat{x})e^{jh_2z}\Big\} \tag{2.56}$$

There will also be reflected and transmitted fields at $z = -t$ interface. These fields can be written as follows.

$$\mathbf{E}^{ir}_{ch_1}(\mathbf{J}_2) = \eta_{c_1}J_0\Big\{b^{'}_9(-\hat{x} + j\hat{y})e^{-jh_1z} + b^{'}_{10}(-\hat{x} - j\hat{y})e^{-jh_2z}\Big\} \tag{2.57}$$

$$\mathbf{H}^{ir}_{ch_1}(\mathbf{J}_2) = J_0\Big\{b^{'}_9(-\hat{y} - j\hat{x})e^{-jh_1z} + b^{'}_{10}(-\hat{y} + j\hat{x})e^{-jh_2z}\Big\} \tag{2.58}$$

$$\mathbf{E}^{it}_{d_1}(\mathbf{J}_2) = \eta J_0\Big\{ - \hat{x}b^{'}_{11} + \hat{y}b^{'}_{12}\Big\}e^{jkz} \tag{2.59}$$

$$\mathbf{H}^{it}_{d_1}(\mathbf{J}_2) = J_0\Big\{\hat{y}b^{'}_{11} + \hat{x}b^{'}_{12}\Big\}e^{jkz} \tag{2.60}$$

where $b^{'}_5 - b^{'}_{12}$ are also unknown constants. The above twelve unknown constants are determined by satisfying the boundary conditions at the interfaces at $z = -t, z = 0$, and $z = t$. The unknown coefficients are as follows.

$$b^{'}_1 = \frac{e^{jkt}}{(\eta + \eta_{c_2})}\Big\{(\eta_{c_2} - \eta)e^{-jk(d-t)} + 2\eta_{c_2}b^{'}_5e^{-jh_3t} + 2\eta_{c_2}b^{'}_6e^{-jh_4t}\Big\}$$

$$b^{'}_2 = \frac{e^{jkt}}{(\eta_{c_2} - \eta)}\Big\{2j\eta_{c_2}b^{'}_3e^{jh_3t} - 2j\eta_{c_2}b^{'}_4e^{jh_4t}\Big\}$$

$$b^{'}_3 = \frac{1}{(\eta_{c_1} + \eta_{c_2})}\Big\{b^{'}_6(\eta_{c_1} - \eta_{c_2}) + 2\eta_{c_1}b^{'}_7\Big\}$$

$$b^{'}_4 = \frac{1}{(\eta_{c_1} + \eta_{c_2})}\Big\{b^{'}_5(\eta_{c_1} - \eta_{c_2}) + 2\eta_{c_1}b^{'}_8\Big\}$$

$$b_5^{'} = \frac{1}{(\eta_{c_1} + \eta_{c_2})}\Big\{b_4^{'}(\eta_{c_1} - \eta_{c_2}) + 2\eta_{c_1} b_9^{'}\Big\}$$

$$b_6^{'} = \frac{1}{(\eta_{c_1} + \eta_{c_2})}\Big\{b_3^{'}(\eta_{c_1} - \eta_{c_2}) + 2\eta_{c_1} b_{10}^{'}\Big\}$$

$$b_7^{'} = \frac{-je^{jh_1 t}}{4\eta_{c_1}}\Big\{j(\eta_{c_1} + \eta)b_{11}^{'}e^{-jkt} + (\eta_{c_1} + \eta)b_{12}^{'}e^{-jkt}\Big\}$$

$$b_8^{'} = \frac{-je^{jh_2 t}}{4\eta_{c_1}}\Big\{j(\eta_{c_1} + \eta)b_{11}^{'}e^{-jkt} + (\eta_{c_1} + \eta)b_{12}^{'}e^{-jkt}\Big\}$$

$$b_9^{'} = \frac{-je^{-jh_1 t}}{4\eta_{c_1}}\Big\{j(\eta - \eta_{c_1})b_{11}^{'}e^{-jkt} + (\eta - \eta_{c_1})b_{12}^{'}e^{-jkt}\Big\}$$

$$b_{10}^{'} = \frac{-je^{-jh_2 t}}{4\eta_{c_1}}\Big\{j(\eta - \eta_{c_1})b_{11}^{'}e^{-jkt} + (\eta - \eta_{c_1})b_{12}^{'}e^{-jkt}\Big\}$$

$$b_{11}^{'} = \Big\{2\eta e^{2jkt}e^{-jkd}\big[\eta_{c_2}e^{jh_1 t}e^{jh_3 t} + \eta_{c_2}e^{jh_2 t}e^{jh_4 t}\big]\Big\} \times \Big\{2\eta\eta_{c_1} - \eta^2 - \eta_{c_2}^2 + \eta^2 S + \eta_{c_1}^2 S + 2\eta\eta_{c_2} S\Big\}^{-1}$$

$$b_{12}^{'} = \Big\{2j\eta e^{2jkt}e^{-jkd}\big[j\eta_{c_2}e^{jh_1 t}e^{jh_3 t} - j\eta_{c_2}e^{jh_2 t}e^{jh_4 t}\big]\Big\} \times \Big\{2j\eta\eta_{c_1} - j\eta^2 - j\eta_{c_2}^2 + j\eta^2 S + j\eta_{c_1}^2 S + 2j\eta\eta_{c_2} S\Big\}^{-1}$$

where $S = e^{jh_1 t}e^{jh_2 t}e^{jh_3 t}e^{jh_4 t}$.

Similarly, the fields due to surface current $\mathbf{J}_1$ can be written in the four regions. In region d_1, the following fields exist.

$$\mathbf{E}_{d_1}^{i+}(\mathbf{J}_1) = \hat{x}\eta J_0 e^{-jk(z+d)} \tag{2.61}$$

$$\mathbf{H}_{d_1}^{i+}(\mathbf{J}_1) = \hat{y} J_0 e^{-jk(z+d)} \tag{2.62}$$

$$\mathbf{E}^{r}_{d_1}(\mathbf{J}_1) = \Big\{\hat{x}b^{''}_1 + \hat{y}b^{''}_2\Big\}\eta J_0 e^{jkz} \tag{2.63}$$

$$\mathbf{H}^{r}_{d_1}(\mathbf{J}_1) = \Big\{ -\hat{y}b^{''}_1 + \hat{x}b^{''}_2\Big\}J_0 e^{jkz} \tag{2.64}$$

In region ch_1, the fields due to $\mathbf{J}_1$ are written as follows.

$$\mathbf{E}^{t}_{ch_1}(\mathbf{J}_1) = \eta_{c_1} J_0\Big\{b^{''}_3(\hat{x} - j\hat{y})e^{-jh_1 z} + b^{''}_4(\hat{x} + j\hat{y})e^{-jh_2 z}\Big\} \tag{2.65}$$

$$\mathbf{H}^{t}_{ch_1}(\mathbf{J}_1) = J_0\Big\{b^{''}_3(\hat{y} + j\hat{x})e^{-jh_1 z} + b^{''}_4(\hat{y} - j\hat{x})e^{-jh_2 z}\Big\} \tag{2.66}$$

$$\mathbf{E}^{r}_{ch_1}(\mathbf{J}_1) = \eta_{c_1} J_0\Big\{b^{''}_5(\hat{x} + j\hat{y})e^{jh_1 z} + b^{''}_6(\hat{x} - j\hat{y})e^{jh_2 z}\Big\} \tag{2.67}$$

$$\mathbf{H}^{r}_{ch_1}(\mathbf{J}_1) = J_0\Big\{b^{''}_5(-\hat{y} + j\hat{x})e^{jh_1 z} + b^{''}_6(-\hat{y} - j\hat{x})e^{jh_2 z}\Big\} \tag{2.68}$$

Similarly, the fields in region ch_2 are as follows.

$$\mathbf{E}^{t}_{ch_2}(\mathbf{J}_1) = \eta_{c_2} J_0\Big\{b^{''}_7(\hat{x} - j\hat{y})e^{-jh_3 z} + b^{''}_8(\hat{x} + j\hat{y})e^{-jh_4 z}\Big\} \tag{2.69}$$

$$\mathbf{H}^{t}_{ch_2}(\mathbf{J}_1) = J_0\Big\{b^{''}_7(\hat{y} + j\hat{x})e^{-jh_3 z} + b^{''}_8(\hat{y} - j\hat{x})e^{-jh_4 z}\Big\} \tag{2.70}$$

$$\mathbf{E}^{r}_{ch_2}(\mathbf{J}_1) = \eta_{c_2} J_0\Big\{b^{''}_9(\hat{x} + j\hat{y})e^{jh_3 z} + b^{''}_{10}(\hat{x} - j\hat{y})e^{jh_4 z}\Big\} \tag{2.71}$$

$$\mathbf{H}^{r}_{ch_2}(\mathbf{J}_1) = J_0\Big\{b^{''}_9(-\hat{y} + j\hat{x})e^{jh_3 z} + b^{''}_{10}(-\hat{y} - j\hat{x})e^{jh_4 z}\Big\} \tag{2.72}$$

Finally, the field in region d_2 due to $\mathbf{J}_1$ can be written as follows.

$$\mathbf{E}^{t}_{d_2}(\mathbf{J}_1) = \eta J_0\Big\{\hat{x}b^{''}_{11} + \hat{y}b^{''}_{12}\Big\}e^{-jkz} \tag{2.73}$$

$$\mathbf{H}^{t}_{d_2}(\mathbf{J}_1) = J_0\Big\{\hat{y}b^{''}_{11} - \hat{x}b^{''}_{12}\Big\}e^{-jkz} \tag{2.74}$$

The twelve unknown constants $b^{''}_1 - b^{''}_{12}$ are computed by satisfying the boundary conditions at the three interfaces ($z = -t, z = 0, z = t$). The unknown coefficients are as follows.

$$b_1^{''} = \frac{e^{jkt}}{(\eta + \eta_{c_1})}\Big\{(\eta - \eta_{c_1})e^{-jk(d-t)} - 2\eta_{c_1}b_5^{''}e^{-jh_1t} - 2\eta_{c_1}b_6^{''}e^{-jh_2t}\Big\}$$

$$b_2^{''} = \frac{e^{jkt}}{(\eta_{c_1} - \eta)}\Big\{2j\eta_{c_1}b_4^{''}e^{jh_2t} - 2j\eta_{c_1}b_3^{''}e^{jh_1t}\Big\}$$

$$b_3^{''} = \frac{1}{2\eta_{c_1}}\Big\{b_{10}^{''}(\eta_{c_2} - \eta_{c_1}) + 2(\eta_{c_1} + \eta_{c_2})b_7^{''}\Big\}$$

$$b_4^{''} = \frac{1}{2\eta_{c_1}}\Big\{b_9^{''}(\eta_{c_2} - \eta_{c_1}) + 2(\eta_{c_1} + \eta_{c_2})b_8^{''}\Big\}$$

$$b_5^{''} = \frac{1}{2\eta_{c_1}}\Big\{b_8^{''}(\eta_{c_2} - \eta_{c_1}) + 2(\eta_{c_1} + \eta_{c_2})b_9^{''}\Big\}$$

$$b_6^{''} = \frac{1}{2\eta_{c_1}}\Big\{b_7^{''}(\eta_{c_2} - \eta_{c_1}) + 2(\eta_{c_1} + \eta_{c_2})b_{10}^{''}\Big\}$$

$$b_7^{''} = \frac{-je^{jh_3t}}{4\eta_{c_2}}\Big\{j(\eta_{c_2} + \eta)b_{11}^{''}e^{-jkt} + (\eta_{c_2} - \eta)b_{12}^{''}e^{-jkt}\Big\}$$

$$b_8^{''} = \frac{-je^{jh_4t}}{4\eta_{c_2}}\Big\{j(\eta_{c_2} + \eta)b_{11}^{''}e^{-jkt} + (\eta_{c_2} + \eta)b_{12}^{''}e^{-jkt}\Big\}$$

$$b_9^{''} = \frac{-je^{-jh_3t}}{4\eta_{c_2}}\Big\{j(\eta - \eta_{c_2})b_{11}^{''}e^{-jkt} + (\eta - \eta_{c_2})b_{12}^{''}e^{-jkt}\Big\}$$

$$b_{10}^{''} = \frac{-je^{-jh_4t}}{4\eta_{c_2}}\Big\{j(\eta - \eta_{c_2})b_{11}^{''}e^{-jkt} + (\eta - \eta_{c_2})b_{12}^{''}e^{-jkt}\Big\}$$

$$b_{11}^{''} = \Big\{2\eta e^{2jkt}e^{-jkd}\big[\eta_{c_1}e^{jh_1t}e^{jh_3t} + \eta_{c_1}e^{jh_2t}e^{jh_4t}\big]\Big\} \times \Big\{2\eta\eta_{c_2} - \eta^2 - \eta_{c_1}^2 + \eta^2 S + \eta_{c_2}^2 S + 2\eta\eta_{c_1}S\Big\}^{-1}$$

$$b_{12}'' = \left\{ 2j\eta e^{2jkt} e^{-jkd} \left[j\eta_{c_1} e^{jh_1 t} e^{jh_3 t} - j\eta_{c_1} e^{jh_2 t} e^{jh_4 t} \right] \right\} \times \left\{ 2j\eta\eta_{c_2} - j\eta^2 - j\eta_{c_1}^2 + j\eta^2 S + j\eta_{c_2}^2 S + 2j\eta\eta_{c_1} S \right\}^{-1}$$

where $S = e^{jh_1 t} e^{jh_2 t} e^{jh_3 t} e^{jh_4 t}$.

2.2.3 Fields Computation

To demonstrate the behavior of the electric and magnetic fields in various parts of the problems, we have computed the fields for a special case of $J_0 = 1$ (A/m), $\epsilon_r = 2$, $\mu_r = 1$, $\gamma_1 = 0.005$, $d = 1$ m, $t = 0.1$ m and $f = 300$ MHz. The computed results are shown in Figs. 2.15 - 2.22. Figure 2.15 shows the real part of x-component of the total electric field. There are three curves in this figure. It is seen that when $\gamma_2 = -\gamma_1$, the fields of the image problem are the same as the fields in the original problem. Where as, these two fields are not the same when $\gamma_2 = \gamma_1$ at $z = 0$ and $z = -t$ interfaces. Note that total E_y is not zero at $z = 0$ interface, when $\gamma_2 \neq -\gamma_1$. This is clear from Figs. 2.17 and 2.18. The other six figures (2.15, 2.16, 2.19 - 2.22) also support the conclusion that the image chiral material must have $\gamma_2 = -\gamma_1$.

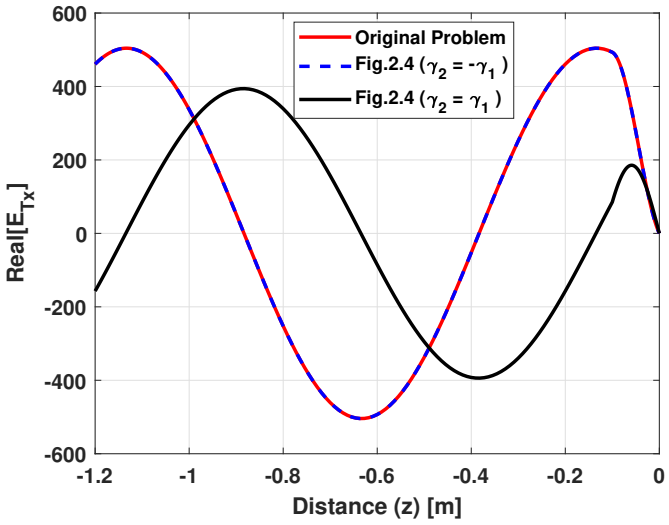

Figure 2.15: Real component of total E_x in Fig. 2.3 and Fig. 2.4 for a grounded chiral slab problem.

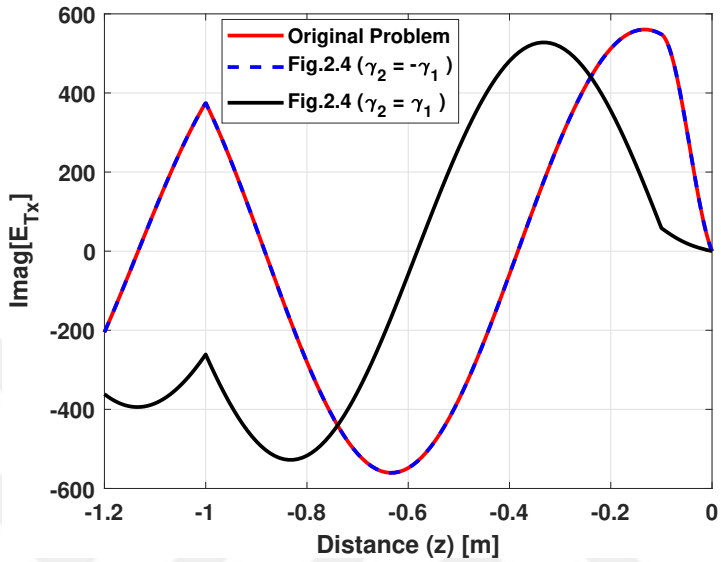

Figure 2.16: Imaginary component of total E_x in Fig. 2.3 and Fig. 2.4 for a grounded chiral slab problem.

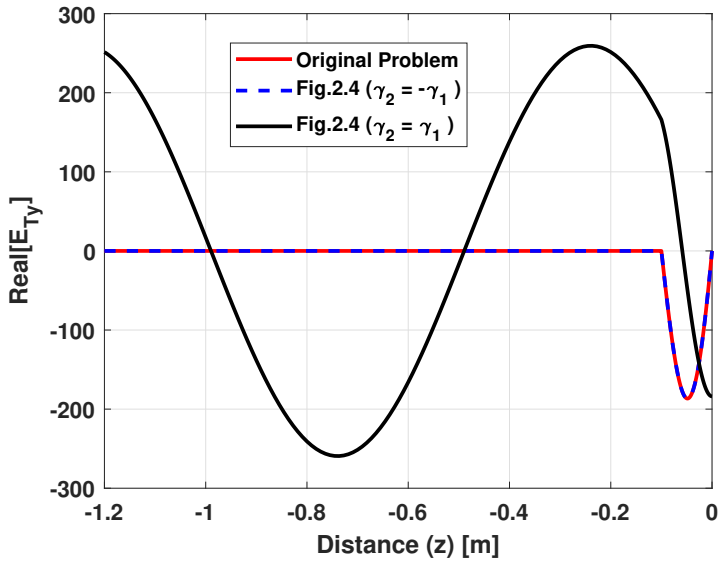

Figure 2.17: Real component of total E_y in Fig. 2.3 and Fig. 2.4 for a grounded chiral slab problem.

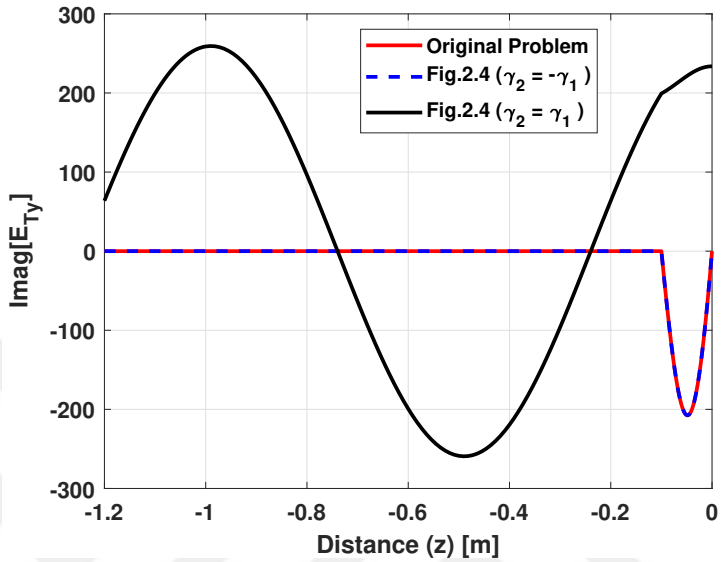

Figure 2.18: Imaginary component of total E_y in Fig. 2.3 and Fig. 2.4 for a grounded chiral slab problem.

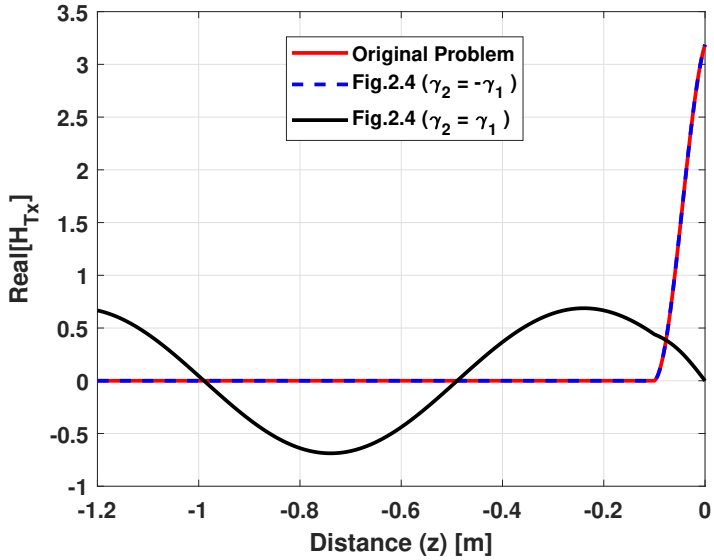

Figure 2.19: Real component of total H_x in Fig. 2.3 and Fig. 2.4 for a grounded chiral slab problem.

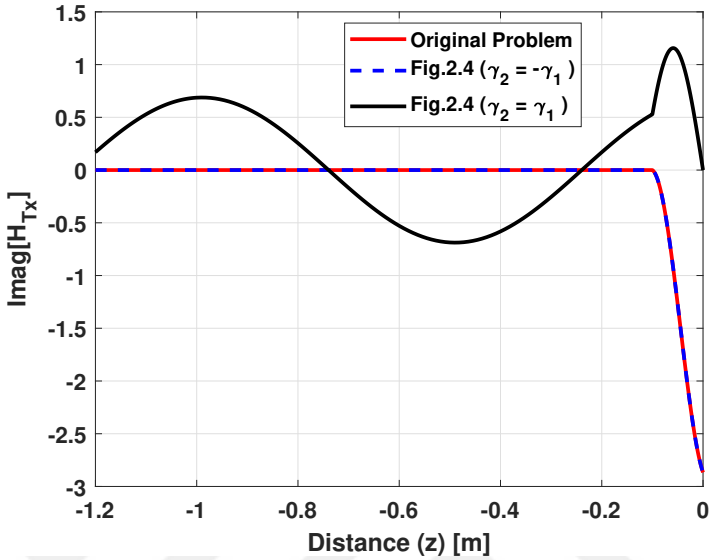

Figure 2.20: Imaginary component of total H_x in Fig. 2.3 and Fig. 2.4 for a grounded chiral slab problem.

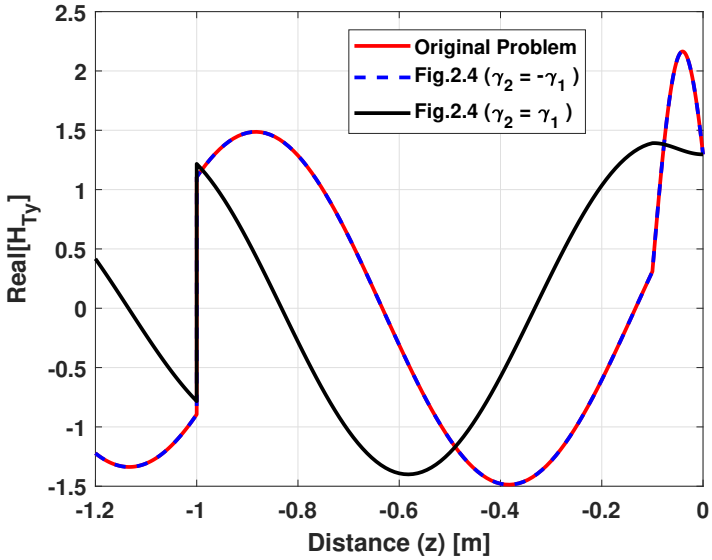

Figure 2.21: Real component of total H_y in Fig. 2.3 and Fig. 2.4 for a grounded chiral slab problem.

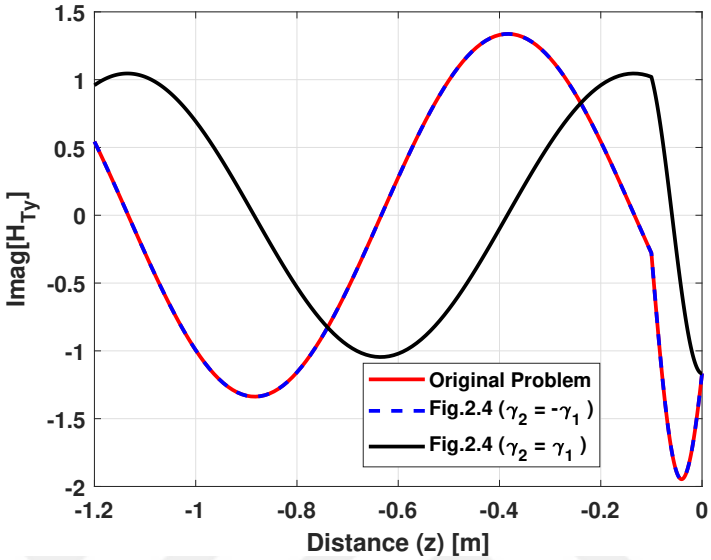

Figure 2.22: Imaginary component of total H_y in Fig. 2.3 and Fig. 2.4 for a grounded chiral slab problem.

2.3 Example-3

2.3.1 The Original Problem

In this section, a chiral slab of finite thickness t, confined between two dielectric mediums, is considered. For simplicity, the ambient mediums have the same material parameters (ϵ, μ). The chiral slab is characterized by $(\epsilon_1, \mu_1, \gamma_1)$, and occupies the region $-z_2 < z < -z_1$, away from the PEC plane. A current sheet carrying a surface current $\mathbf{J}_1$ is placed in the dielectric at a distance d away from the PEC interface. This original problem is shown in Fig. 2.5. Among the three canonical problems considered here, this problem is approximately more representative of the problem considered in Chapter 3.

The surface current $\mathbf{J}_1$ is defined as;

$$\mathbf{J}_1 = -2J_0\hat{x} \tag{2.75}$$

The incident field produced by this surface current $\mathbf{J}_1$ in the region $z < -d$ can be written as;

$$\mathbf{E}^{i-}(\mathbf{J}_1) = \hat{x}\eta J_0 e^{jk(z+d)} \tag{2.76}$$

$$\mathbf{H}^{i-}(\mathbf{J}_1) = -\hat{y} J_0 e^{jk(z+d)} \tag{2.77}$$

where the superscripts $i-$ represents that the field traveling in $-z$ direction.

The incident field produced by this surface current for region $z > -d$ are as follows;

$$\mathbf{E}^{i+}(\mathbf{J}_1) = \hat{x}\eta J_0 e^{-jk(z+d)} \tag{2.78}$$

$$\mathbf{H}^{i+}(\mathbf{J}_1) = \hat{y} J_0 e^{-jk(z+d)} \tag{2.79}$$

The superscript $i+$ represents the incident field is traveling in the $+z$ direction in the dielectric. In the region $z < -z_2$, there may be a reflected field traveling in $-z$ direction given by

$$\mathbf{E}^{r}(\mathbf{J}_1) = \eta J_0 \Big\{ \hat{x} f_1 + \hat{y} f_2 \Big\} e^{jkz} \tag{2.80}$$

$$\mathbf{H}^{r}(\mathbf{J}_1) = J_0 \Big\{ -\hat{y} f_1 + \hat{x} f_2 \Big\} e^{jkz} \tag{2.81}$$

Where $f_1 - f_2$ are unknown constants. In the chiral medium ($-z_2 < z < -z_1$), there will be a $+z$ travelling transmitted wave ($\mathbf{E}^{1t}, \mathbf{H}^{1t}$) and a $-z$ traveling reflected wave ($\mathbf{E}^{1r}, \mathbf{H}^{1r}$) given by

$$\mathbf{E}^{1t}(\mathbf{J}_1) = \eta_{c_1} J_0 \Big\{ f_3(\hat{x} - j\hat{y}) e^{-jh_1 z} + f_4(\hat{x} + j\hat{y}) e^{-jh_2 z} \Big\} \tag{2.82}$$

$$\mathbf{H}^{1t}(\mathbf{J}_1) = J_0 \Big\{ f_3(\hat{y} + j\hat{x}) e^{-jh_1 z} + f_4(\hat{y} - j\hat{x}) e^{-jh_2 z} \Big\} \tag{2.83}$$

$$\mathbf{E}^{1r}(\mathbf{J}_1) = \eta_{c_1} J_0 \Big\{ f_5(\hat{x} + j\hat{y}) e^{jh_1 z} + f_6(\hat{x} - j\hat{y}) e^{jh_2 z} \Big\} \tag{2.84}$$

$$\mathbf{H}^{1r}(\mathbf{J}_1) = J_0 \Big\{ f_5(-\hat{y} + j\hat{x}) e^{jh_1 z} + f_6(-\hat{y} - j\hat{x}) e^{jh_2 z} \Big\} \tag{2.85}$$

Where $f_3 - f_6$ are unknown constants. In the dielectric medium ($-z_1 < z < 0$), there will be a $+z$ travelling transmitted wave ($\mathbf{E}^{t}, \mathbf{H}^{t}$) and a $-z$ traveling reflected wave ($\mathbf{E}^{r}_{PEC}, \mathbf{H}^{r}_{PEC}$) given by

$$\mathbf{E}^t(\mathbf{J}_1) = \eta J_0 \Big\{ \hat{x} f_7 + \hat{y} f_8 \Big\} e^{-jkz} \tag{2.86}$$

$$\mathbf{H}^t(\mathbf{J}_1) = J_0 \Big\{ \hat{y} f_7 - \hat{x} f_8 \Big\} e^{-jkz} \tag{2.87}$$

$$\mathbf{E}^r_{PEC}(\mathbf{J}_1) = \eta J_0 \Big\{ \hat{x} f_9 + \hat{y} f_{10} \Big\} e^{jkz} \tag{2.88}$$

$$\mathbf{H}^r_{PEC}(\mathbf{J}_1) = J_0 \Big\{ -\hat{y} f_9 + \hat{x} f_{10} \Big\} e^{jkz} \tag{2.89}$$

Where $f_7 - f_{10}$ are also unknown constants to be found. To find these ten unknown constants ($f_1 - f_{10}$), appropriate boundary conditions are satisfied at the $z = -z_2, z = -z_1$, and $z = 0$ interfaces. The unknown coefficients are as follows.

$$f_1 = \frac{e^{jkz_2}}{(\eta + \eta_{c_1})} \Big\{ (\eta_{c_1} - \eta) e^{-jk(d - z_2)} + 2\eta_{c_1} f_5 e^{-jh_1 z_2} + 2\eta_{c_1} f_6 e^{-jh_2 z_2} \Big\}$$

$$f_2 = \frac{e^{jkz_2}}{(\eta_{c_1} + \eta)} \Big\{ 2j\eta_{c_1} f_5 e^{-jh_1 z_2} - 2j\eta_{c_1} f_6 e^{-jh_2 z_2} \Big\}$$

$$f_3 = \frac{-je^{-jh_1 z_1}}{4\eta_{c_1}} \Big\{ j(\eta_{c_1} + \eta) f_7 e^{jkz_1} - j(\eta - \eta_{c_1}) f_7 e^{-jkz_1} - (\eta_{c_1} + \eta) f_8 e^{jkz_1} + (\eta - \eta_{c_1}) f_8 e^{-jkz_1} \Big\}$$

$$f_4 = \frac{-je^{-jh_2 z_1}}{4\eta_{c_1}} \Big\{ j(\eta_{c_1} + \eta) f_7 e^{jkz_1} - j(\eta - \eta_{c_1}) f_7 e^{-jkz_1} + (\eta_{c_1} + \eta) f_8 e^{jkz_1} - (\eta - \eta_{c_1}) f_8 e^{-jkz_1} \Big\}$$

$$f_5 = \frac{-je^{jh_1 z_1}}{4\eta_{c_1}} \Big\{ j(\eta - \eta_{c_1}) f_7 e^{jkz_1} - j(\eta + \eta_{c_1}) f_7 e^{-jkz_1} + (\eta - \eta_{c_1}) f_8 e^{jkz_1} - (\eta + \eta_{c_1}) f_8 e^{-jkz_1} \Big\}$$

$$f_6 = \frac{-je^{jh_2 z_1}}{4\eta_{c_1}} \Big\{ j(\eta - \eta_{c_1}) f_7 e^{jkz_1} - j(\eta + \eta_{c_1}) f_7 e^{-jkz_1} + (\eta_{c_1} - \eta) f_8 e^{jkz_1} + (\eta + \eta_{c_1}) f_8 e^{-jkz_1} \Big\}$$

$$f_7 = \Big\{2\eta e^{jkz_1}e^{-jk(d-z_2)}\big[\eta_{c_1}e^{jh_1z_2}e^{jh_2z_1} + \eta_{c_1}e^{jh_2z_2}e^{jh_1z_1}\big]\Big\}$$
$$\times\Big\{(\eta_{c_1}^2-\eta^2)e^{jh_1z_2}e^{jh_2z_2} + (\eta^2-\eta_{c_1}^2)e^{jh_1z_1}e^{jh_2z_1}$$
$$-(\eta_{c_1}^2+\eta^2)e^{jh_1z_1}e^{jh_2z_1}e^{2jkz_1} + (\eta_{c_1}^2+\eta^2)e^{jh_1z_2}e^{jh_2z_2}e^{2jkz_1}$$
$$+2\eta\eta_{c_1}\big[e^{jh_1z_1}e^{jh_2z_1}e^{2jkz_1} + e^{jh_1z_2}e^{jh_2z_2}e^{2jkz_1}\big]\Big\}^{-1}$$

$$f_8 = \Big\{2j\eta e^{jkz_1}e^{-jk(d-z_2)}\big[j\eta_{c_1}e^{jh_1z_2}e^{jh_2z_1} - j\eta_{c_1}e^{jh_2z_2}e^{jh_1z_1}\big]\Big\}$$
$$\times\Big\{j(\eta_{c_1}^2-\eta^2)e^{jh_1z_2}e^{jh_2z_2} + j(\eta^2-\eta_{c_1}^2)e^{jh_1z_1}e^{jh_2z_1}$$
$$-j(\eta_{c_1}^2+\eta^2)e^{jh_1z_1}e^{jh_2z_1}e^{2jkz_1} + j(\eta_{c_1}^2+\eta^2)e^{jh_1z_2}e^{jh_2z_2}e^{2jkz_1}$$
$$+2j\eta\eta_{c_1}\big[e^{jh_1z_1}e^{jh_2z_1}e^{2jkz_1} + e^{jh_1z_2}e^{jh_2z_2}e^{2jkz_1}\big]\Big\}^{-1}$$

$$f_9 = -f_7\,, \quad f_{10} = -f_8\,.$$

2.3.2 The Equivalent Image Problem

In this problem, the ground plane is removed, and an image source $\mathbf{J}_2 = -\mathbf{J}_1$ is placed at $z = d$ and an image chiral slab with parameters $(\epsilon_1, \mu_1, \gamma_2)$ is placed between $z = z_1$ and $z = z_2$ as shown in Fig. 2.6. Our purpose here is to show that when $\gamma_2 = -\gamma_1$, the total fields in the region $z < 0$ in Fig. 2.5 are identical to those in Fig. 2.6 in the same region.

There are six distinct regions in Fig. 2.6. The dielectric regions ($-d < z < -z_2$ and $-z_1 < z < 0$) (right to the $z = 0$ interface) are named as d_1 and d_2 respectively, while the dielectric regions ($0 < z < z_1$ and $z_2 < z < d$) (left to the $z = 0$ interface) are denoted by d_3 and d_4 respectively. Similarly, the chiral region $-z_2 < z < -z_1$ is named as ch_1, while the chiral region $z_1 < z < z_2$ is denoted by ch_2.

The fields in Fig. 2.6 are produced by $\mathbf{J}_1$ and $\mathbf{J}_2$. Using the superposition principle, they can be computed separately. The fields produced by $\mathbf{J}_2$ are shown

in the upper half of Fig. 2.6, and the fields produced by $\mathbf{J}_1$ are shown in the lower half of Fig. 2.6.

The incident field produced by $\mathbf{J}_2$ in region d_4 is given by

$$\mathbf{E}^{ii}_{d_4}(\mathbf{J}_2) = -\hat{x}\eta J_0 e^{jk(z-d)} \tag{2.90}$$

$$\mathbf{H}^{ii}_{d_4}(\mathbf{J}_2) = \hat{y} J_0 e^{jk(z-d)} \tag{2.91}$$

The superscript ii represents the incident field, and the subscript d_4 is used to remind us that the field exists in region d_4. Part of this incident field is reflected at $z = z_2$ and can be written as follows.

$$\mathbf{E}^{ir}_{d_4}(\mathbf{J}_2) = \eta J_0 \Big\{ -\hat{x} f_1^{'} + \hat{y} f_2^{'} \Big\} e^{-jkz} \tag{2.92}$$

$$\mathbf{H}^{ir}_{d_4}(\mathbf{J}_2) = J_0 \Big\{ -\hat{y} f_1^{'} - \hat{x} f_2^{'} \Big\} e^{-jkz} \tag{2.93}$$

The other part is transmitted through the interface at $z = z_2$ and is given by;

$$\mathbf{E}^{it}_{ch_2}(\mathbf{J}_2) = \eta_{c_2} J_0 \Big\{ f_3^{'}(-\hat{x} - j\hat{y}) e^{jh_3 z} + f_4^{'}(-\hat{x} + j\hat{y}) e^{jh_4 z} \Big\} \tag{2.94}$$

$$\mathbf{H}^{it}_{ch_2}(\mathbf{J}_2) = J_0 \Big\{ f_3^{'}(\hat{y} - j\hat{x}) e^{jh_3 z} + f_4^{'}(\hat{y} + j\hat{x}) e^{jh_4 z} \Big\} \tag{2.95}$$

where $f_1^{'} - f_4^{'}$ are constants to be found. There will also be reflected and transmitted fields at $z = z_1$ interface. These fields can be written as

$$\mathbf{E}^{ir}_{ch_2}(\mathbf{J}_2) = \eta_{c_2} J_0 \Big\{ f_5^{'}(-\hat{x} + j\hat{y}) e^{-jh_3 z} + f_6^{'}(-\hat{x} - j\hat{y}) e^{-jh_4 z} \Big\} \tag{2.96}$$

$$\mathbf{H}^{ir}_{ch_2}(\mathbf{J}_2) = J_0 \Big\{ f_5^{'}(-\hat{y} - j\hat{x}) e^{-jh_3 z} + f_6^{'}(-\hat{y} + j\hat{x}) e^{-jh_4 z} \Big\} \tag{2.97}$$

$$\mathbf{E}^{it}_{d_3}(\mathbf{J}_2) = \eta J_0 \Big\{ -\hat{x} f_7^{'} + \hat{y} f_8^{'} \Big\} e^{jkz} \tag{2.98}$$

$$\mathbf{H}^{it}_{d_3}(\mathbf{J}_2) = J_0 \Big\{ \hat{y} f_7^{'} + \hat{x} f_8^{'} \Big\} e^{jkz} \tag{2.99}$$

There will also be reflected and transmitted fields at $z = 0$ interface. These fields can be written as follows.

$$\mathbf{E}^{ir}_{d_3}(\mathbf{J}_2) = \eta J_0 \Big\{ -\hat{x} f_9^{'} + \hat{y} f_{10}^{'} \Big\} e^{-jkz} \tag{2.100}$$

$$\mathbf{H}^{ir}_{d_3}(\mathbf{J}_2) = J_0\Big\{ -\hat{y}f^{'}_{9} - \hat{x}f^{'}_{10}\Big\}e^{-jkz} \tag{2.101}$$

$$\mathbf{E}^{it}_{d_2}(\mathbf{J}_2) = \eta J_0\Big\{ -\hat{x}f^{'}_{11} + \hat{y}f^{'}_{12}\Big\}e^{jkz} \tag{2.102}$$

$$\mathbf{H}^{it}_{d_2}(\mathbf{J}_2) = J_0\Big\{\hat{y}f^{'}_{11} + \hat{x}f^{'}_{12}\Big\}e^{jkz} \tag{2.103}$$

There will also be reflected and transmitted fields at $z = -z_1$ interface. These fields can be written as

$$\mathbf{E}^{ir}_{d_2}(\mathbf{J}_2) = \eta J_0\Big\{ -\hat{x}f^{'}_{13} + \hat{y}f^{'}_{14}\Big\}e^{-jkz} \tag{2.104}$$

$$\mathbf{H}^{ir}_{d_2}(\mathbf{J}_2) = J_0\Big\{ -\hat{y}f^{'}_{13} - \hat{x}f^{'}_{14}\Big\}e^{-jkz} \tag{2.105}$$

$$\mathbf{E}^{it}_{ch_1}(\mathbf{J}_2) = \eta_{c_1} J_0\Big\{ f^{'}_{15}(-\hat{x} - j\hat{y})e^{jh_1 z} + f^{'}_{16}(-\hat{x} + j\hat{y})e^{jh_2 z}\Big\} \tag{2.106}$$

$$\mathbf{H}^{it}_{ch_1}(\mathbf{J}_2) = J_0\Big\{ f^{'}_{15}(\hat{y} - j\hat{x})e^{jh_1 z} + f^{'}_{16}(\hat{y} + j\hat{x})e^{jh_2 z}\Big\} \tag{2.107}$$

The fields transmitted to and reflected by the interface $z = -z_2$ are given by

$$\mathbf{E}^{ir}_{ch_1}(\mathbf{J}_2) = \eta_{c_1} J_0\Big\{ f^{'}_{17}(-\hat{x} + j\hat{y})e^{-jh_1 z} + f^{'}_{18}(-\hat{x} - j\hat{y})e^{-jh_2 z}\Big\} \tag{2.108}$$

$$\mathbf{H}^{ir}_{ch_1}(\mathbf{J}_2) = J_0\Big\{ f^{'}_{17}(-\hat{y} - j\hat{x})e^{-jh_1 z} + f^{'}_{18}(-\hat{y} + j\hat{x})e^{-jh_2 z}\Big\} \tag{2.109}$$

$$\mathbf{E}^{it}_{d_1}(\mathbf{J}_2) = \eta J_0\Big\{ -\hat{x}f^{'}_{19} + \hat{y}f^{'}_{20}\Big\}e^{jkz} \tag{2.110}$$

$$\mathbf{H}^{it}_{d_1}(\mathbf{J}_2) = J_0\Big\{\hat{y}f^{'}_{19} + \hat{x}f^{'}_{20}\Big\}e^{jkz} \tag{2.111}$$

where $f^{'}_{5} - f^{'}_{20}$ are unknown constants. To find these twenty unknown constants $(f^{'}_{5} - f^{'}_{20})$, appropriate boundary conditions are satisfied at the five interfaces $(z = -z_2, z = -z_1, z = 0, z = z_1, z = z_2)$. Since there are many unknowns, the coefficients are computed numerically using MATLAB ® [84].

Similarly, the fields due to surface current $\mathbf{J}_1$ can be written in the six region. In region d_1, the following fields exist.

$$\mathbf{E}^{i+}_{d_1}(\mathbf{J}_1) = \hat{x}\eta J_0 e^{-jk(z+d)} \tag{2.112}$$

$$\mathbf{H}^{i+}_{d_1}(\mathbf{J}_1) = \hat{y} J_0 e^{-jk(z+d)} \tag{2.113}$$

$$\mathbf{E}^{r}_{d_1}(\mathbf{J}_1) = \eta J_0 \Big\{ \hat{x} f_1^{''} + \hat{y} f_2^{''} \Big\} e^{jkz} \tag{2.114}$$

$$\mathbf{H}^{r}_{d_1}(\mathbf{J}_1) = J_0 \Big\{ -\hat{y} f_1^{''} + \hat{x} f_2^{''} \Big\} e^{jkz} \tag{2.115}$$

In region ch_1, the fields due to $\mathbf{J}_1$ are written as follows.

$$\mathbf{E}^{t}_{ch_1}(\mathbf{J}_1) = \eta_{c_2} J_0 \Big\{ f_3^{''}(\hat{x} - j\hat{y}) e^{-jh_1 z} + f_4^{''}(\hat{x} + j\hat{y}) e^{-jh_2 z} \Big\} \tag{2.116}$$

$$\mathbf{H}^{t}_{ch_1}(\mathbf{J}_1) = J_0 \Big\{ f_3^{''}(\hat{y} + j\hat{x}) e^{-jh_1 z} + f_4^{''}(\hat{y} - j\hat{x}) e^{-jh_2 z} \Big\} \tag{2.117}$$

$$\mathbf{E}^{r}_{ch_1}(\mathbf{J}_1) = \eta_{c_2} J_0 \Big\{ f_5^{''}(\hat{x} + j\hat{y}) e^{jh_1 z} + f_6^{''}(\hat{x} - j\hat{y}) e^{jh_2 z} \Big\} \tag{2.118}$$

$$\mathbf{H}^{r}_{ch_1}(\mathbf{J}_1) = J_0 \Big\{ f_5^{''}(-\hat{y} + j\hat{x}) e^{jh_1 z} + f_6^{''}(-\hat{y} - j\hat{x}) e^{jh_2 z} \Big\} \tag{2.119}$$

Similarly, the fields in region d_2 are as follows.

$$\mathbf{E}^{t}_{d_2}(\mathbf{J}_1) = \eta J_0 \Big\{ \hat{x} f_7^{''} + \hat{y} f_8^{''} \Big\} e^{-jkz} \tag{2.120}$$

$$\mathbf{H}^{t}_{d_2}(\mathbf{J}_1) = J_0 \Big\{ \hat{y} f_7^{''} - \hat{x} f_8^{''} \Big\} e^{-jkz} \tag{2.121}$$

$$\mathbf{E}^{r}_{d_2}(\mathbf{J}_1) = \eta J_0 \Big\{ \hat{x} f_9^{''} + \hat{y} f_{10}^{''} \Big\} e^{jkz} \tag{2.122}$$

$$\mathbf{H}^{r}_{d_2}(\mathbf{J}_1) = J_0 \Big\{ -\hat{y} f_9^{''} + \hat{x} f_{10}^{''} \Big\} e^{jkz} \tag{2.123}$$

The reflected and the transmitted fields in region d_3 are given by

$$\mathbf{E}^{t}_{d_3}(\mathbf{J}_1) = \eta J_0 \Big\{ \hat{x} f_{11}^{''} + \hat{y} f_{12}^{''} \Big\} e^{-jkz} \tag{2.124}$$

$$\mathbf{H}^t_{d_3}(\mathbf{J}_1) = J_0\Big\{\hat{y}f^{''}_{11} - \hat{x}f^{''}_{12}\Big\}e^{-jkz} \tag{2.125}$$

$$\mathbf{E}^r_{d_3}(\mathbf{J}_1) = \eta J_0\Big\{\hat{x}f^{''}_{13} + \hat{y}f^{''}_{14}\Big\}e^{jkz} \tag{2.126}$$

$$\mathbf{H}^r_{d_3}(\mathbf{J}_1) = J_0\Big\{ -\hat{y}f^{''}_{13} + \hat{x}f^{''}_{14}\Big\}e^{jkz} \tag{2.127}$$

Similarly, the fields in region ch_2 are as follows.

$$\mathbf{E}^t_{ch_2}(\mathbf{J}_1) = \eta_{c_1} J_0\Big\{f^{''}_{15}(\hat{x} - j\hat{y})e^{-jh_3z} + f^{''}_{16}(\hat{x} + j\hat{y})e^{-jh_4z}\Big\} \tag{2.128}$$

$$\mathbf{H}^t_{ch_2}(\mathbf{J}_1) = J_0\Big\{f^{''}_{15}(\hat{y} + j\hat{x})e^{-jh_3z} + f^{''}_{16}(\hat{y} - j\hat{x})e^{-jh_4z}\Big\} \tag{2.129}$$

$$\mathbf{E}^r_{ch_2}(\mathbf{J}_1) = \eta_{c_1} J_0\Big\{f^{''}_{17}(\hat{x} + j\hat{y})e^{jh_3z} + f^{''}_{18}(\hat{x} - j\hat{y})e^{jh_4z}\Big\} \tag{2.130}$$

$$\mathbf{H}^r_{ch_2}(\mathbf{J}_1) = J_0\Big\{f^{''}_{17}(-\hat{y} + j\hat{x})e^{jh_3z} + f^{''}_{18}(-\hat{y} - j\hat{x})e^{jh_4z}\Big\} \tag{2.131}$$

Finally, the field in region d_4 due to $\mathbf{J}_1$ can be written as follows.

$$\mathbf{E}^t_{d_4}(\mathbf{J}_1) = \eta J_0\Big\{\hat{x}f^{''}_{19} + \hat{y}f^{''}_{20}\Big\}e^{-jkz} \tag{2.132}$$

$$\mathbf{H}^t_{d_4}(\mathbf{J}_1) = J_0\Big\{\hat{y}f^{''}_{19} - \hat{x}f^{''}_{20}\Big\}e^{-jkz} \tag{2.133}$$

The twenty unknown constants $f^{''}_1 - f^{''}_{20}$ are computed by satisfying the boundary conditions at the five interfaces ($z = -z_2, z = -z_1, z = 0, z = z_1, z = z_2$). The coefficients are computed numerically using MATLAB ®.

2.3.3 Fields Computation

To demonstrate the behavior of the electric and magnetic fields in various parts of the problem, we have computed the fields for a special case of $\mathrm{J}_0 = 1$ (A/m), $\epsilon_r = 2$, $\mu_r = 1$, $\gamma_1 = 0.005$, $d = 1$ m, $t = 0.1$ m and $f = 300$ MHz. The computed results are shown in Figs. 2.23 - 2.30. Figure 2.23 shows the real part

of x-component of the total electric field. There are three curves in this figure. It is seen that when $\gamma_2 = -\gamma_1$, the fields of the image problem are the same as the fields in the original problem. Where as, these two fields are not the same when $\gamma_2 = \gamma_1$ at $z = 0$, $z = -z_1$ and $z = -z_2$ interfaces. Note that total E_y is not zero at $z = 0$ interface, when $\gamma_2 \neq -\gamma_1$. This is clear from Figs. 2.25 and 2.26. The other six figures $(2.23, 2.24, 2.27 - 2.30)$ also support the conclusion that the image chiral material must have $\gamma_2 = -\gamma_1$.

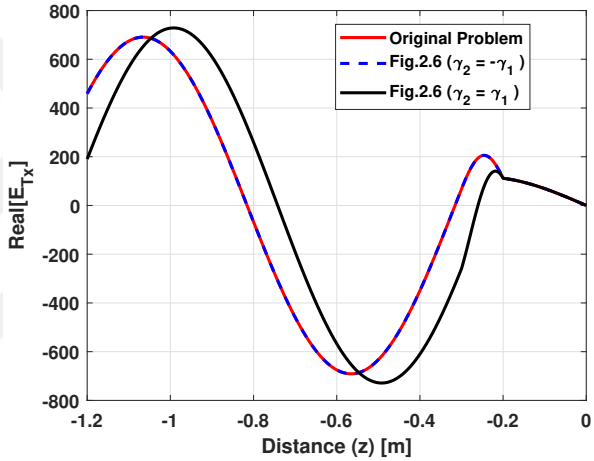

Figure 2.23: Real component of total E_x in Fig. 2.5 and Fig. 2.6 for a chiral slab parallel to a PEC plane problem.

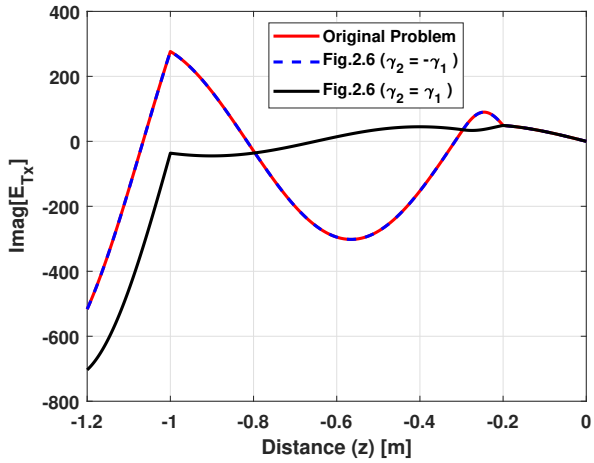

Figure 2.24: Imaginary component of total E_x in Fig. 2.5 and Fig. 2.6 for a chiral slab parallel to a PEC plane problem.

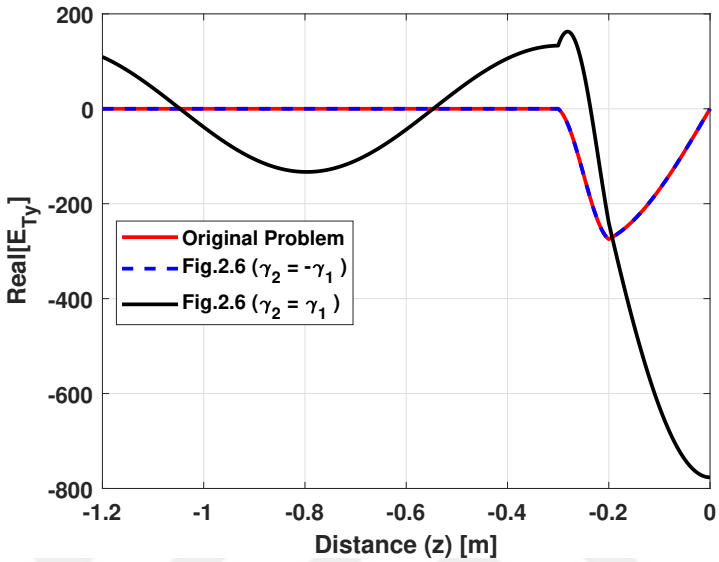

Figure 2.25: Real component of total E_y in Fig. 2.5 and Fig. 2.6 for a chiral slab parallel to a PEC plane problem.

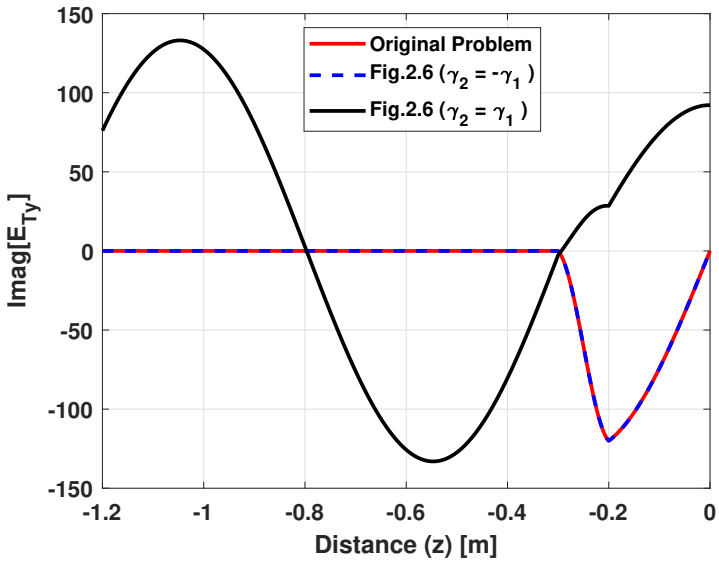

Figure 2.26: Imaginary component of total E_y in Fig. 2.5 and Fig. 2.6 for a chiral slab parallel to a PEC plane problem.

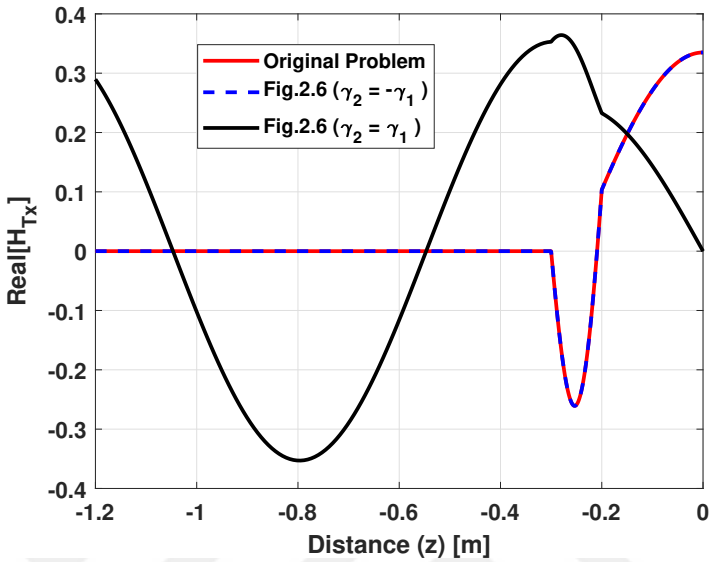

Figure 2.27: Real component of total H_x in Fig. 2.5 and Fig. 2.6 for a chiral slab parallel to a PEC plane problem.

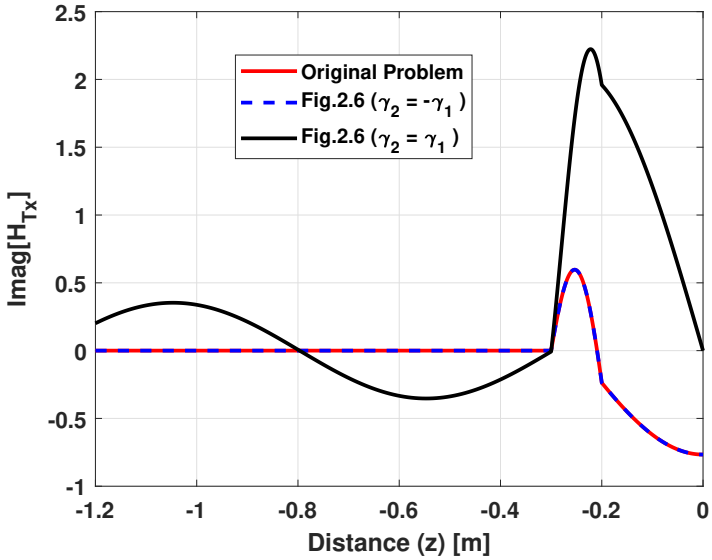

Figure 2.28: Imaginary component of total H_x in Fig. 2.5 and Fig. 2.6 for a chiral slab parallel to a PEC plane problem.

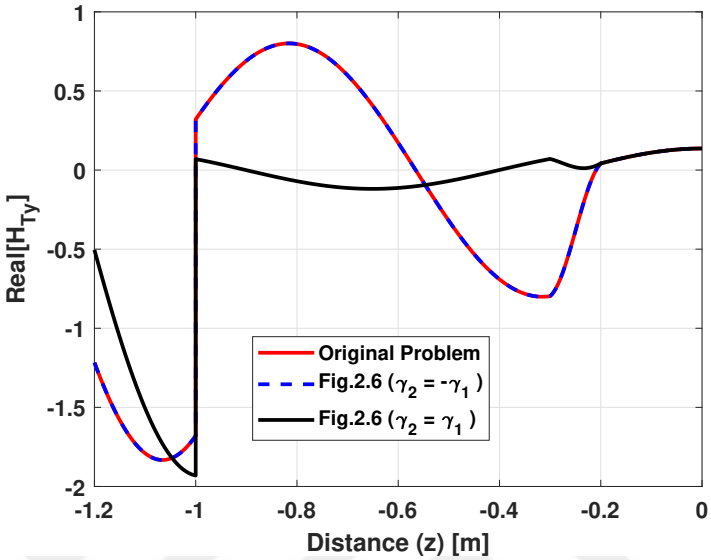

Figure 2.29: Real component of total H_y in Fig. 2.5 and Fig. 2.6 for a chiral slab parallel to a PEC plane problem.

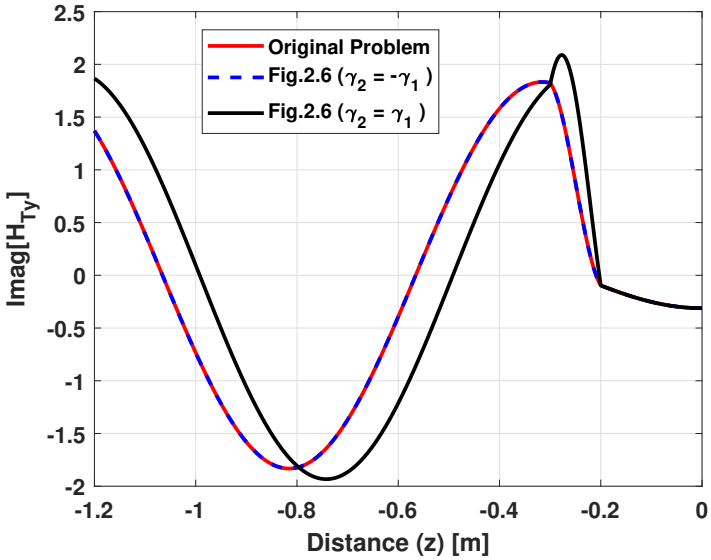

Figure 2.30: Imaginary component of total H_y in Fig. 2.5 and Fig. 2.6 for a chiral slab parallel to a PEC plane problem.

2.4 Summary

It is verified that the image of a chiral material through an infinite Perfect Electric Conductor (PEC) is another chiral material with the same permittivity and permeability but opposite chirality. This is done by solving three problems exactly. The source in these problems is an infinite electric current sheet parallel to the ground plane. In the first example, the current sheet is inside a chiral half-space. In the second example, the current sheet is outside a grounded chiral slab. In the third example, the slab is also away from the ground plane. A brief summary of plane waves in an unbounded chiral medium and the plane waves produced by an infinite electric current sheet is given in Appendix A.

Chapter 3

Electromagnetic Scattering from Chiral Cylinders of Arbitrary Cross-Sections above a Ground Plane

The main purpose of this work is to solve the problem of electromagnetic scattering from a two dimensional (2-D) homogeneous chiral cylinder of arbitrary cross-section above an infinite perfect electric conductor (PEC) plane. This problem is shown in Fig. 3.1. Here, a chiral cylinder of arbitrary cross-section S_1 is placed above an infinite PEC plane and is illuminated by a known incident plane wave. The purpose is to find the total field at any point above the plane. This problem is solved by first using the image theory to obtain two chiral cylinders in free-space. Then, the surface equivalence principle is used to obtain a set of coupled integral equations for the unknown equivalent surface currents on these two cylinders. Then, the Method of Moments (MoM) is used to solve these integral equations numerically. The moment matrix for this two-cylinder problem is unnecessarily large. The properties of the image body and the image source are used to reduce the size of the moment matrix. This matrix is named the Enhanced Moment Matrix.

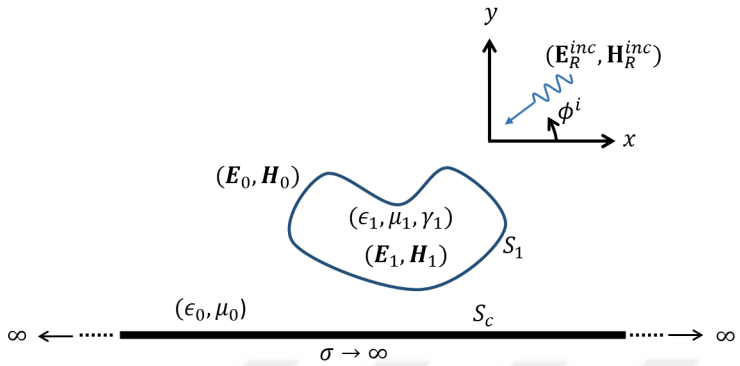

Figure 3.1: The original problem: A chiral cylinder above a ground plane illuminated by a plane wave.

The chiral cylinder in Fig. 3.1 is characterized by $(\epsilon_1, \mu_1, \gamma_1)$, where ϵ_1 is the permittivity of the body, μ_1 is the permeability, and γ_1 is the chiral admittance. It is placed above a PEC plane at $y = 0$, and is illuminated by an incident plane wave $(\mathbf{E}_R^{inc}, \mathbf{H}_R^{inc})$. The subscript R is used to show that this incident plane wave is due to a real impressed source. This incident wave is either a TM or a TE wave with an angle of incidence ϕ^i. The cylinder is surrounded by free-space (ϵ_0, μ_0). The surfaces of the ground plane and cylinder are denoted by S_c and S_1, respectively. The purpose is to find the total fields $(\mathbf{E}_0, \mathbf{H}_0)$ external to the cylinder, and $(\mathbf{E}_1, \mathbf{H}_1)$ internal to the cylinder.

Next, a detailed description of each method is presented.

3.1 Method of Images

3.1.1 The Original Problem

Consider the problem of electromagnetic scattering from two cylinders illuminated by two different plane waves as shown in Fig. 3.2. The cylinders may have different cross-sections S_1 and S_2, and different material parameters (ϵ, μ, γ).

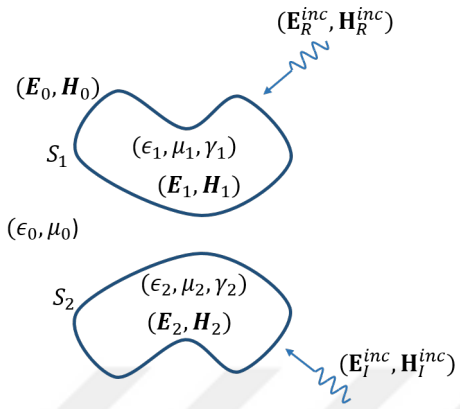

Figure 3.2: Scattering from two arbitrarily shaped chiral cylinders with different parameters excited by two different incident waves.

It is shown in [79] that the problem of Fig. 3.2 would be electromagnetically equivalent to the problem in Fig. 3.1 (for $y \geq 0$), if:

1. S_2 is the *mirror* image of S_1,
2. tangential component of $\mathbf{E}_I^{inc}$ is negative of the tangential component of $\mathbf{E}_R^{inc}$ at $y = 0$,
3. $\epsilon_2 = \epsilon_1$, $\mu_2 = \mu_1$, and
4. $\gamma_2 = -\gamma_1$.

In this "electromagnetic image problem", the PEC plane of Fig. 3.1 is replaced by an image cylinder characterized by $(\epsilon_1, \mu_1, -\gamma_1)$ and an image plane wave $(\mathbf{E}_I^{inc}, \mathbf{H}_I^{inc})$. The subscript I is used to show that this incident plane wave is due to an image impressed source.

In this section, we will present the procedure to solve the two-cylinder problem shown in Fig. 3.2, where the cylinders are assumed to be arbitrary. We will use the surface equivalence principle to obtain some coupled integral equations for unknown equivalent surface electric and magnetic currents. We will then solve these integral equations numerically by using MoM. We will also present some results. All computed results are given for the cases where the first three of the

above four conditions are satisfied. However, in some cases, γ_2 is assumed to be equal to γ_1, and in some special cases, γ_2 is taken to be $-\gamma_1$.

3.1.2 Surface Integral Formulation

The equivalence principle allows for the decomposition of the multi-region problem into simpler one-region problems. Each of these one-region problems is simpler than the original. In other words, in the equivalence principle, our goal is often to remove some object(s) in a problem space to make the region homogeneous by adding the "equivalent" sources on a boundary that divides the solution space.

This two-body problem is solved by using the surface equivalence principle and the method of moments. Here, the surface equivalence principle is used to obtain three equivalent problems for three different regions of Fig. 3.2.

3.1.2.1 External Equivalence

Figure 3.3 shows an equivalent problem for the problem of Fig. 3.2 external to the surfaces S_1 and S_2. Here, the whole space is characterized by (ϵ_0, μ_0). The two incident plane waves of Fig. 3.2 are also kept in Fig. 3.3. The total fields inside the fictitious surfaces S_1 and S_2 of Fig. 3.3 are assumed to be zero. The total fields at any point outside these surfaces are assumed to be the same as the total field $(\mathbf{E}_0, \mathbf{H}_0)$ at the same point of Fig. 3.2. To support the discontinuities of the fields at the surface S_1, equivalent electric and magnetic surface currents $(\mathbf{J}_1, \mathbf{M}_1)$ are placed on this surface. Similarly, equivalent electric and magnetic surface currents $(\mathbf{J}_2, \mathbf{M}_2)$ are placed on the surface S_2. When the fields radiated by these four surface currents are added to the incident fields in Fig. 3.3, the result is equal to $(\mathbf{E}_0, \mathbf{H}_0)$ at any point external to S_1 and S_2 of Fig. 3.2. However, at any point inside these two surfaces, the sum is equal to zero. In other words,

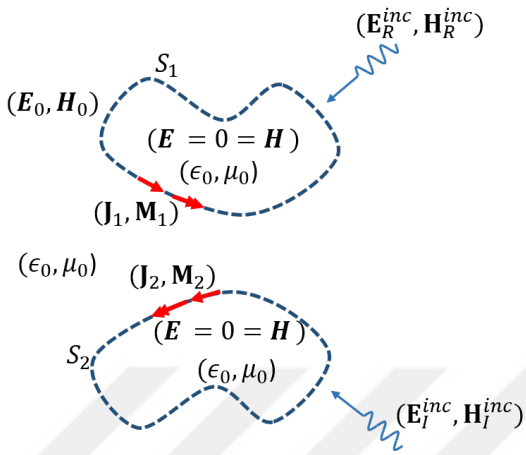

Figure 3.3: External equivalence for the problem of Fig. 3.2.

$$\mathbf{E}^0_{tan}(\mathbf{J}_1, \mathbf{M}_1) + \mathbf{E}^0_{tan}(\mathbf{J}_2, \mathbf{M}_2) = -\left[\mathbf{E}_R^{inc} + \mathbf{E}_I^{inc}\right]_{tan} \quad on \quad S_1^- \tag{3.1}$$

$$\mathbf{E}^0_{tan}(\mathbf{J}_1, \mathbf{M}_1) + \mathbf{E}^0_{tan}(\mathbf{J}_2, \mathbf{M}_2) = -\left[\mathbf{E}_R^{inc} + \mathbf{E}_I^{inc}\right]_{tan} \quad on \quad S_2^- \tag{3.2}$$

Here, the subscript *tan* denotes the tangential component and the superscirpt "0" denotes that surface currents are radiating in an unbounded external medium (ϵ_0, μ_0). S_1^- and S_2^- refer to the surface just inside S_1 and S_2, respectively. Obviously, similar equations apply for the tangential component of the magnetic field.

3.1.2.2 Internal Equivalence-1

Figure 3.4 shows an equivalent problem for the problem of Fig. 3.2 internal to the surface S_1. Here, the whole space is characterized by $(\epsilon_1, \mu_1, \gamma_1)$. The two incident plane waves of Fig. 3.2 are absent here in Fig. 3.4. The total fields outside the fictitious surface S_1 of Fig. 3.4 are assumed to be zero. The total fields at any point inside S_1 are assumed to be the same as the total fields $(\mathbf{E}_1, \mathbf{H}_1)$ at the same point of Fig. 3.2. To support the discontinuities of the fields at the surface S_1, equivalent electric and magnetic surface currents $(-\mathbf{J}_1, -\mathbf{M}_1)$ are placed on this surface. The fields radiated by these two currents (in the unbounded medium $(\epsilon_1, \mu_1, \gamma_1)$) are the same as $(\mathbf{E}_1, \mathbf{H}_1)$ at any point inside S_1

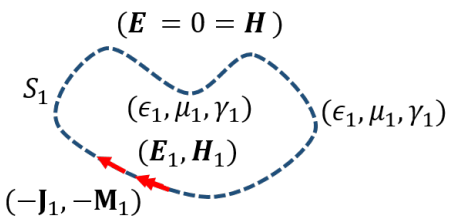

Figure 3.4: Internal equivalence for the real body.

of Fig. 3.2. However, at any point outside S_1, the fields radiated by these surface currents are zero. In other words,

$$\mathbf{E}^1_{tan}(\mathbf{J}_1, \mathbf{M}_1) = 0 \quad on \quad S_1^+ \tag{3.3}$$

where, the superscirpt "1" denotes that surface currents are radiating in an unbounded medium characterized by $(\epsilon_1, \mu_1, \gamma_1)$, and S_1^+ refers to the surface just outside S_1 . Obviously, a similar equation applies for the tangential components of the magnetic field.

3.1.2.3 Internal Equivalence-2

Figure 3.5 shows an equivalent problem for the problem of Fig. 3.2 internal to the surface S_2. Here, the whole space is characterized by $(\epsilon_2, \mu_2, \gamma_2)$. The two incident plane waves of Fig. 3.2 are absent here in Fig. 3.5. The total fields outside the fictitious surface S_2 of Fig. 3.5 are assumed to be zero. The total fields at any point inside S_2 are assumed to be the same as the total fields $(\mathbf{E}_2, \mathbf{H}_2)$ at the same point of Fig. 3.2. To support the discontinuities of the fields at the surface S_2, equivalent electric and magnetic surface currents $(-\mathbf{J}_2, -\mathbf{M}_2)$

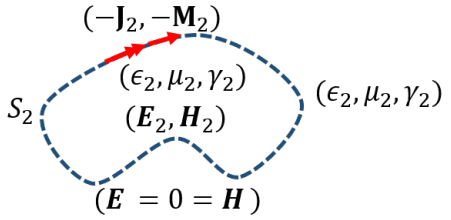

Figure 3.5: Internal equivalence for the image body.

are placed on this surface. The fields radiated by these two currents are the same as $(\mathbf{E}_2, \mathbf{H}_2)$ at any point inside S_2. However, at any point outside S_2, the fields radiated by these surface currents are zero. In other words,

$$\mathbf{E}^2_{tan}(\mathbf{J}_2, \mathbf{M}_2) = 0 \quad on \quad S_2^+ \tag{3.4}$$

where, the superscript "2" denotes that surface currents are radiating in an unbounded medium characterized by $(\epsilon_2, \mu_2, \gamma_2)$, and S_2^+ refers to the surface just outside S_2. Obviously, a similar equation applies for the tangential components of the magnetic field.

3.1.3 Application of the Moment Matrix

The Moment Method is used to find the approximate solution to the proposed problem. Equations $(3.1 - 3.4)$ represent four coupled integral equations for the four unknown currents $(\mathbf{J}_1, \mathbf{M}_1, \mathbf{J}_2, \mathbf{M}_2)$. These equations are called EFIE (Electric Field Integral Equations). They are solved here numerically using the method of moments. There are five steps involved in the Moment Method. In the first step, the region bounded by the surface is discretized by N linear segments. Then, on each discretized segment, the unknowns are expressed in terms of suitable expansion functions. In the third step, the fields produced by the expansion functions are tested by the weighting functions. The testing procedure produces N linear equations for N unknown expansion functions. Using these linear equations, a *moment matrix* is constructed in the fourth step. The final step involves the computation of the unknown expansion coefficients. Once, the expansion coefficients are determined, then the other quantities of interest such as equivalent surface currents on the body, scattered fields in the near- and far-field regions can easily be computed.

3.1.3.1 Discretization

First the cross-sections S_1 and S_2 are each approximated by N linear segments as shown in Fig. 3.6. (At this point number of sections on S_1 and S_2 do not have

to be the same. However, later we will specialize S_2 to be the mirror image of S_1. Then, the number of segments on S_2 must be the same as those on S_1). The number or the lengths of the segments are chosen by the wavelength (λ) in the medium. While discretizing the surface, the lengths of the segments are chosen in a manner that there must be a physical similarity to the shape of the object. For instance, a discretized circle should appear round.

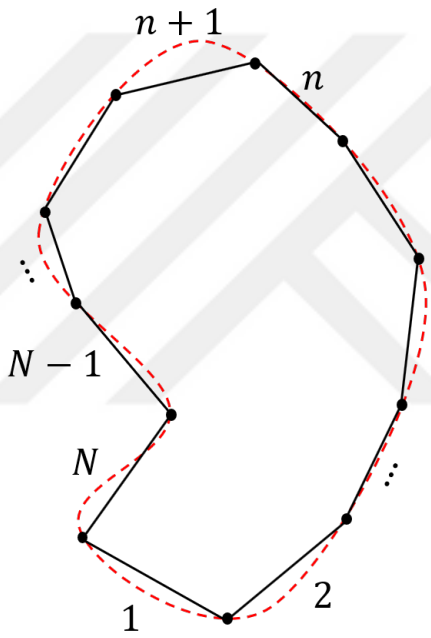

Figure 3.6: Surface S discretized into N linear segments.

3.1.3.2 Expansion Functions

In this step, the unknown surface currents are approximated by known expansion functions on the discrete segments of the surface S. On each segment, there are four unknown currents: the $z-$ and the lateral component of the electric current, and the $z-$ and the lateral component of the magnetic current. In this work, pulses are used as expansion functions. In other words, we let

$$\mathbf{J}_1 = \hat{z} \sum_{n=1}^{N} a_n P_n^1 + \sum_{n=1}^{N} \hat{t}_n^1 b_n P_n^1 \tag{3.5}$$

$$\mathbf{M}_1 = \hat{z} \sum_{n=1}^{N} c_n P_n^1 + \sum_{n=1}^{N} \hat{t}_n^1 d_n P_n^1 \tag{3.6}$$

$$\mathbf{J}_2 = \hat{z} \sum_{n=N+1}^{2N} e_n P_n^2 + \sum_{n=N+1}^{2N} \hat{t}_n^2 f_n P_n^2 \tag{3.7}$$

$$\mathbf{M}_2 = \hat{z} \sum_{n=N+1}^{2N} g_n P_n^2 + \sum_{n=N+1}^{2N} \hat{t}_n^2 h_n P_n^2 \tag{3.8}$$

Here, $a - h$ are the unknown expansion coefficients. $\hat{z}$ denotes the unit vector in the longitudinal direction, and $\hat{t}_n^1$ ($\hat{t}_n^2$) represents the unit vector tangent to the n^{th} segment (counter-clockwise in the lateral direction) on surface S_1 (S_2), and P_n^1 (P_n^2) is the unit pulse function defined on n^{th} segment of S_1 (S_2).

For instance, a_n is the unknown expansion coefficient for the pulse current that exists on the n^{th} segment of the surface S_1. This is a constant, z-directed, electric current of density 1 (A/m). The pulse function is illustrated in Fig. 3.7.

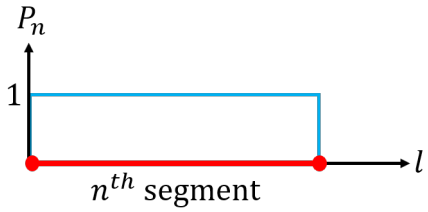

Figure 3.7: The pulse function.

Similarly, b_n is the unknown expansion coefficient that exists on the n^{th} segment of the surface S_1 due to a constant, circumferential-directed, electric current of density 1 (A/m). The charge associated with the lateral current of the m^{th} segment is approximated by two displaced pulses as shown in Fig. 3.8 [85–87]. These charge pulses are shifted by a half segment with respect to the current pulses. The n^{th} expansion function associated with the longitudinal and lateral directed magnetic currents on S_1 are c_n and d_n, respectively.

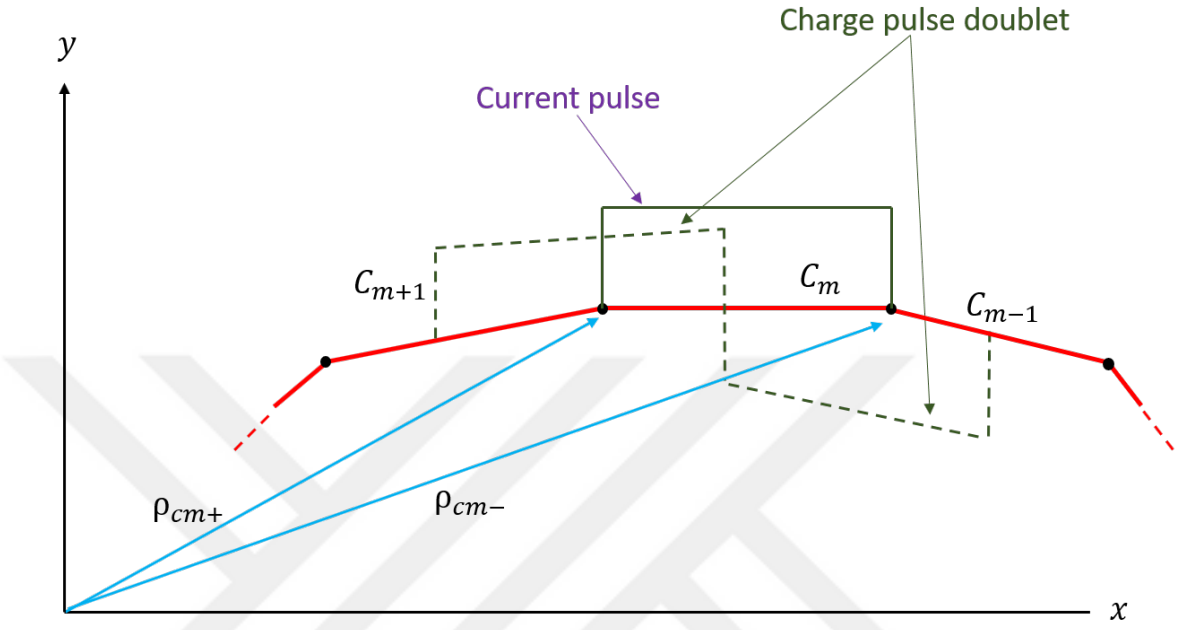

Figure 3.8: The charge associated with the pulse currents on the n^{th} segment.

3.1.3.3 Testing Functions and the Moment Matrix

To find the above $8N$ unknown expansion coefficients, $(3.5-3.8)$ are inserted in the integral equation $(3.1-3.4)$ and by using an approximate Galerkin's method as in [44], the matrix equation (3.9) is obtained. The $8N \times 8N$ matrix on the left-hand side of (3.9) is known as the Moment Matrix. Each element of this moment matrix is a $N \times N$ sub-matrix. The first letter in the name of the sub-matrices in (3.9) denotes the component of the field. The second letter denotes the source of the field, while the subscript of the second letter denotes the component of the source current. The third number (1 or 2) represents the body where the field is computed. The fourth number (1 or 2) represents the body where the source current resides. Finally, the last number denotes the unbounded medium $(0, 1,$ or 2) in which the source radiates. For instance, an element in the m^{th} row and the n^{th} column of the sub-matrix $\mathrm{ZJ_Z110}$ is the z-component of the electric field on the m^{th} segment of S_1, produced by $\mathrm{J_Z}$ on the n^{th} segment of S_1, when this

J_Z radiates in the unbounded medium (ϵ_0, μ_0).

$$\begin{bmatrix} ZJ_Z110 & ZJ_L110 & ZM_Z110 & ZM_L110 & ZJ_Z120 & ZJ_L120 & ZM_Z120 & ZM_L120 \\ LJ_Z110 & LJ_L110 & LM_Z110 & LM_L110 & LJ_Z120 & LJ_L120 & LM_Z120 & LM_L120 \\ ZJ_Z210 & ZJ_L210 & ZM_Z210 & ZM_L210 & ZJ_Z220 & ZJ_L220 & ZM_Z220 & ZM_L220 \\ LJ_Z210 & LJ_L210 & LM_Z210 & LM_L210 & LJ_Z220 & LJ_L220 & LM_Z220 & LM_L220 \\ ZJ_Z111 & ZJ_L111 & ZM_Z111 & ZM_L111 & 0 & 0 & 0 & 0 \\ LJ_Z111 & LJ_L111 & LM_Z111 & LM_L111 & 0 & 0 & 0 & 0 \\ 0 & 0 & 0 & 0 & ZJ_Z222 & ZJ_L222 & ZM_Z222 & ZM_L222 \\ 0 & 0 & 0 & 0 & LJ_Z222 & LJ_L222 & LM_Z222 & LM_L222 \end{bmatrix} \begin{bmatrix} a \\ b \\ c \\ d \\ e \\ f \\ g \\ h \end{bmatrix} = \begin{bmatrix} -Zinc1 \\ -Linc1 \\ -Zinc2 \\ -Linc2 \\ 0 \\ 0 \\ 0 \\ 0 \end{bmatrix} \quad (3.9)$$

Similarly, an element in the m^{th} row and the n^{th} column of the sub-matrix LJ_L110 is the lateral component of the electric field on the m^{th} segment of S_1, produced by J_L on the n^{th} segment of S_1, when this J_L radiates in the unbounded medium (ϵ_0, μ_0).

The sub-matrices $ZJ_L110, ZM_Z110, ZJ_L120, ZM_Z120$, $ZJ_L210, ZM_Z210, ZJ_L220$, and ZM_Z220 are identically zero.

The sub-matrices in the 2^{nd} row of (3.9) contain the lateral field on S_1, produced by different sources radiating in the unbounded medium (ϵ_0, μ_0). Therefore, LJ_Z110, LM_L110, LJ_Z120, and LM_L120 are identically zero. Similarly, the sub-matrices $LJ_Z210, LM_L210, LJ_Z220$, and LM_L220 are identically zero.

An element in the m^{th} row and the n^{th} column of the sub-matrix LM_L111 is the lateral component of the electric field on the m^{th} segment of S_1, produced by

M_L on the n^{th} segment of S_1, when this M_L radiates in the unbounded medium $(\epsilon_1, \mu_1, \gamma_1)$.

The $8N \times 1$ column matrix on the left-hand side of (3.9) contains the unknown expansion coefficients. The $N \times 1$ sub-matrices a and e contain the expansion coefficients for J_Z on S_1 and S_2, respectively. Similarly, b and f contain the expansion coefficients for J_L, and c and g contain the expansion coefficients for M_Z, and finally, d and h contain the expansion coefficients for M_L.

The m^{th} element of $N \times 1$ sub-matrix $-$Zinc1 on the right-hand side of (3.9) is equal to the negative of the z-component of the total incident electric field on the m^{th} segment of S_1. Similarly, the sub-matrix $-$Zinc2 contains the negative of the z-component of the total incident electric field on S_2. The m^{th} element of the sub-matrices $-$Linc1 and $-$Linc2 represent the lateral component of the total incident electric field on the m^{th} segment of S_1 and S_2, respectively.

The computational details of each element of the moment matrix are given in Appendix C.

3.1.3.4 Near Field Computation

Once (3.9) is solved for the unknown expansion coefficients, all four components of the equivalent surface currents can be found using (3.5) - (3.8). With these currents, the internal and external fields can be computed everywhere using (B.35) and (B.36). Note that these field equations reduce to usual free-space equations when the value of chiral admittance (γ) is set to zero. A detailed description of two-dimensional fields in chiral media is presented in Appendix B.

3.1.3.5 Radar Cross-Section (RCS)

The scattered width at any point in space in cylindrical coordinates [88] can be written as

$$\sigma(\phi) = \lim_{\rho\to\infty} 2\pi\rho \left| \frac{\mathbf{E}^s}{\mathbf{E}^{inc}} \right|^2 \tag{3.10}$$

Where ρ is the distance from the origin of the surface S to the observation point and ϕ is the angle of the observation point. In (3.10), the scattered and incident fields are denoted by $\mathbf{E}^s$ and $\mathbf{E}^{inc}$, respectively. In general, the surface currents $(\mathbf{J}, \mathbf{M})$ have both z- and lateral components. Therefore, the scattered field must have co- and cross-polarized components. The radar cross-section for the two components can be written as follows.

$$\sigma_z(\phi) = \frac{k_0}{4} \left| \sum_{n=1}^{N} l_{n_1} \Big(a_n - \frac{d_n}{\eta_0} \hat{t}_n^1 \cdot \hat{a}_\phi \Big) e^{jk_0\rho^{n_1} cos(\phi - \phi^{n_1})} + \sum_{n=N+1}^{2N} l_{n_2} \Big(e_n - \frac{h_n}{\eta_0} \hat{t}_n^2 \cdot \hat{a}_\phi \Big) e^{jk_0\rho^{n_2} cos(\phi - \phi^{n_2})} \right|^2 \tag{3.11}$$

$$\sigma_\phi(\phi) = \frac{k_0}{4} \left| \sum_{n=1}^{N} l_{n_1} \Big(\frac{c_n}{\eta_0} + b_n \hat{t}_n^1 \cdot \hat{a}_\phi \Big) e^{jk_0\rho^{n_1} cos(\phi - \phi^{n_1})} + \sum_{n=N+1}^{2N} l_{n_2} \Big(\frac{g_n}{\eta_0} + f_n \hat{t}_n^2 \cdot \hat{a}_\phi \Big) e^{jk_0\rho^{n_2} cos(\phi - \phi^{n_2})} \right|^2 \tag{3.12}$$

where, σ denotes the bistatic radar scattering width, l_{n_1} (l_{n_2}) is the length of the n^{th} segment on S_1 (S_2), $\hat{a}_\phi$ is the unit vector in the ϕ-direction at the field point, ρ^{n_1} (ρ^{n_2}) and ϕ^{n_1} (ϕ^{n_2}) are the cylindrical coordinates of the center of the n^{th} segment on S_1 (S_2), η_0 is the free-space wave impedance, and k_0 is the free-space wavenumber.

3.1.4 Numerical Results of Two Chiral Cylinders

Consider a system of two circular chiral cylinders as shown in Fig. 3.9. The cylinders could have completely different cross-sections. However, in this section, the cylinder in the lower half-space is deliberately chosen to be the mirror image of the upper cylinder. The radius r of the cylinders is $0.5\lambda_0$, and the distance d from the center of the cylinders to $y = 0$ plane is λ_0. Where, λ_0 is the free-space wavelength and assumed to be 1 meter. Both cylinders have $(\epsilon_r = 4, \mu_r = 1)$. Three different values will be assumed for their chiral admittance γ:
(i). $\gamma_1 = \gamma_2 = 0.0$,
(ii). $\gamma_1 = \gamma_2 = 0.0005$, and
(iii). $\gamma_1 = -\gamma_2 = 0.0005$.

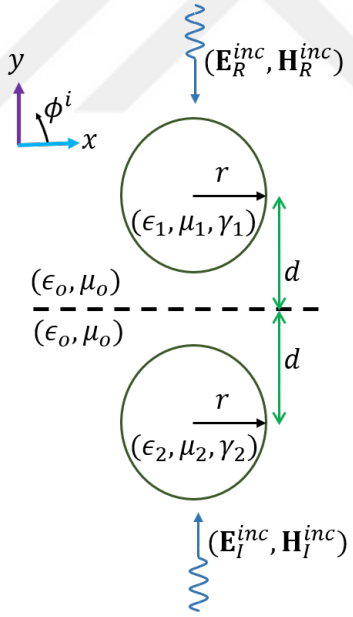

Figure 3.9: Two circular chiral cylinders illuminated by two plane waves.

The system is illuminated by two TM plane waves. $\mathbf{E}_R^{inc}$ is equal to $\hat{z}1$ (V/m) with incident angle $\phi^i = 90^o$ and $\mathbf{E}_I^{inc}$ is equal to -$\hat{z}1$ (V/m) with incident angle $\phi^i = -90^o$. To use MoM, each cylinder is approximated by $N = 90$ segments.

Using MoM, we first computed the equivalent surface currents (which are not shown here), and then we can find the fields produced by these currents at any point.

Figure 3.10 shows the magnitude of the total tangential electric field ($\sqrt{|E_x|^2 + |E_z|^2}$) at $y = 0$ plane of the problem shown in Fig. 3.9. This field is the sum of the two incident fields and the fields radiated by the equivalent surface currents on both cylinders, when these currents radiate in the unbounded medium (ϵ_0, μ_0), as suggested by Fig. 3.3. The results in Fig. 3.10 for the case of $\gamma = 0$ are in an excellent agreement for those obtained by the methods used in [89].

The red curve in Fig. 3.10 (for the case $\gamma_1 = \gamma_2 = 0$) shows that the total tangential electric field is zero at $y = 0$ plane.

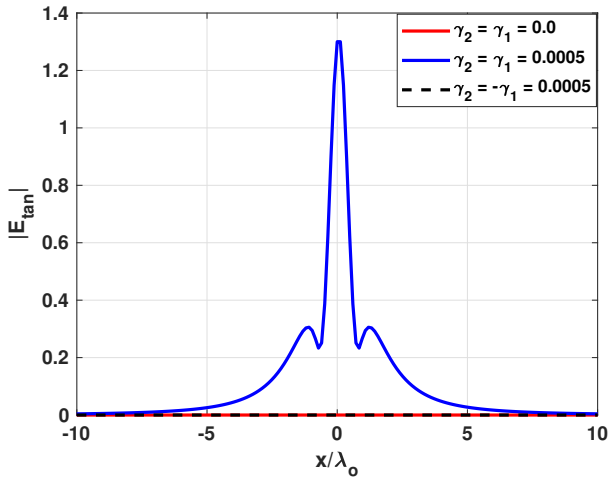

Figure 3.10: Magnitude of the total tangential electric field at $y = 0$ plane of Fig. 3.9.

We also noticed that the currents (not shown here) in the lower cylinder are the images of those on the upper cylinder. These results are expected and agree very well with those presented in [89]. Therefore, it is verified that the image of a dielectric cylinder above a PEC plane is the same dielectric cylinder.

The same results are observed for the dotted black curve in Fig. 3.10 (for the case $\gamma_1 = -\gamma_2 = 0.0005$), and therefore we can conclude that the image of a chiral cylinder through a PEC plane is another chiral cylinder with real chirality equal to negative of chirality of the original cylinder.

The blue curve in Fig. 3.10 (for the case $\gamma_1 = \gamma_2 = 0.0005$) shows that the total tangential electric field is not zero at $y = 0$ plane. We also observed that the currents (not shown here) on the lower cylinder are not the image of those on the upper cylinder. Therefore, we conclude that the image of a chiral cylinder through a PEC plane is not another chiral cylinder with the same chirality.

3.2 Enhanced Moment Matrix Method

As mentioned before, the moment matrix in (3.9) is unnecessarily large. When correct image theory is used, the equivalent surface currents on the image cylinder are the image of the equivalent currents on the real cylinder. Then, the number of unknowns in (3.9) would reduce to $4N$ (from $8N$).

To further demonstrate the relationship between the equivalent surface currents on two chiral cylinders, we consider the simple problem shown in Fig. 3.11. Both cylinders have ($\epsilon_r = 4, \mu_r = 1$), and the side lengths (L_x and L_y) are $0.2\lambda_0$. These cylinders are placed at distance $d = 0.5\lambda_0$ away from the $y = 0$ plane. Here, the cylinders are the mirror image of each other and each is approximated by $N = 3$ segments. (Segment-4 is the image of segment-1, segment-5 is the image of segment-2, and segment-6 is the image of segment-3). The two incident fields are also the image of each other.

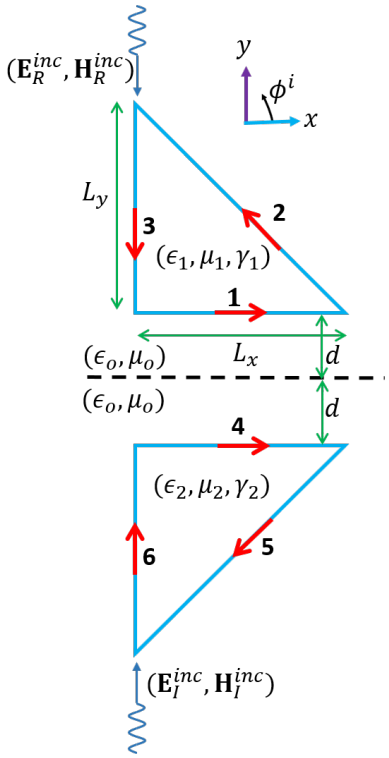

Figure 3.11: Two triangular chiral cylinders illuminated by two plane waves.

Currents	$\gamma_1 = \gamma_2 = 0$	
	Seg-1 (S_1)	Seg-4 (S_2)
J_Z	3.4401 - j0.2069	-3.4401 + j0.2069
J_L	0	0
M_Z	0	0
M_L	-0.3748 + j0.0208	-0.3748 + j0.0208

(a) Currents on segment-1 and segment-4

Currents	$\gamma_1 = \gamma_2 = 0$	
	Seg-2 (S_1)	Seg-5 (S_2)
J_Z	-0.7328 - j0.1839	0.7328 + j0.1839
J_L	0	0
M_Z	0	0
M_L	-0.5655 - j1.3531	-0.5655 - j1.3531

(b) Currents on segment-2 and segment-5

Currents	$\gamma_1 = \gamma_2 = 0$	
	Seg-3 (S_1)	Seg-6 (S_2)
J_Z	0.5142 - j0.5561	-0.5142 + j0.5561
J_L	0	0
M_Z	0	0
M_L	-0.6372 - j1.3132	-0.6372 - j1.3132

(c) Currents on segment-3 and segment-6

Table 3.1: TM excitation, Dielectric Case

The computed results for the surface currents are shown in Table 3.1 for the case of simple dielectric $\epsilon_r = 4, \mu_r = 1$, and $\gamma_1 = \gamma_2 = 0$. In this case, the lower body is the correct image of the upper body. Hence, we expect that the currents on the lower body should be the image of the currents on the upper body. We see from Table 3.1 that J_Z on an image segment is negative of J_Z on the corresponding original segment. That is, $J_{Z4} = -J_{Z1} = -3.4401 + j0.2069$, $J_{Z5} = -J_{Z2} = 0.7328 + j0.1839$, and $J_{Z6} = -J_{Z3} = -0.5142 + j0.5561$. Therefore, we can see that for the simple dielectric case the expected relationship

$$e_{n+N} = -a_n \,, \quad (n = 1, \cdots, N) \tag{3.13}$$

Currents	$\gamma_1 = -\gamma_2 = 0.0005$	
	Seg-1 (S_1)	Seg-4 (S_2)
J_Z	3.2520 - j0.2121	-3.2520 + j0.2121
J_L	0.1305 + j0.1165	-0.1305 - j0.1165
M_Z	0.0861 + j0.0139	0.0861 + j0.0139
M_L	-0.3235 + j0.0827	-0.3235 + j0.0827

(a) Currents on segment-1 and segment-4

Currents	$\gamma_1 = -\gamma_2 = 0.0005$	
	Seg-2 (S_1)	Seg-5 (S_2)
J_Z	-0.8314 - j0.1334	0.8314 + j0.1334
J_L	-0.0490 + j0.0580	0.0490 - j0.0580
M_Z	0.0040 + j0.0919	0.0040 + j0.0919
M_L	-0.4409 - j1.3418	-0.4409 - j1.3418

(b) Currents on segment-2 and segment-5

Currents	$\gamma_1 = -\gamma_2 = 0.0005$	
	Seg-3 (S_1)	Seg-6 (S_2)
J_Z	0.3985 - j0.4583	-0.3985 + j0.4583
J_L	0.0554 + j0.0599	-0.0554 - j0.0599
M_Z	0.0643 + j0.0799	0.0643 + j0.0799
M_L	-0.5091 - j1.3083	-0.5091 - j1.3083

(c) Currents on segment-3 and segment-6

Table 3.2: TM excitation, Chiral Case (Opposite Chiral Admittance)

is satisfied.

Note also that $M_{L4} = M_{L1} = -0.3748 + j0.0208$ in Table 3.1. According to image theory, the actual M_L current on segment-6 must be negative of the M_L current on segment-3. Since, the arrow on segment-6 is in opposite direction to the arrow on segment-3, we see from Table 3.1 that $M_{L6} = M_{L3} = -0.6372 - j1.3132$. Similarly, we see that M_{L5} is the image of M_{L2}. Therefore, we can see that for the simple dielectric case the expected relationship

$$h_{n+N} = d_n \,, \quad (n = 1, \cdots, N) \tag{3.14}$$

Currents	$\gamma_1 = \gamma_2 = 0.0005$	
	Seg-1 (S_1)	Seg-4 (S_2)
J_Z	3.3523 - j0.1889	-3.3523 + j0.1889
J_L	-0.0863 - j0.1103	-0.0863 - j0.1103
M_Z	-0.0333 - j0.0031	0.0333 + j0.0031
M_L	-0.3448 + j0.0461	-0.3448 + j0.0461

(a) Currents on segment-1 and segment-4

Currents	$\gamma_1 = \gamma_2 = 0.0005$	
	Seg-2 (S_1)	Seg-5 (S_2)
J_Z	-0.7711 - j0.1465	0.7711 + j0.1465
J_L	0.0707 + j0.0506	0.0707 + j0.0506
M_Z	0.0709 + j0.0410	-0.0709 - j0.0410
M_L	-0.5062 - j1.3663	-0.5062 - j1.3663

(b) Currents on segment-2 and segment-5

Currents	$\gamma_1 = \gamma_2 = 0.0005$	
	Seg-3 (S_1)	Seg-6 (S_2)
J_Z	0.4771 - j0.4932	-0.4771 + j0.4932
J_L	0.0733 + j0.1874	0.0733 + j0.1874
M_Z	0.1133 + j0.0516	-0.1133 - j0.0516
M_L	-0.5765 - j1.3319	-0.5765 - j1.3319

(c) Currents on segment-3 and segment-6

Table 3.3: TM excitation, Chiral Case (Same Chiral Admittance)

is satisfied.

The computed results for the surface currents are shown in Table 3.2 for the case of two chiral cylinders with $\epsilon_r = 4, \mu_r = 1$, and $\gamma_1 = -\gamma_2 = 0.0005$. In this case, the lower chiral body is the correct image of the upper chiral body. Therefore, the equivalent currents on the lower body must be the image of the currents on the upper body. This is correctly shown in Table 3.2. Therefore, for the correct image problem, in addition to (3.13) and (3.14), the following equations are satisfied.

$$f_{n+N} = -b_n \,, \quad (n = 1, \cdots, N) \tag{3.15}$$

$$g_{n+N} = c_n \ , \quad (n = 1, \cdots, N) \tag{3.16}$$

The computed results for the surface currents are shown in Table 3.3 for the case of two identical chiral cylinders with $\epsilon_r = 4, \mu_r = 1$, and $\gamma_1 = \gamma_2 = 0.0005$. Without going into the details, we see that (3.15) and (3.16) are not satisfied in this case. Hence, we can quickly conclude that the lower body with $\gamma_1 = \gamma_2$ cannot be the correct image of the original body.

Consider Fig. 3.2. Let us assume that it represents the correct image problem. That is, S_2 is the mirror image of S_1, the parameters of S_2 are equal to $(\epsilon_1, \mu_1, -\gamma_1)$, and the incident field $(\mathbf{E}_I^{inc}, \mathbf{H}_I^{inc})$ is the image field of the original field $(\mathbf{E}_R^{inc}, \mathbf{H}_R^{inc})$. Then, from the proceeding discussions, it was concluded that the equivalent currents on S_2 are the image of currents on S_1. Then, knowing $a_n, n = 1, \ldots, N$, one knows e_n, $n = N+1, \ldots, 2N$. Similarly, knowing b_n, one knows f_n, and knowing c_n, one knows g_n, and finally knowing d_n, one knows h_n. With these in mind, we can reduce the eight equations in (3.9) to four equations as follows.

Remembering that some of the sub-matrices in (3.9) are identically zero, then by adding the 1^{st} row to the 5^{th} row, and using $(3.13 - 3.16)$, we get

$$\begin{aligned}\Big\{\mathrm{ZJ_Z}110 - \mathrm{ZJ_Z}120 + \mathrm{ZJ_Z}111\Big\}a_n + \Big\{\mathrm{ZJ_L}111\Big\}b_n \\ + \Big\{\mathrm{ZM_Z}111\Big\}c_n + \Big\{\mathrm{ZM_L}110 + \mathrm{ZM_L}120 + \mathrm{ZM_L}111\Big\}d_n \\ = -\mathrm{Zinc1}\end{aligned} \tag{3.17}$$

Similarly, adding the 2^{nd} row to the 6^{th} row, we get

$$\begin{aligned}\Big\{\mathrm{LJ_Z}111\Big\}a_n + \Big\{\mathrm{LJ_L}110 - \mathrm{LJ_L}120 + \mathrm{LJ_L}111\Big\}b_n \\ + \Big\{\mathrm{LM_Z}110 + \mathrm{LM_Z}120 + \mathrm{LM_Z}111\Big\}c_n + \Big\{\mathrm{LM_L}111\Big\}d_n \\ = -\mathrm{Linc1}\end{aligned} \tag{3.18}$$

Adding the 3^{rd} row to the 7^{th} row, we get

$$\Big\{\mathrm{ZJ_Z}210 - \mathrm{ZJ_Z}220 - \mathrm{ZJ_Z}222\Big\}a_n + \Big\{\mathrm{ZJ_L}222\Big\}b_n + \Big\{\mathrm{ZM_Z}222\Big\}c_n + \Big\{\mathrm{ZM_L}210 + \mathrm{ZM_L}220 + \mathrm{ZM_L}222\Big\}d_n = -\mathrm{Zinc2} \quad (3.19)$$

Finally, adding the 4^{th} row to the 8^{th} row, we get

$$\Big\{\mathrm{LJ_Z}222\Big\}a_n + \Big\{\mathrm{LJ_L}210 - \mathrm{LJ_L}220 - \mathrm{LJ_L}222\Big\}b_n + \Big\{\mathrm{LM_Z}210 + \mathrm{LM_Z}220 + \mathrm{LM_Z}222\Big\}c_n + \Big\{\mathrm{LM_L}222\Big\}d_n = -\mathrm{Linc2} \quad (3.20)$$

The above four equations, can be written in matrix form as follows.

$$\begin{bmatrix} \mathrm{ZJ_Z}1 & \mathrm{ZJ_L}1 & \mathrm{ZM_Z}1 & \mathrm{ZM_L}1 \\ \mathrm{LJ_Z}1 & \mathrm{LJ_L}1 & \mathrm{LM_Z}1 & \mathrm{LM_L}1 \\ \mathrm{ZJ_Z}2 & \mathrm{ZJ_L}2 & \mathrm{ZM_Z}2 & \mathrm{ZM_L}2 \\ \mathrm{LJ_Z}2 & \mathrm{LJ_L}2 & \mathrm{LM_Z}2 & \mathrm{LM_L}2 \end{bmatrix} \begin{bmatrix} a \\ b \\ c \\ d \end{bmatrix} = \begin{bmatrix} -\mathrm{Zinc1} \\ -\mathrm{Linc1} \\ -\mathrm{Zinc2} \\ -\mathrm{Linc2} \end{bmatrix} \quad (3.21)$$

The square matrix in (3.21) is $4N \times 4N$, and is called the enhanced moment matrix. This matrix is much smaller than $8N \times 8N$ moment matrix in (3.9). However, the elements of the enhanced matrix are more complicated. For example, the element in the m^{th} row and the n^{th} column of $\mathrm{ZJ_Z}1$ in (3.21) is equal to the z-component of the electric field produced on segment m^{th} of S_1. This field consists of three parts. The first part is due to $\mathrm{J_Z}$ on the n^{th} segment of S_1, when this current radiates in the external medium (ϵ_0, μ_0). The second part is due to the image of this $\mathrm{J_Z}$, when this image current radiates in the external medium (ϵ_0, μ_0). Obviously, this image current is equal to the negative of $\mathrm{J_Z}$, and resides on S_2. The third part is due to $\mathrm{J_Z}$ which resides on the m^{th} segment of S_1, when this $\mathrm{J_Z}$ radiates in the unbounded medium $(\epsilon_1, \mu_1, \gamma_1)$.

First, the expansion coefficients are determined using (3.21). Then, the scattered fields can easily be computed. The bi-static radar cross section for

$z-$ and $\phi-$ directed scattered fields is defined as

$$\sigma_z(\phi) = \frac{k_0}{4}\left|\sum_{n=1}^{N} l_{n_1}\Big(a_n - \frac{d_n}{\eta_0}\hat{t}_n^1\cdot\hat{a}_\phi\Big)e^{jk_0\rho^{n_1}cos(\phi-\phi^{n_1})} - \sum_{n=N+1}^{2N} l_{n_2}\Big(a_n + \frac{d_n}{\eta_0}\hat{t}_n^2\cdot\hat{a}_\phi\Big)e^{jk_0\rho^{n_2}cos(\phi-\phi^{n_2})}\right|^2 \quad (3.22)$$

$$\sigma_\phi(\phi) = \frac{k_0}{4}\left|\sum_{n=1}^{N} l_{n_1}\Big(\frac{c_n}{\eta_0} + b_n\hat{t}_n^1\cdot\hat{a}_\phi\Big)e^{jk_0\rho^{n_1}cos(\phi-\phi^{n_1})} + \sum_{n=N+1}^{2N} l_{n_2}\Big(\frac{c_n}{\eta_0} - b_n\hat{t}_n^2\cdot\hat{a}_\phi\Big)e^{jk_0\rho^{n_2}cos(\phi-\phi^{n_2})}\right|^2 \quad (3.23)$$

where, σ denotes the bistatic radar scattering width, l_{n_1} (l_{n_2}) is the length of the n^{th} segment on S_1 (S_2), $\hat{t}_n^1$ ($\hat{t}_n^2$) represents the unit vector tangent to the nth segment (counter-clockwise in the lateral direction) on S_1 (S_2), $\hat{a}_\phi$ is the unit vector in the ϕ-direction at the field point, ρ^{n_1} (ρ^{n_2}) and ϕ^{n_1} (ϕ^{n_2}) are the cylindrical coordinates of the center of the n^{th} segment on S_1 (S_2), η_0 is the free-space wave impedance, and k_0 is the free-space wavenumber.

The numerical results computed using the enhanced moment matrix represented by (3.21) are presented in chapter 4.

Chapter 4

Numerical Results and Discussion

In this chapter, the numerical results obtained from the formulations developed in Chapter 3 are presented. For each method, a MATLAB [84] program is scripted to compute numerical solutions. Using (3.9 and 3.21), first, the expansion coefficients are determined. Then the other quantities of interest such as scattered fields can easily be computed.

To demonstrate the flexibility and robustness of the proposed approaches, cylinders of arbitrary cross-sections such as circular, elliptical, rectangular, and triangular are analyzed. The setup is assumed to be illuminated by either a TM or a TE plane wave. Different studies for various material parameters such as permittivity (ϵ), permeability (μ), electric ($tan\delta_e$) and magnetic ($tan\delta_m$) losses, and chiral admittance (γ) are presented to understand the characteristics of the chiral materials when they are placed in front of a PEC plane. The effect of incident angles (ϕ^i) is also investigated. The surfaces are approximated by thirty segments per wavelength (λ) unless otherwise stated. For all work presented here, the external medium has free space parameters (ϵ_0, μ_0), and the frequency of the incident wave is assumed to be 300 MHz. Computed results include currents on the cylinder and the scattered fields.

4.0.1 Motivation

The scattering behavior of a chiral cylinder above a ground plane can be very different than the scattering behavior in free-space. Because of the presence of a cross-polarized component, the scattered field from a chiral cylinder, even in free-space, is shown to be quite different than the field scattered from a similar dielectric cylinder [38, 44].

To show the effect of the ground plane consider Fig. 4.1 which shows this difference in the bi-static scattering width in the backward region ($0^o < \phi < 180^o$). This problem setup is shown in the inset of Fig. 4.1. The radius of the cylinder is $0.5\lambda_0$. The cylinder is illuminated by a TM plane wave with an angle of incidence of $\phi^i = 90^o$. Figure 4.1 clearly shows how different the scattering behavior can be with the presence of a PEC plane. It is seen that the back-scattered co-polarized field has been increased around 8 dB, and nulls are more pronounced as compared to when this cylinder is placed in free-space. Similarly, the cross-polarized component has been increased around 10 dB, and multiple major lobes are introduced in other directions.

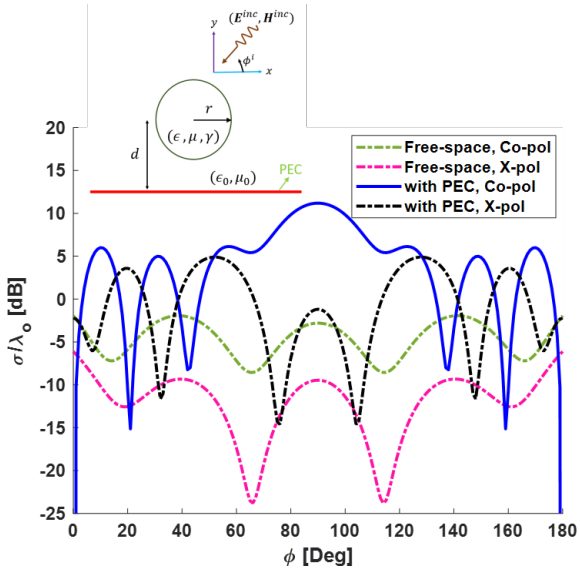

Figure 4.1: Bi-static RCS of a circular chiral cylinder in free-space and when it is placed above a ground plane, TM excitation, $\phi^i = 90^o$, $\epsilon_r = 4, \mu_r = 1, \gamma = 0.002, r = 0.5\lambda_0, d = \lambda_0$.

4.0.2 Verification

The results for a chiral cylinder above a ground plane are computed for the first time in this work. To the best of our knowledge, solution for such a problem does not exist in the literature. Before presenting results for a chiral cylinder above a ground plane, this work is validated in various ways.

First, a circular chiral cylinder in free-space is considered. For this problem, an exact eigenfucntion solution is presented in [44]. The cylinder is characterized by $(\epsilon_r = 1.5, \mu_r = 4, \gamma = 0.0005)$, and is illuminated by a TM plane wave with incidence angle $\phi^i = 180^o$. The radius of the cylinder is $0.1\lambda_0$. Bi-static scattering width is computed and is compared with the exact results as shown in Fig. 4.2. From Fig. 4.2, it is evident that the computed results obtained from this work are in excellent agreement with those obtained from the exact results.

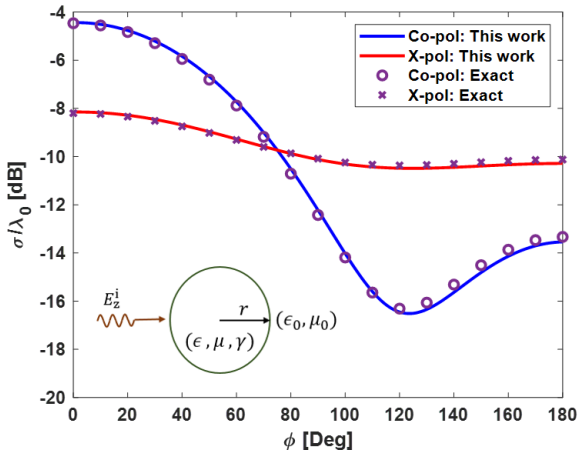

Figure 4.2: Comparison, with the exact solution, of bi-static scattering width of a circular chiral cylinder in free-space.

Now, we added another circular chiral cylinder with parameters of the vacuum (ϵ_0, μ_0). The center to center distance between two cylinders is $d = 0.5\lambda_0$. Then, the results must be the same as those in the previous study. This is achieved as shown in Fig. 4.3.

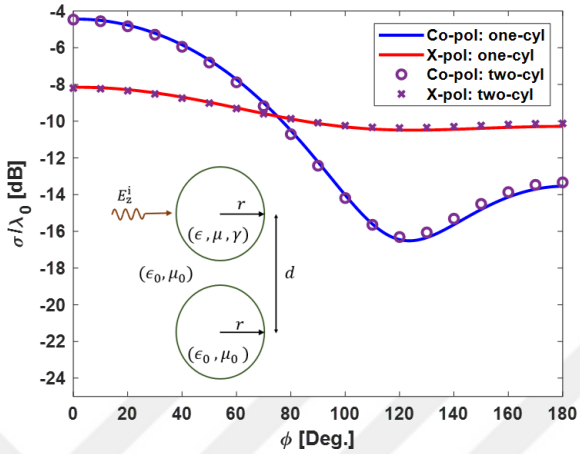

Figure 4.3: Bi-static scattering width of two circular chiral cylinders. One of the cylinders is the same as the one in Fig. 4.2 and the other is a fictitious cylinder with parameters of vacuum.

The results for the problem of scattering from a chiral cylinder above a PEC plane are not available in the literature. Therefore, we used various special cases to validate our computed results. As an example, consider a circular chiral cylinder placed above a PEC plane as shown in Fig. 4.4.

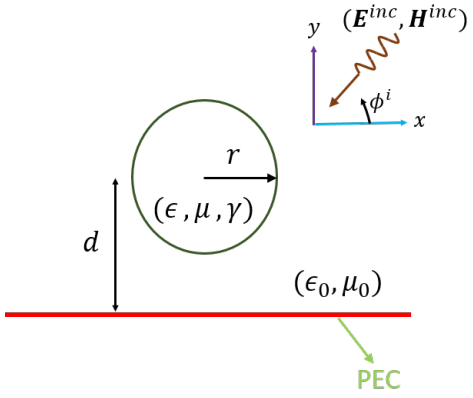

Figure 4.4: A circular chiral cylinder above a PEC plane.

The radius r of the cylinder is $0.1\lambda_0$. The PEC plane is assumed to be at $y = 0$. The distance d between the PEC plane and the center of the cylinder is $0.5\lambda_0$. The

cylinder is characterized by $\epsilon_r = 4, \mu_r = 1.5$, and a variable chiral admittance γ. It is illuminated by a TM plane wave with $\phi^i = 90^o$. Fig. 4.5 and Fig. 4.6 show the co- and cross-polarized components of the bi-static scattering width for various values of γ. It is seen from Fig. 4.5 that as γ reduces to zero, the co-polarized component of the scattering width of the chiral cylinder approaches to that of a regular dielectric cylinder of $\epsilon_r = 4, \mu_r = 1.5$. The results for the dielectric cylinder above a PEC plane is computed using the approach in [89]. Also, from Fig. 4.6 we see that as γ approaches zero, the cross-polarized component of the scattering width vanishes. Based on this example, and various other special cases that we considered, we have confidence in our computed results.

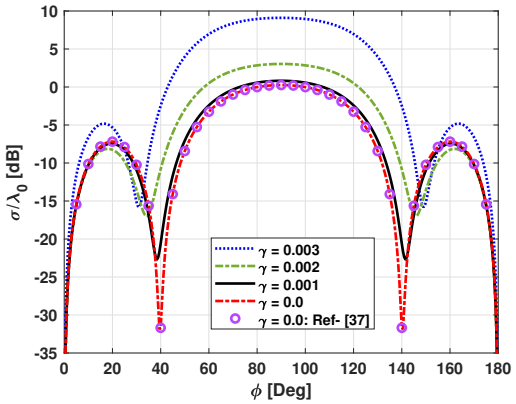

Figure 4.5: Co-polarized component of the bi-static RCS of a circular chiral cylinder placed above a PEC plane. TM excitation, $\phi^i = 90^o$ for various γ values.

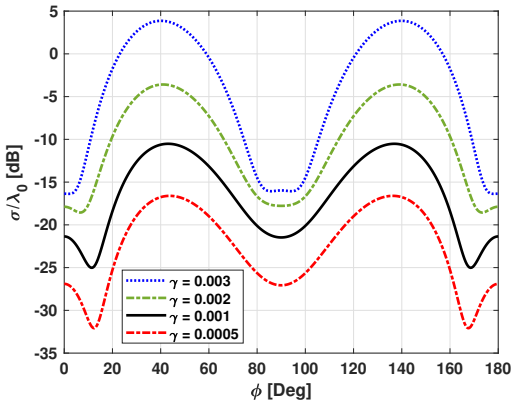

Figure 4.6: Cross-polarized component of the bi-static RCS of a circular chiral cylinder placed above a PEC plane. TM excitation, $\phi^i = 90^o$ for various γ values.

4.0.3 More Computed Results for the Circular Cylinder

A circular chiral cylinder of radius r is placed above a PEC plane. The distance from the center of the cylinder to the PEC plane is denoted by d. The permittivity and permeability of the cylinder are denoted by ϵ and μ, respectively. The chiral admittance is represented by γ, and the system is excited by either a TM or a TE plane wave. This problem is shown in Fig. 4.4.

4.0.3.1 TM-Excitation

In this section, the system shown in Fig. 4.4 is excited by a TM plane wave with an incidence angle (ϕ^i) of 90^o. The radius of the cylinder r is $0.5\lambda_0$, and the distance d from the center of the cylinder to the PEC plane is λ_0. The relative permittivity, ϵ_r, of the cylinder is 4 and the relative permeability, μ_r, is assumed to be 1. The chiral admittance, γ, of the cylinder is 0.002. The computed equivalent electric and magnetic surface currents on the chiral cylinder are shown in Fig. 4.7 and Fig. 4.8, and the scattering width is given in Fig. 4.9. Results obtained by two methods are in excellent agreement.

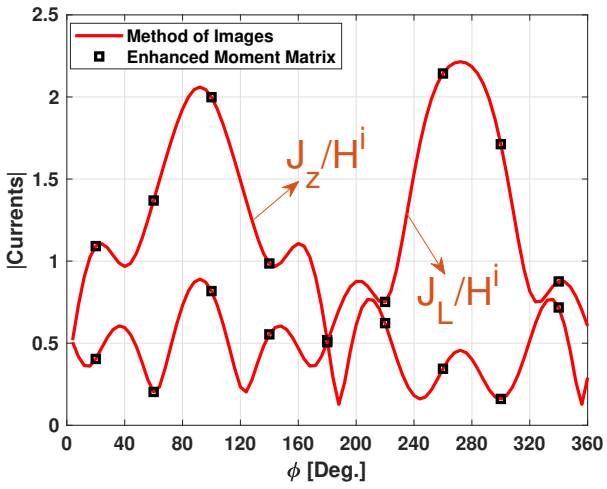

Figure 4.7: The longitudinal and the lateral components of equivalent surface electric current on the circular chiral cylinder, TM excitation, $\phi^i = 90^o$, $r = 0.5\lambda_0$, $d = \lambda_0$, $\epsilon_r = 4$, $\mu_r = 1$, $\gamma = 0.002$.

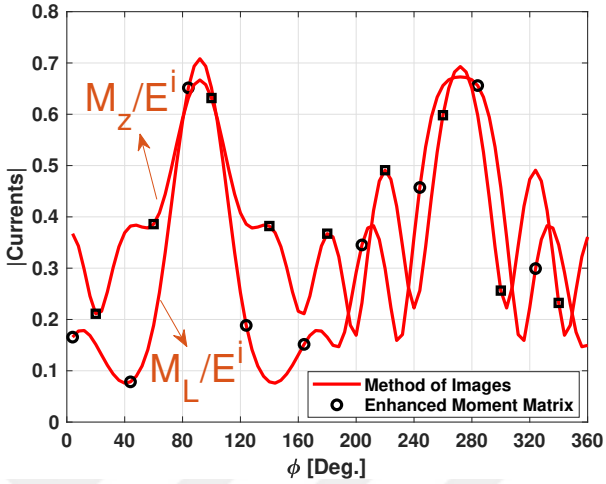

Figure 4.8: The longitudinal and the lateral components of equivalent surface magnetic current on the circular chiral cylinder, TM excitation, $\phi^i = 90^o$, $r = 0.5\lambda_0$, $d = \lambda_0$, $\epsilon_r = 4$, $\mu_r = 1$, $\gamma = 0.002$.

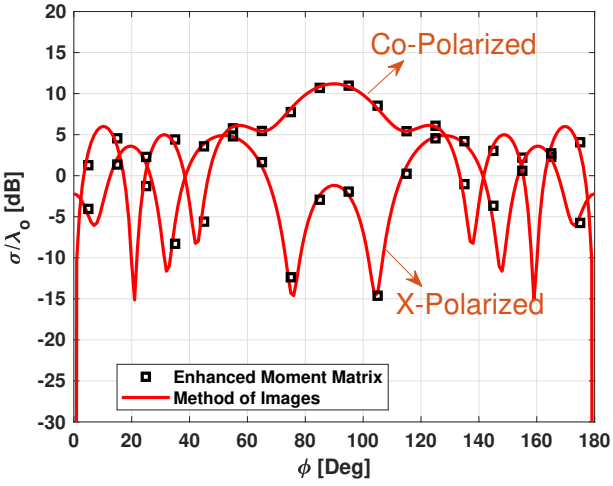

Figure 4.9: Bi-static RCS of a circular chiral cylinder placed above a PEC plane, TM excitation, $\phi^i = 90^o$, $r = 0.5\lambda_0$, $d = \lambda_0$, $\epsilon_r = 4$, $\mu_r = 1$, $\gamma = 0.002$.

Figure 4.10 and Fig 4.11 show the magnitude and the phase of the electric and magnetic fields internal to the circular chiral cylinder placed above a PEC plane, along the $y = \lambda_0$ line.

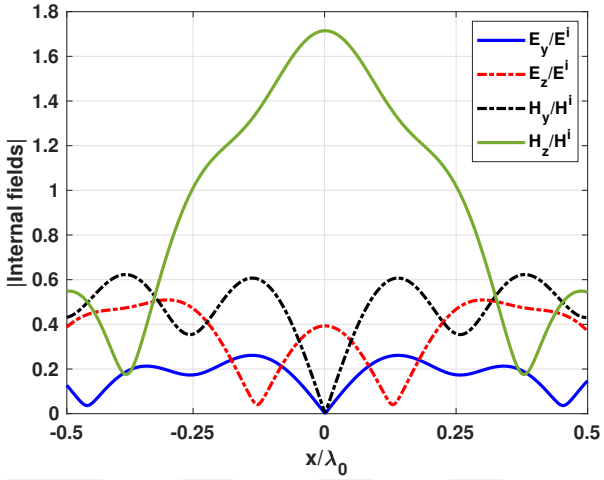

Figure 4.10: The magnitude of the fields internal to the circular chiral cylinder along the $y = \lambda_0$ line for the setup shown in Fig. 4.4, TM excitation, $\phi^i = 90^o$, $r = 0.5\lambda_0$, $d = \lambda_0$, $\epsilon_r = 4$, $\mu_r = 1$, $\gamma = 0.002$.

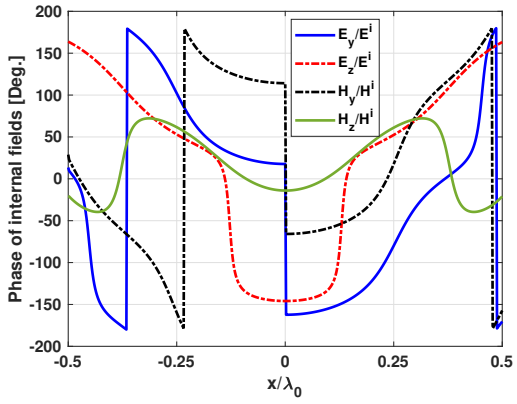

Figure 4.11: The phase of the fields internal to the circular chiral cylinder along the $y = \lambda_0$ line for the setup shown in Fig. 4.4, TM excitation, $\phi^i = 90^o$, $r = 0.5\lambda_0$, $d = \lambda_0$, $\epsilon_r = 4$, $\mu_r = 1$, $\gamma = 0.002$.

Next, the same configuration (shown in Fig. 4.4) is studied for various different incident angles. Figures 4.12 and 4.13, respectively, show the effect of incident angles on the co- and cross-polarized components of the scattering width. The asymmetric behavior is due to the asymmetric excitation. Also, note that, the magnitude of the co-polarized component of the scattered far-field has peak at

emergence angles. For instance, if the incidence angle is 30^o, then the emergence angle will be 150^o.

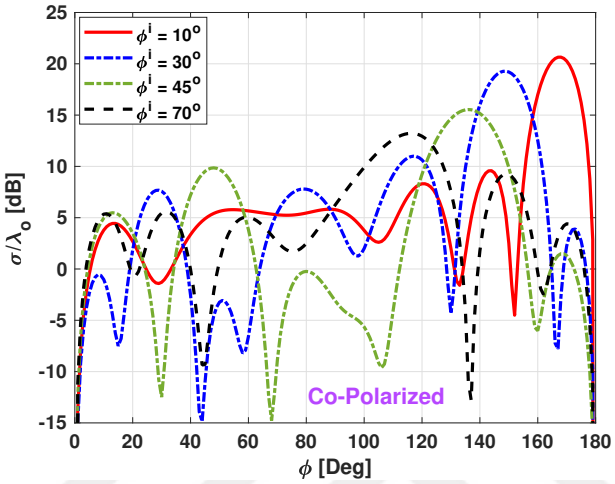

Figure 4.12: Co-polarized component of bi-static RCS for a circular chiral cylinder above a PEC plane with different incident angles, ϕ^i, TM excitation, $r = 0.5\lambda_0$, $d = \lambda_0$, $\epsilon_r = 4$, $\mu_r = 1$, $\gamma = 0.002$.

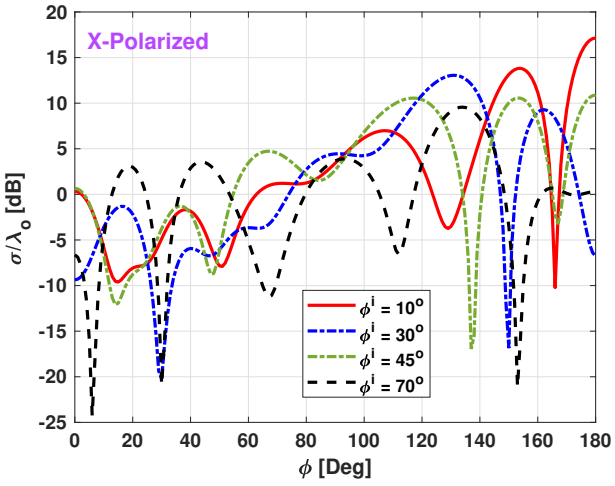

Figure 4.13: Cross-polarized component of bi-static RCS for a circular chiral cylinder above a PEC plane with different incident angles, ϕ^i, TM excitation, $r = 0.5\lambda_0$, $d = \lambda_0$, $\epsilon_r = 4$, $\mu_r = 1$, $\gamma = 0.002$.

Bi-static RCS comparison of circular conducting, dielectric, and chiral

cylinders placed above a PEC plane is shown in Fig 4.14. For these three cases, the same setup shown in Fig. 4.4 is considered. The dielectric cylinder is characterized by $(\epsilon_r = 4, \mu_r = 1)$, and the chiral cylinder is characterized by $(\epsilon_r = 4, \mu_r = 1, \gamma = 0.002)$. The radius of the cylinders is $r = 0.5\lambda_0$, and the distance from the center of the cylinder to the ground plane is $d = \lambda_0$. The system is illuminated by a TM plane wave with $\phi^i = 90^o$. Figure 4.14 shows the bi-static scattering width of a conducting, dielectric, or chiral cylinder placed above a PEC plane. The three cylinders behave entirely different from each other. From Fig. 4.14, it was observed that the magnitude of the side lobes of a conducting cylinder is comparable to the magnitude of the main lobe, and the magnitude of the main lobe of the dielectric cylinder is 5 dB smaller than the side lobes. For chiral cylinder, the magnitude of the co-polarized component of the scattering width has maximum amplitude at $\phi = 90^o$, and deep nulls are also introduced in other directions. For the sake of completeness, cross-polarized component of the scattered far-field is also given, and it is noted that the cross-polar component for the chiral cylinder is comparable with the scattering width of PEC or dielectric at certain angles. Such results make the numerical analysis of chiral materials important because of their complex scattering properties.

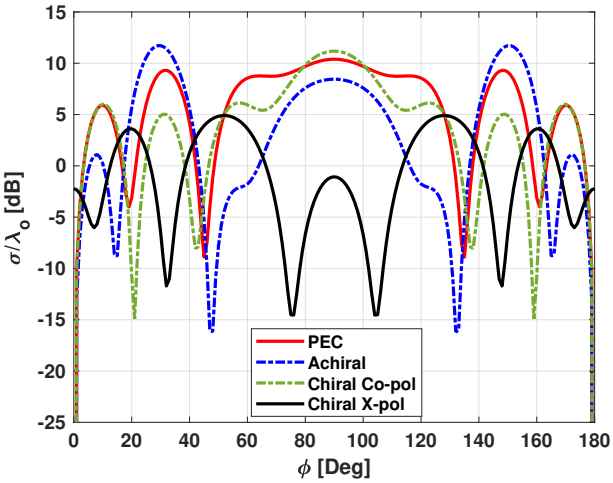

Figure 4.14: Bi-static RCS for circular conducting, dielectric, and chiral cylinders placed above a PEC plane, TM excitation, $\phi^i = 90^o$, $r = 0.5\lambda_0$, $d = \lambda_0$.

4.0.3.2 TE-Excitation

The same system (given in Fig. 4.4) maybe excited by a TE plane wave with $\phi^i = 90^o$. The radius of the cylinder r is $0.5\lambda_0$, while the distance d from the center of the cylinder to PEC plane is λ_0.

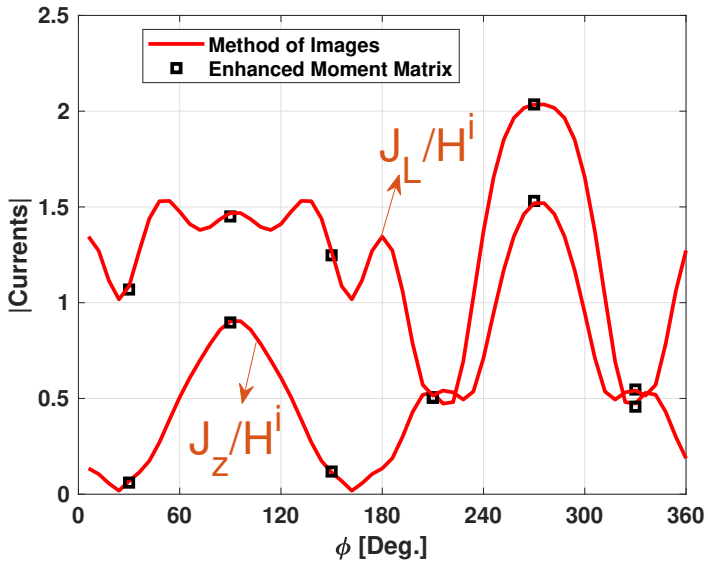

Figure 4.15: The magnitude of the longitudinal and the lateral components of equivalent surface electric current on the circular chiral cylinder, TE excitation, $\phi^i = 90^o$, $r = 0.5\lambda_0$, $d = \lambda_0$, $\epsilon_r = 4$, $\mu_r = 1$, $\gamma = 0.002$.

The relative permittivity, ϵ_r, of the cylinder is 4 and the relative permeability, μ_r, is assumed to be 1. The chiral admittance, γ, of the cylinder is 0.002. The computed equivalent electric and magnetic surface currents on the chiral cylinder are shown in Fig. 4.15 and Fig. 4.16, and the scattering width is given in Fig. 4.17.

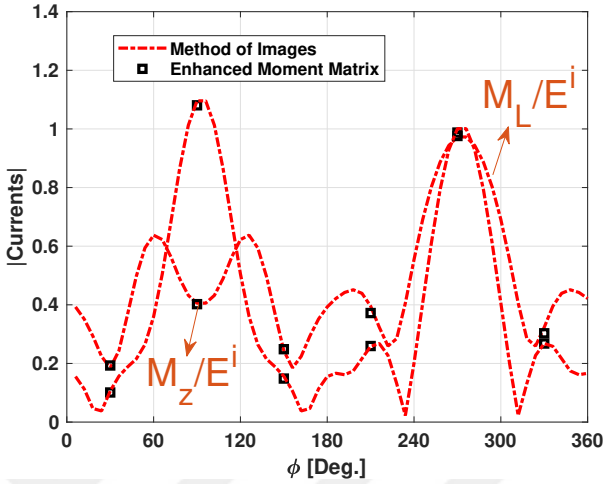

Figure 4.16: The magnitude of the longitudinal and the lateral components of equivalent surface magnetic current on the circular chiral cylinder, TE excitation, $\phi^i = 90^o$, $r = 0.5\lambda_0$, $d = \lambda_0$, $\epsilon_r = 4$, $\mu_r = 1$, $\gamma = 0.002$.

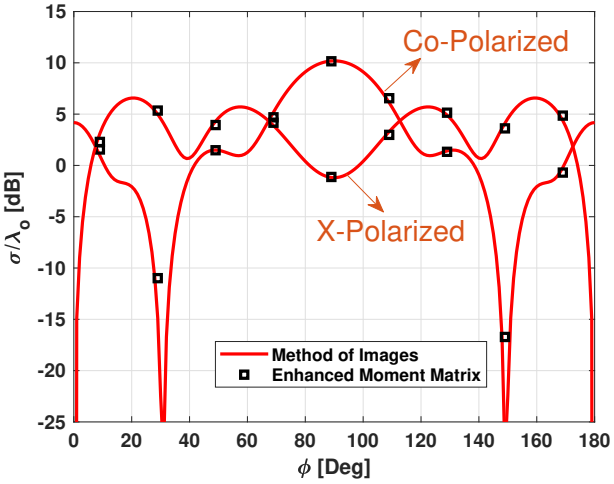

Figure 4.17: Bi-static RCS of a circular chiral cylinder placed above a PEC plane, TM excitation, $\phi^i = 90^o$, $r = 0.5\lambda_0$, $d = \lambda_0$, $\epsilon_r = 4$, $\mu_r = 1$, $\gamma = 0.002$.

Figure 4.18 and Fig 4.19 show the magnitude and the phase of the electric and magnetic fields internal to the circular chiral cylinder placed above a PEC plane, along the $y = \lambda_0$ line.

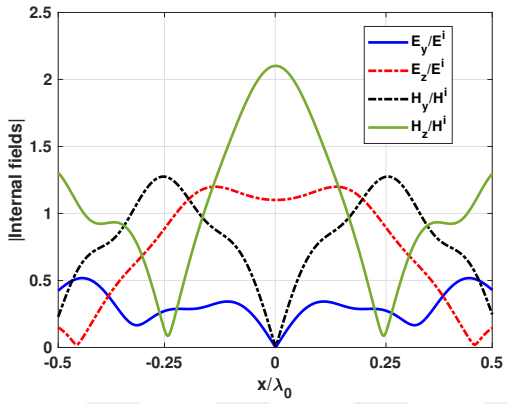

Figure 4.18: The magnitude of the fields internal to the circular chiral cylinder along the $y = \lambda_0$ line for the system shown in Fig. 4.4, TE excitation, $\phi^i = 90^o$, $r = 0.5\lambda_0$, $d = \lambda_0$, $\epsilon_r = 4$, $\mu_r = 1$, $\gamma = 0.002$.

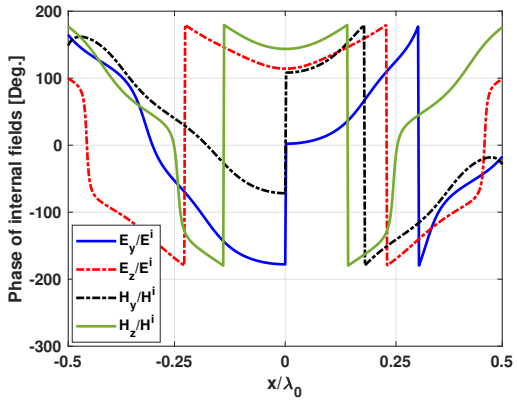

Figure 4.19: The phase of the fields internal to the circular chiral cylinder along the $y = \lambda_0$ line for the system shown in Fig. 4.4, TE excitation, $\phi^i = 90^o$, $r = 0.5\lambda_0$, $d = \lambda_0$, $\epsilon_r = 4$, $\mu_r = 1$, $\gamma = 0.002$.

Next, a study is presented to understand the effect of chirality on the scattering characteristics of a circular chiral cylinder when it is placed above an infinite PEC plane. The same configuration (given in Fig. 4.4) is illuminated by a TE plane wave with $\phi^i = 120^o$. The chiral admittance γ is varied from 0.0 to 0.002 with a step of 0.0005. The co- and cross-polarized component of the scattering width are shown in Fig. 4.20 and Fig. 4.21. Note that, the magnitude of the co-polarized component of the scattering has maximum value at emergence angle (60^o). It was fascinating to see that the cross-polarized component is significantly dropped from

5 dB to -5 dB at 90^o, by an increase of 0.0005 in the chiral admittance and then jumps back to 5 dB with another increase of 0.0005. It is difficult to explain this behavior and the phenomenon in terms of simple theory. However, from this we can conclude that change in chirality effects the bi-static scattering width in a complex manner.

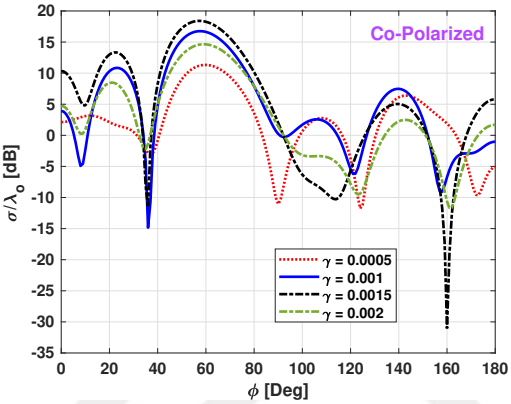

Figure 4.20: The effect of chiral admittance, γ, on the co-polarized component of bi-static RCS for the setup shown in Fig. 4.4, TE excitation, $\phi^i = 120^o$, $r = 0.5\lambda_0$, $d = \lambda_0$, $\epsilon_r = 4$, $\mu_r = 1$.

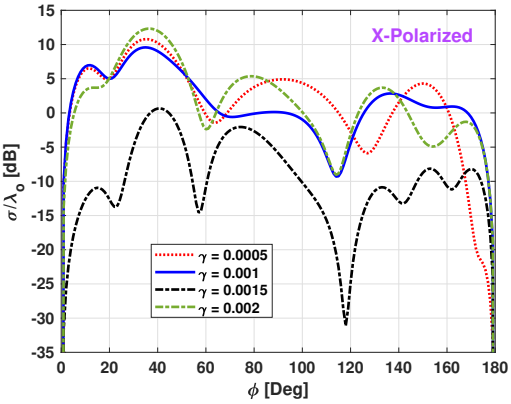

Figure 4.21: The effect of chiral admittance, γ, on the cross-polarized component of bi-static RCS for the setup shown in Fig. 4.4, TE excitation, $\phi^i = 120^o$, $r = 0.5\lambda_0$, $d = \lambda_0$, $\epsilon_r = 4$, $\mu_r = 1$.

Next, circular PEC, dielectric, and chiral cylinders above a ground plane are

studied. The system is illuminated by a TE plane wave with $\phi^i = 90^o$. The dielectric cylinder is characterized by $(\epsilon_r = 4, \mu_r = 1)$, and the chiral cylinder is characterized by $(\epsilon_r = 4, \mu_r = 1, \gamma = 0.002)$. The radius of the cylinders is $r = 0.5\lambda_0$, and the distance from the center of the cylinder to the ground plane is $d = \lambda_0$. Bi-static RCS is given in Fig. 4.22. For a chiral cylinder, it was observed that the magnitude of the co-polarized component of the scattering width has smaller amplitude as compared to the other cylinders (PEC and dielectric), and it also has deep nulls at around 30^o and 150^o. For the sake of completeness, cross-polarized component of the scattered far-field is also given, and it is noted that the cross-polar component for the chiral cylinder is comparable with the scattering width of PEC or dielectric at certain angles.

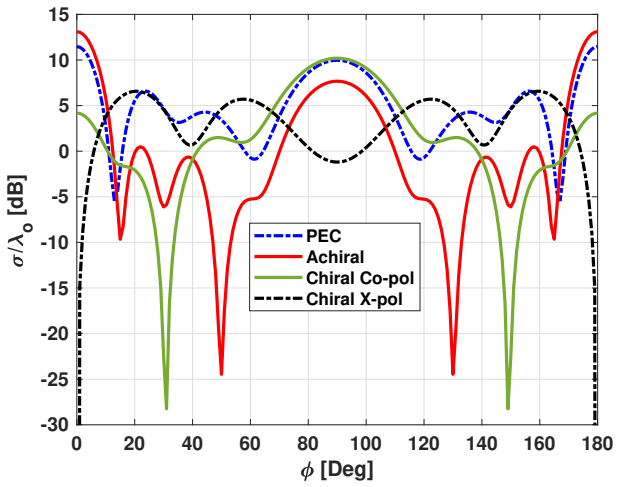

Figure 4.22: Bi-static RCS for circular PEC, dielectric, and chiral cylinders placed above a PEC plane, TE excitation, $\phi^i = 90^o$, $r = 0.5\lambda_0$, $d = \lambda_0$.

4.0.4 The Elliptical Cylinder

In this section, an elliptical cylinder is studied. This problem is shown in Fig. 4.23. The setup is excited by a TM plane wave with $\phi^i = 90^o$. The major radius of the cylinder a is $0.4\lambda_0$, while the minor radius of the cylinder b is $0.5a$.

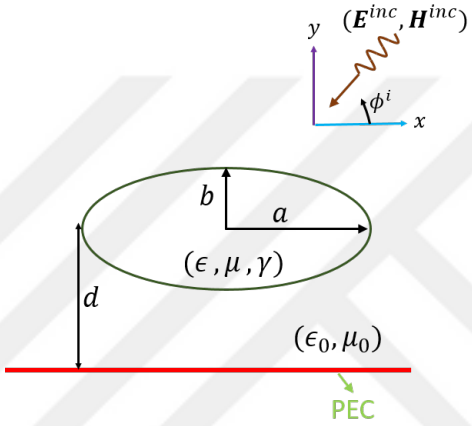

Figure 4.23: An elliptical chiral cylinder above a PEC plane.

The effect of the distance d between the cylinder and the PEC plane is studied. The distance is varied from $0.5\lambda_0$ to $0.8\lambda_0$ with a step of $0.1\lambda_0$. The relative permittivity, ϵ_r, of the cylinder is 3.1 and the relative permeability, μ_r, is assumed to be 1. The chiral admittance, γ, of the cylinder is 0.002. The effect of distance d on the co- and cross-polarized components of the scattering width are shown in Fig. 4.24 and Fig. 4.25, respectively. It is observed that as the cylinder moves away from the half-space, two nulls start to appear in the co-polarized component. In cross-polarized component, two deep nulls can be seen at around 70^o and 110^o by increasing distance d from $0.7\lambda_0$ to $0.8\lambda_0$. However, this behavior may not continue and might be completely different at higher distance values not considered here.

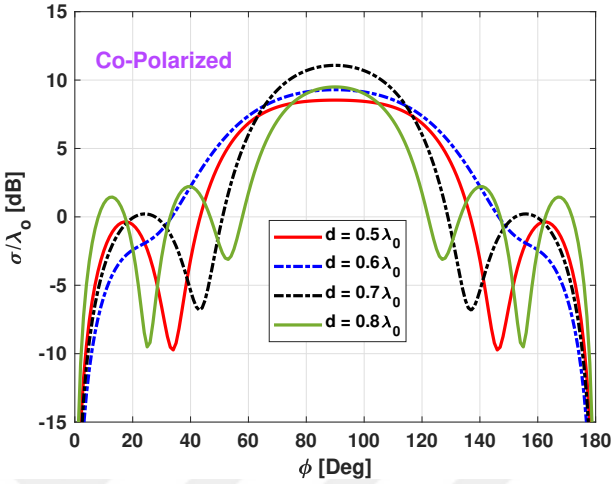

Figure 4.24: The effect of distance d on the co-polarized component of bi-static RCS for the setup shown in Fig. 4.23, TM excitation, $\phi^i = 90^o$, $a = 0.5\lambda_0$, $b = 0.5a$, $\epsilon_r = 3.1$, $\mu_r = 1$, $\gamma = 0.002$.

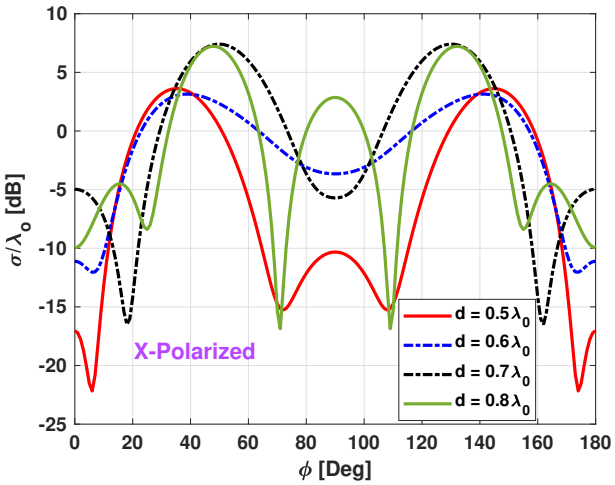

Figure 4.25: The effect of distance d on the cross-polarized component of bi-static RCS for the setup shown in Fig. 4.23, TM excitation, $\phi^i = 90^o$, $a = 0.5\lambda_0$, $b = 0.5a$, $\epsilon_r = 3.1$, $\mu_r = 1$, $\gamma = 0.002$.

Next, the effect of permittivity on the scattering width is studied. The same configuration (given by Fig. 4.23) is considered. The system is excited by a known TE plane wave with $\phi^i = 90^o$. The cylinder is characterized by $\mu_r = 1$ and $\gamma = 0.005$. The major and minor radius of the cylinder are $0.4\lambda_0$ and $0.2\lambda_0$,

respectively. The distance d between the center of the cylinder and the PEC plane is $0.8\lambda_0$. The relative permittivity is varied from 2 to 3.5 with a step of 0.5. The co- and cross-polarized components of bi-static scattering width are shown in Figs. 4.26 and 4.27. Once again, it is observed that it is difficult to explain the behavior by simple theory and the scattered fields vary in a complex manner.

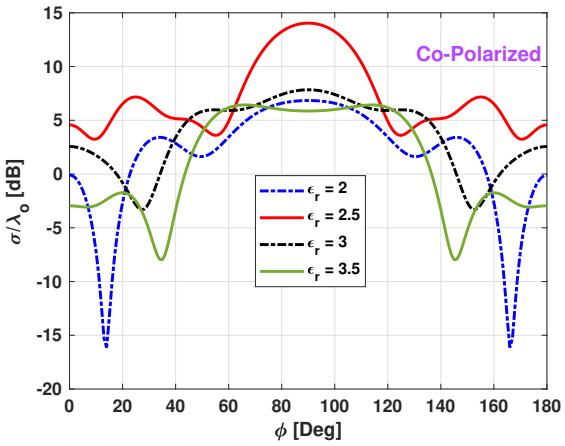

Figure 4.26: The effect of relative permittivity, ϵ_r, of the cylinder on the co-polarized component of bi-static RCS for the setup shown in Fig. 4.23, TE excitation, $\phi^i = 90^o$, $a = 0.4\lambda_0$, $b = 0.5a$, $d = 0.8\lambda_0$, $\mu_r = 1$, $\gamma = 0.005$.

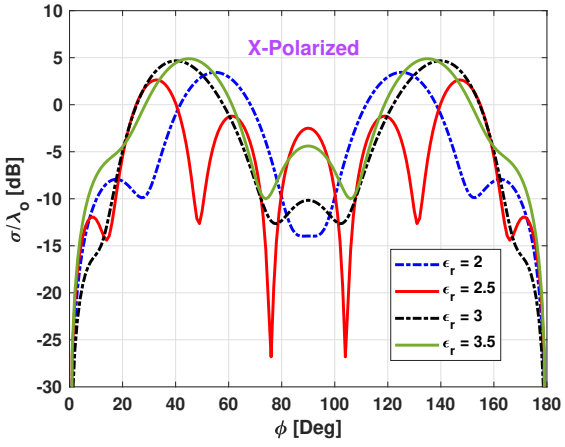

Figure 4.27: The effect of relative permittivity, ϵ_r, of the cylinder on the cross-polarized component of bi-static RCS for the setup shown in Fig. 4.23, TE excitation, $\phi^i = 90^o$, $a = 0.4\lambda_0$, $b = 0.5a$, $d = 0.8\lambda_0$, $\mu_r = 1$, $\gamma = 0.005$.

4.0.5 The Rectangular Cylinder

To demonstrate the flexibility of the proposed work, a chiral cylinder of rectangular cross-section ($L_x \times L_y$) is studied. This problem is illustrated in Fig. 4.28. The setup is excited by a known TM plane wave with $\phi^i = 45^o$. The cross-section of the cylinder is $0.3\lambda_0 \times 0.15\lambda_0$, and is placed at a distance $d = 0.65\lambda_0$ away from the PEC plane. The cylinder is characterized by $\epsilon_r = 2$, and $\gamma = 0.005$. In this section, the effect of relative permeability, μ_r, is studied. The relative permeability is varied from 1 to 2.5 with a step of 0.5.

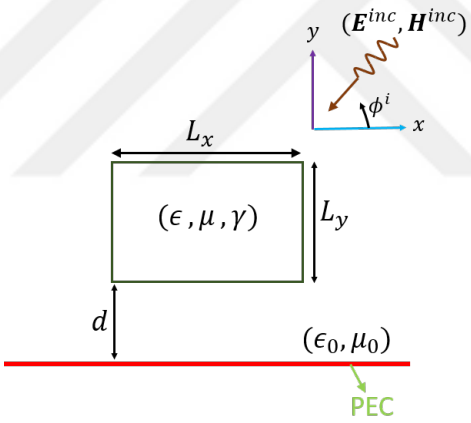

Figure 4.28: A rectangular chiral cylinder above a PEC plane.

Figure 4.29 and Fig. 4.30 show the scattering width for the same problem. In co-polarized component of the scattered field, a null is seen at around 30^o. Note that the cross-polarized component has higher amplitude than the co-polarized component for $\phi = 90^o$.

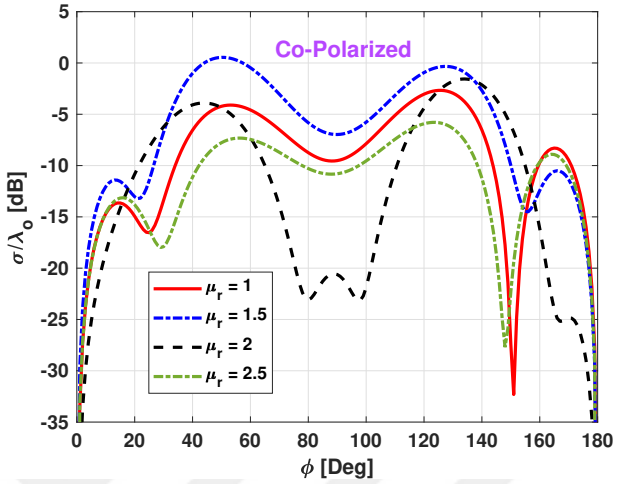

Figure 4.29: The effect of relative permeability, μ_r, on the co-polarized component of bi-static RCS for the setup shown in Fig. 4.28, TM excitation, $\phi^i = 45^o$, $L_x = 0.3\lambda_0$, $L_y = 0.15\lambda_0$, $d = 0.65\lambda_0$, $\epsilon_r = 2$, $\gamma = 0.005$.

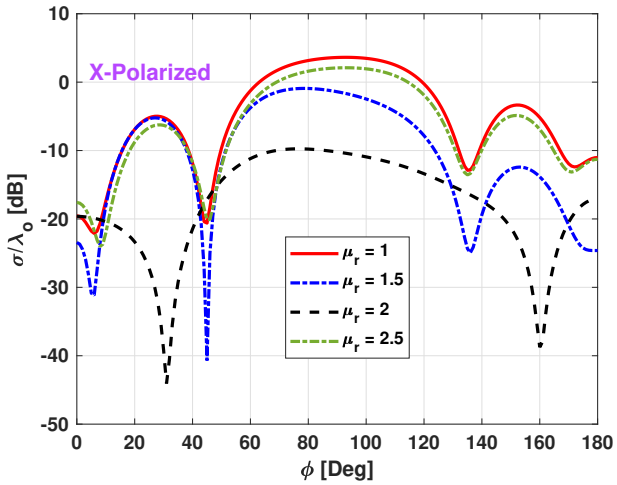

Figure 4.30: The effect of relative permeability, μ_r, on the cross-polarized component of bi-static RCS for the setup shown in Fig. 4.28, TM excitation, $\phi^i = 45^o$, $L_x = 0.3\lambda_0$, $L_y = 0.15\lambda_0$, $d = 0.65\lambda_0$, $\epsilon_r = 2$, $\gamma = 0.005$.

Next, a lossy square was analyzed. The same configuration (given in Fig. 4.28) is considered. The side lengths ($L_x = L_y$) of the square are $0.3\lambda_0$. The cylinder is illuminated by a TE plane wave with $\phi^i = 30^0$. The cylinder is placed at a distance $d = 0.5\lambda_0$ away from the PEC plane. The relative permittivity (ϵ_r) and

the permeability (μ_r) of the cylinder are 3.1 and 1.5, respectively. The chiral admittance, γ, of the cylinder is 0.0005. Both, the electric ($tan\delta_e$) and magnetic ($tan\delta_m$) loss tangents of the cylinder are taken to be 0.05. Figure 4.31 show the co- and cross-polarized components of the scattering width. From Fig. 4.31, it is seen that the co-polarized component has higher magnitude than cross-polarized component, which is expected.

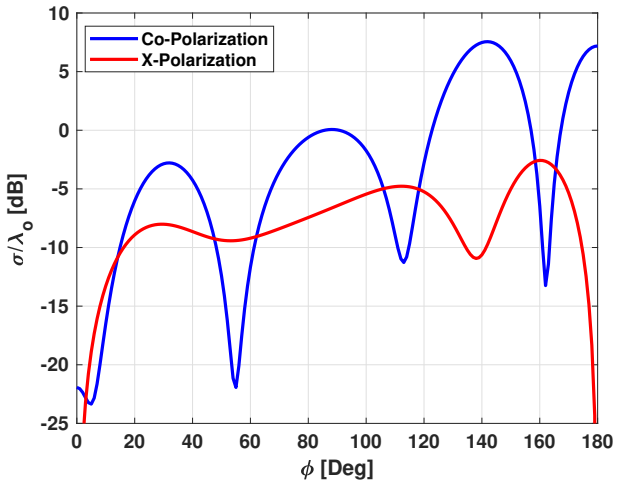

Figure 4.31: Co- and cross-polarized components of bi-static RCS of a lossy square chiral cylinder above a PEC plane, for the setup shown in Fig. 4.28, TE excitation, $\phi^i = 30^o$, $L_x = L_y = 0.3\lambda_0$, $d = 0.5\lambda_0$, $\epsilon_r = 3.1$, $\mu_r = 1.5$ $\gamma = 0.0005$, $tan\delta_e = tan\delta_m = 0.05$.

Figure 4.32 and Fig 4.33 show the magnitude and the phase of the electric and magnetic fields internal to the lossy rectangular chiral cylinder placed above a PEC plane, along the $y = 0.65\lambda_0$ line.

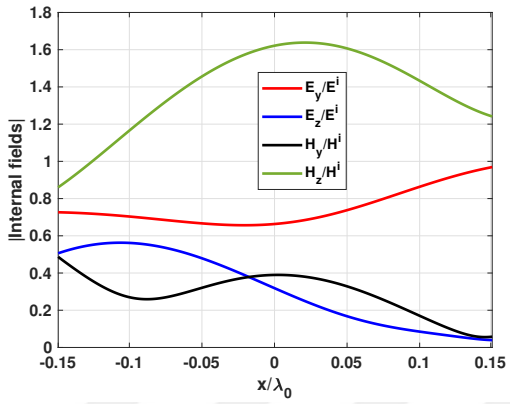

Figure 4.32: The magnitude of the fields internal to the lossy rectangular chiral cylinder along the $y = 0.65\lambda_0$ line, TE excitation, $\phi^i = 30^o$, $L_x = L_y = 0.3\lambda_0$, $d = 0.5\lambda_0$, $\epsilon_r = 3.1$, $\mu_r = 1.5$ $\gamma = 0.0005$, $tan\delta_e = tan\delta_m = 0.05$.

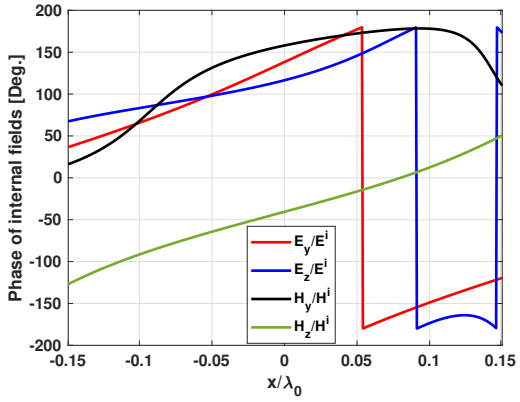

Figure 4.33: The phase of the fields internal to the lossy rectangular chiral cylinder along the $y = 0.65\lambda_0$ line, TE excitation, $\phi^i = 30^o$, $L_x = L_y = 0.3\lambda_0$, $d = 0.5\lambda_0$, $\epsilon_r = 3.1$, $\mu_r = 1.5$ $\gamma = 0.0005$, $tan\delta_e = tan\delta_m = 0.05$.

Next, a lossy chiral cylinder ($\epsilon_r = 2.5, \mu_r = 1, tan\delta_e = tan\delta_m = 0.05$) of rectangular cross-section ($0.2\lambda_0 \times 0.4\lambda_0$) is studied. The cylinder is illuminated by a TE plane wave with $\phi^i = 75^o$. The cylinder is placed close ($d = 0.2\lambda_0$) to the interface. The chiral admittance γ is varied from 0.001 to 0.004 with a step of 0.001. Figure 4.34 and Fig. 4.35 show the co- and cross-polarized components of the bi-static scattering width. It was seen that as the chirality is increased two deep nulls started to appear in the co-polarized component around 30^o and

150^o, while the behavior of the cross-polarized component is difficult to explain by simple theory. In summary, the change in chirality effects the scattering width in a complex manner.

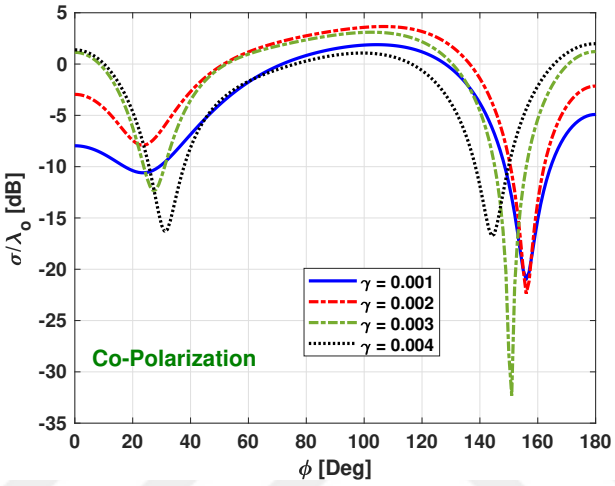

Figure 4.34: The effect of chirality, γ, on the co-polarized component of bi-static RCS for the setup shown in Fig. 4.28, TE excitation, $\phi^i = 75^o$, $L_x = 0.2\lambda_0$, $L_y = 0.4\lambda_0$, $d = 0.2\lambda_0$, $\epsilon_r = 2.5$, $\mu_r = 1$.

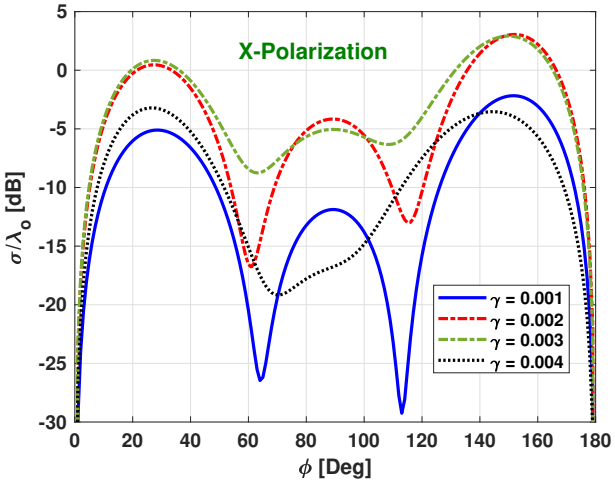

Figure 4.35: The effect of chirality, γ, on the cross-polarized component of bi-static RCS for the setup shown in Fig. 4.28, TE excitation, $\phi^i = 75^o$, $L_x = 0.2\lambda_0$, $L_y = 0.4\lambda_0$, $d = 0.2\lambda_0$, $\epsilon_r = 2.5$, $\mu_r = 1$.

4.0.6 The Triangular Cylinder

Figure 4.36 shows the cross-section of a triangular chiral cylinder. First, an equilateral triangle with height 'b' is illuminated by a TM plane wave with $\phi^i = 60^o$ is analyzed. The height of the triangle is $0.2\lambda_0$ and it is placed at a distance $d = 0.5\lambda_0$ away from the PEC plane. The triangular cylinder has relative permittivity, $\epsilon_r = 3.5$, and relative permeability, $\mu_r = 1$. The chiral admittance is assumed to be $\gamma = 0.0004$. Figure 4.37 show the bi-static scattering width.

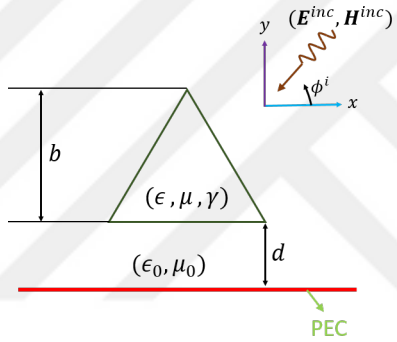

Figure 4.36: A triangular chiral cylinder above a PEC plane.

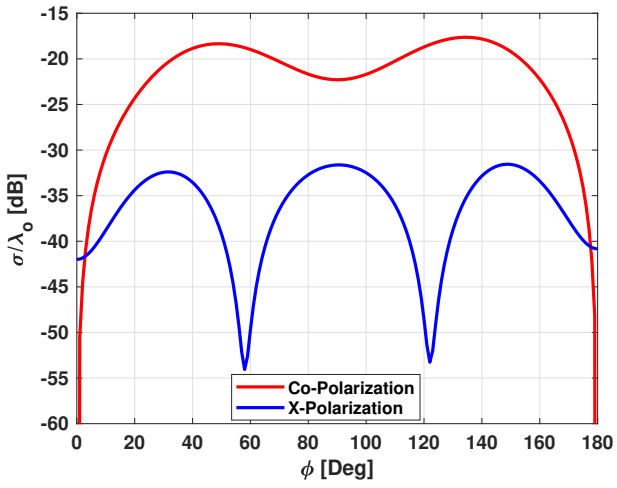

Figure 4.37: Co- and cross-polarized components of bi-static RCS of a triangular chiral cylinder above a PEC plane, for the setup shown in Fig. 4.36, TM excitation, $\phi^i = 60^o$, $b = 0.2\lambda_0$, $d = 0.5\lambda_0$, $\epsilon_r = 3.5$, $\mu_r = 1$ $\gamma = 0.0004$.

Next, a lossy equilateral triangle is studied. The same setup (given in Fig. 4.36) is considered, and maybe excited by a TE plane wave with $\phi^i = 60^o$. The cylinder is characterized by ($\epsilon_r = 3.5, \mu_r = 1$, and $\gamma = 0.0033, tan\delta_e = tan\delta_m = 0.05$). The cylinder is placed $d = 0.5\lambda_0$ away from the PEC plane. The computed results for co- and cross-polarized components of the bi-static scattering width are shown in Fig. 4.38.

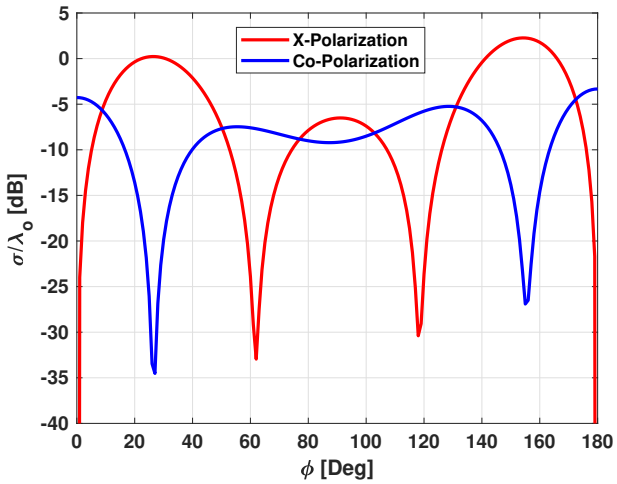

Figure 4.38: Co- and cross-polarized components of bi-static RCS of a triangular chiral cylinder above a PEC plane, for the setup shown in Fig. 4.36, TE excitation, $\phi^i = 60^o$, $b = 0.3\lambda_0$, $d = 0.5\lambda_0$, $\epsilon_r = 3.5$, $\mu_r = 1$, $\gamma = 0.0033$, $tan\delta_e = tan\delta_m = 0.05$.

It is very interesting to see that for this particular study, the cross-polarized component of scattering width has higher magnitude than the co-polarized component, which is unexpected. As a conclusion, one can not explain this unpredictable complex characteristics of chiral materials. In other words, it is a complex problem that can not be understood from simple theory.

4.0.7 Discussion

4.0.7.1 Surface Formulation Versus Volume Formulation

This work is based on the surface equivalence principle. The formulation used in this work is computationally efficient as compared to the volume equivalence principle [38]. In surface formulation, the cross-section of the surface of the body is approximated by linear segments. Then, currents are expanded on these segments. The fields produced by these expansion functions are tested by weighting functions. However, in volume formulation, the cross-sectional area of the body is meshed. This results in more unknowns. For instance, in the surface formulation, the unknowns are $4N$, where N is the number of linear segments. The same problem if solved by volume formulation will have $6M$ unknowns, where M is the number of mesh cells. The volume formulation can be used to solve inhomogeneous cylinders while the surface formulation fails to handle inhomogeneity. In addition, the moment matrix obtained from volume formulation is less complex than the one obtained from the surface formulation. It is due to fact that the volume formulation uses simple free-space Green's function. In summary, the surface formulation presented here is computationally efficient as compared to volume formulation, however, it can not be used when the scatterer is inhomogeneous.

4.0.7.2 Specular Optical Activity of Chiral Materials

Since its conception, chiral materials have been a topic of keen interest for many researchers. Due to optical activity in these materials, the plane of a linearly polarized light ray is rotated. Therefore, specular optical activity appears at interfaces. This specular phenomenon can be very strong for surface such as ground plane, and usually observed for oblique incidence. This is due to the fact that the reflected waves with a different handedness may have different reflectivity levels. To demonstrate this, a circular chiral cylinder of radius $r = 0.5331\lambda_0$ placed at a height $d = 0.05\lambda_0$ above a ground plane similar to the one in Fig.

4.4 is considered. The cylinder is characterized by $(\epsilon_r = 2.1316, \mu_r = 1, \gamma)$. The setup is illuminated by a TM plane wave with $\phi^i = 120^o$. Figure 4.39 shows the scattered normalized far-field pattern above the ground plane for various values of the chiral admittance γ. Note that setting $\gamma = 0$ changes the chiral material into regular dielctric in which case the cross-polarized component is zero. As the chirality decreases, the scattered fields of the chiral cylinder approach those of a regular dielectric. Furthermore, it is interesting to see that the specular angle for the cross-polar field is in a different direction which is due to chirality. Finally, note that the scattered field for the highest chirality is the lowest which shows that chiral materials can be used as EM absorbers. However, both these observations may not hold true for scatterers with different parameters. Such results make the numerical analysis of chiral materials important because their scattering properties vary in a complex manner.

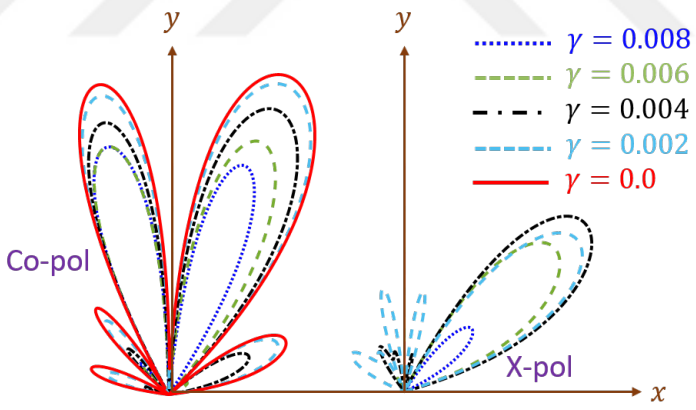

Figure 4.39: Far-field amplitude of a chiral cylinder placed above a ground plane. TM excitation at $\phi^i = 120^o$ for different γ values.

4.0.7.3 Non-Uniqueness of the EFIE Formulation

It is known that the EFIE formulation used here fails to give a unique solution when a cylinder is of a spurious "resonant size" [90]. In such cases the moment matrix is highly ill-conditioned and the results computed using such matrices may not be accurate. Therefore, to tell whether the computed results are accurate or

not, the condition number of the moment matrix must be monitored.

To demonstrate the behavior of the condition number, consider Fig. 4.40 below, where a rectangular cylinder ($0.3\lambda_0 \times 0.15\lambda_0$) is placed at a distance of $0.65\lambda_0$ above a PEC plane.

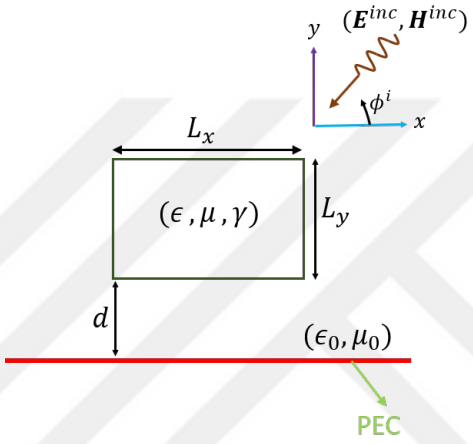

Figure 4.40: A rectangular chiral cylinder above a ground plane.

First, assume that this cylinder to be free-space (i.e. we let $\epsilon = \epsilon_0, \mu = \mu_0$, and $\gamma = 0$) and it is excited by a TM plane wave with incidence angle $\phi^i = 90^o$. Then, we know the exact values of the equivalent surface currents on the cylinder ($\mathbf{J} = \hat{n} \times \mathbf{H}$, and $\mathbf{M} = \mathbf{E} \times \hat{n}$, where $\hat{n}$ is the unit vector normal to the surface of the cylinder and $\mathbf{E}$ and $\mathbf{H}$ are the total fields at the surface of the cylinder). Figure 4.41 shows the variation of the condition number of the moment matrix with $k_0 L_x$. Note that, when $k_0 L_x = 3.1762$, the moment matrix is highly ill-conditioned.

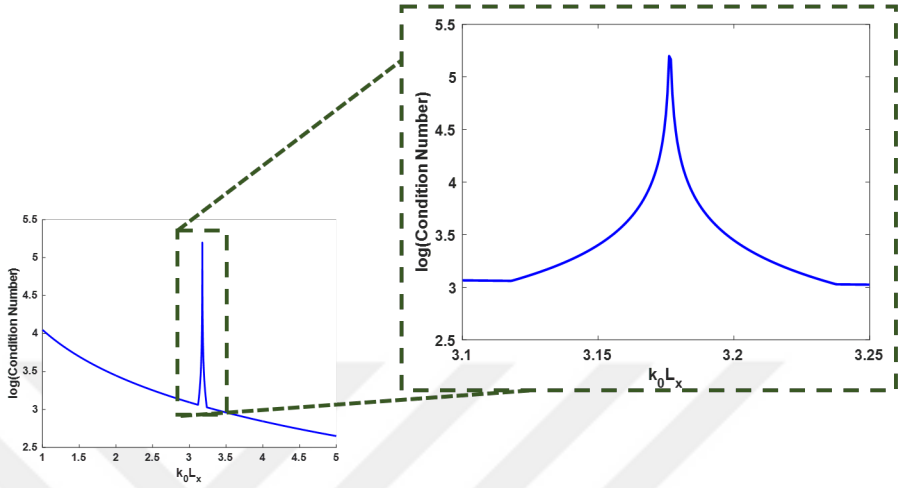

Figure 4.41: Variation of the condition number of the moment matrix with k_0L_x, for a dielectric cylinder above a ground plane.

Figure 4.43 shows the computed surface currents when the matrix is ill-conditioned (log(Condition Number) = 5.19802). It is clearly seen that the computed results do not agree with the exact results. Figure 4.42 shows the computed currents when the matrix is well-conditioned (log(Condition Number) = 3.51502). It is seen that the computed results are in excellent agreement with the exact ones.

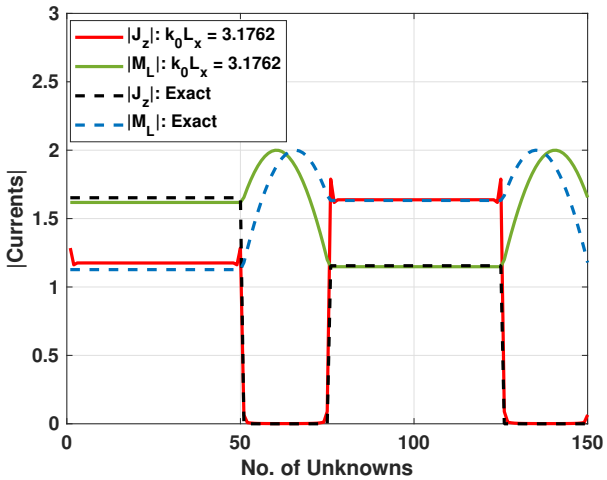

Figure 4.42: Comparison of the exact solution with those computed with an ill-conditioned matrix, TM excitation, $\phi^i = 90^o$, $\epsilon_r = 1, \mu_r = 1, \gamma = 0$.

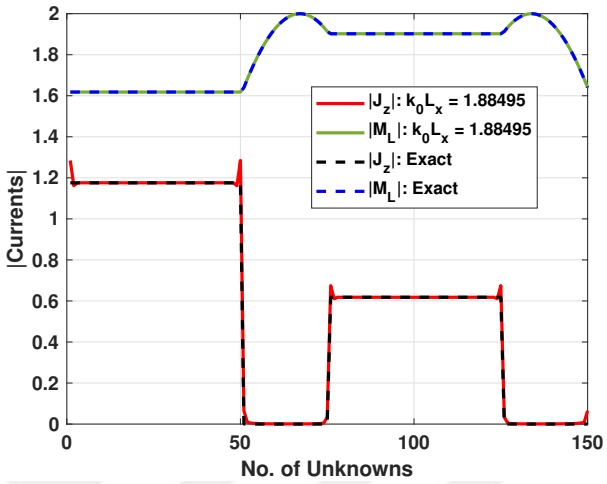

Figure 4.43: Comparison of the exact solution with those computed with a well-conditioned matrix, TM excitation, $\phi^i = 90^o$, $\epsilon_r = 1, \mu_r = 1, \gamma = 0$.

Next, let us assume that the rectangular cylinder shown in Fig. 4.40 is above a PEC plane with the parameters $\epsilon_r = 4$, $\mu_r = 2$, and $\gamma = 0.0005$, and is illuminated by a TM plane wave with incidence angle $\phi^i = 60^o$. The exact results for this problem are unknown. However, when the condition number is large we are sure that our results would be questionable. We can demonstrate that as follows. Figure 4.44 shows the condition number of the moment matrix versus frequency.

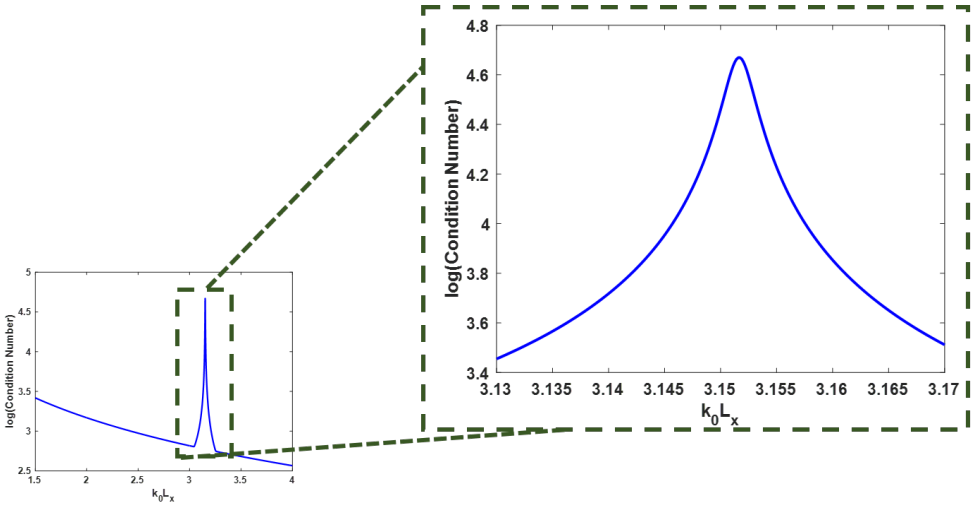

Figure 4.44: Variation of the condition number of the moment matrix with $k_0 L_x$, for a chiral cylinder above a ground plane.

Figure 4.45 shows the equivalent surface currents for three very similar cylinders ($k_0 L_x$ = 3.15164, 3.15165, and 3.15166), when the condition number of the moment matrix is large (log(Condition Number) = 4.6695). It is seen that the computed results for the surface currents are quite different although the cylinders are almost identical. This is not acceptable. This demonstrates the fact mentioned above: the results obtained with an ill-conditioned matrix may not be trusted.

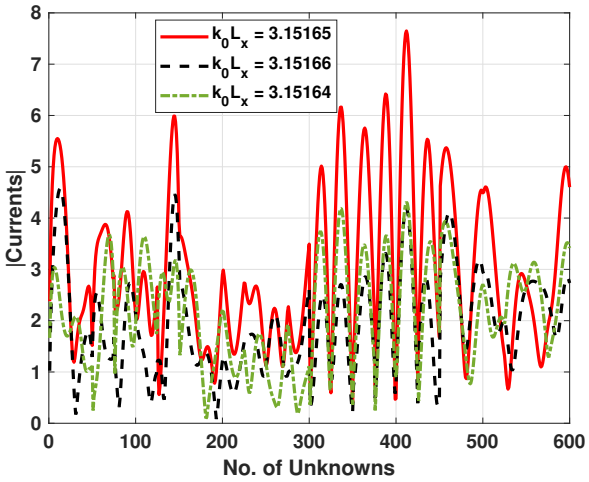

Figure 4.45: Computed surface currents on the cylinder for three different values of $k_0 L_x$, when the condition number of the moment matrix is large, TM excitation, $\phi^i = 60^o$, $\epsilon_r = 4, \mu_r = 2, \gamma = 0.0005$.

On the other hand, Fig. 4.46 shows the surface currents on cylinders of again very similar sizes ($k_0 L_x$ = 1.88494, 1.88495, and 1.88496), when the condition number of the moment matrix is small (log(Condition Number) = 3.22025). It is seen that the currents are indistinguishable. This is expected because the sizes of the three cylinders are basically indistinguishable.

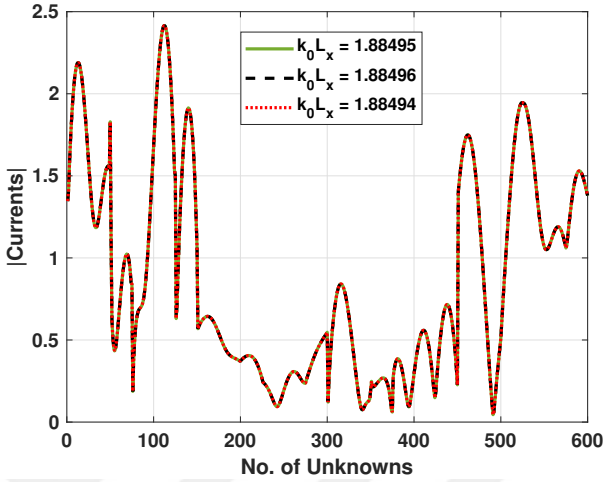

Figure 4.46: Computed surface currents on the cylinder for three different values of $k_0 L_x$, when the condition number of the moment matrix is small, TM excitation, $\phi^i = 60^o$, $\epsilon_r = 4, \mu_r = 2, \gamma = 0.0005$.

In summary, it is well known that the results obtained with an ill-conditioned matrix is questionable. Therefore, we did not present any results for such cases. Also, for the cases considered, no abnormality was observed in the value of the condition number. Therefore, we are confident that these results are accurate.

Chapter 5

Conclusion

A simple moment solution is presented to compute the electromagnetic fields scattered from a chiral cylinder of arbitrary cross-section above a PEC plane. The image theory is used to replace the PEC plane with an image chiral cylinder and an image source. Then, the method of moments is used to formulate the solution to this two-body problem. It was shown that when the image body is legitimate, the two-body problem can be reduced to a one-body problem with a more complicated moment matrix. It was also observed that the computed results for the $\gamma = 0$ case were in excellent agreement with the results obtained by other researchers for the case of a dielectric cylinder.

Before solving the numerical problem of cylinders of arbitrary cross-sections above a PEC plane, three canonical problems are solved exactly using analytical techniques. The purpose here was to verify that the chirality of the image of a chiral cylinder is negative of the chirality of the actual cylinder.

The condition number of the moment matrix was monitored to ensure the accuracy of the computed results. Also, some advantages and drawbacks for the proposed formulation and their solutions are briefly discussed.

Bibliography

[1] D. F. Arago, "Sur une modification remarquable qu'eprouvent les rayons lumineux dans leur passage a travers certains corps diaphanes, et sur quelques autres nouveaux phenomenes d'optique," *Mem. Inst.*, vol. 1, pp. 93–134, 1811.

[2] J. B. Biot, "Memoire sur un nouveau genre d'oscillations que les molecules de la lumiere eprouvent, en traversant certains cristaux," *Mem. Inst.*, vol. 1, pp. 1–372, 1812.

[3] J. B. Biot, "Phenomenes de polarisation successive, observes dans des fluides homogenes," *Bull. Soc. Philomat*, pp. 190–192, 1815.

[4] J. B. Biot, "Memoire sur les rotations que certaines substances impriment aux axes de polarisation des rayons lumineux," *Memoires de I'Academie Royale des Sciences de I'Institut de France*, vol. 2, pp. 41–136, 1817.

[5] J. B. Biot, "Mnoire sur la polarisation circulaire et sur ses applications a la chimie organique," *Memoires de I'Academie Royale des Sciences de I'Institut de France*, vol. 13, pp. 39–175, 1835.

[6] L. Pasteur, "Sur les relations qui peuvent exister entre la forme cristalline, la composition chimique et le sens de la polarisation rotatoire," *Ann. Chim. Phys.*, vol. 24, pp. 442–459, 1848.

[7] K. F. Lindman, "Ober eine durch ein isotropes system von spiralftrmigen resonatoren erzeugte rotationspolarisation der elektromagnetischen wellen," *Annalen der Physik*, vol. 63, no. 23, pp. 621–644, 1920.

[8] K. F. Lindman, "Ober die durch ein actives raumgitter erzeugte rotationspolarisation der elektromagnetischen wellen," *Annalen der Physik*, vol. 69, no. 20, pp. 270–284, 1922.

[9] I. V. Lindell, A. H. Sihvola, and J. Kurkijarvi, "Karl F. Lindman: The last Hertzian, and a harbinger of electromagnetic chirality," *IEEE Antennas and Propagation Magazine*, vol. 34, no. 3, pp. 24–30, 1992.

[10] W. H. Winkler, "An experimental investigation of some models for optical activity," *Journal of Phyical Chemistry*, vol. 60, pp. 1656–1659, 1956.

[11] I. T. Jr. and M. Freeman, "The optical activity of oriented copper helices. I. Experimental," *Journal of Phyical Chemistry*, vol. 61, pp. 1196–1200, 1957.

[12] P. Drude, "Lehrbuch der optik," *Leipzig, S. Hirzel*, p. 371, 1900.

[13] D. L. Jaggard, A. R. Mickelson, and C. H. Papas, "On electromagnetic waves in chiral media," *Appl. Phys.*, vol. 18, pp. 211–216, 1979.

[14] N. Engheta and A. R. Mickelson, "Transition Radiation caused by a Chiral Plate," *IEEE Antennas and Propagation Magazine*, vol. 30, pp. 1213–1216, 1982.

[15] M. P. Silverman, "Reflection and Refraction at the Surface of a Chiral Medium: Comparison of Gyrotropic Constitutive Relations invariant or noninvariant under a duality transformation," *Journal of Opt. Soc. Am. A*, vol. 3, pp. 830–837, 1986.

[16] A. Lakhtakia, V. V. Varadan, and V. K. Varadan, "A Parametric Study of Microwave Reflection Characteristics of a Planar Achiral-Chiral Interface," *IEEE Trans. Electromagn. Compat.*, vol. 28, pp. 90–95, 1986.

[17] A. Lakhtakia, V. K. Varadan, and V. V. Varadan, "Excitation of a Planar achiral/chiral interface by near fields," *Journal Wave-Matter Interact.*, vol. 3, pp. 231–241, 1988.

[18] A. Lakhtakia, V. K. Varadan, and V. V. Varadan, "Reflection of Elastic Plane Waves at a Planar Achiral-Chiral Interface and Through a Chiral Slab,," *Journal Opt. Soc. Am. A*, vol. 87, pp. 2314–2318, 1990.

[19] A. Lakhtakia, V. K. Varadan, and V. V. Varadan, "Reflection of Plane Waves at a Planar Achiral-Chiral Interfaces: Independence of the Reflected Polarization State from the Incident Polarization State," *Journal Opt. Soc. Am. A*, vol. 7, pp. 1654–1656, 1990.

[20] A. Lakhtakia, V. V. Varadan, and V. K. Varadan, "What Happens to Plane Waves at the Planar Interfaces of Mirror-Conjugated Chiral Media," *Journal Opt. Soc. Am. A*, vol. 7, pp. 683–692, 1989.

[21] A. Lakhtakia, "On Extending the brewster law at Planar Interfaces," *Optik*, vol. 84, no. 5, pp. 160–162, 1990.

[22] N. Engheta and S. Bassiri, "Cerenkov Radiation in Chiral Media," *J. Appl. Phys.*, vol. 68, pp. 4393–4398, 1990.

[23] S. Bassiri, C. H. Papas, and N. Engheta, "Electromagnetic Wave Propagation Through a Dielectric-Chiral interface and Through a Chiral Slab," *J. Opt. Soc. Am.A*, vol. 5, pp. 1450–1459, 1988.

[24] A. J. Viitanen, I. V. Lindell, A. H. Sihvola, and S. A. Tretyakov, "Eigen solutions for the Reflection Problem of the Interface of Two Chiral Half-Spaces," *J. Opt. Soc. Am.A*, vol. 7, pp. 683–692, 1990.

[25] A. Lakhtakia, V. V. Varadan, and V. K. Varadan, "Scattering by periodic Achiral-Chiral interfaces," *Journal Opt. Soc. Am. A*, vol. 6, pp. 1657–1681, 1989.

[26] T. Guire, V. V. Varadan, and V. K. Varadan, "Influence of Chirality on the Reflection of EM waves by Planar Dielectric Slabs," *IEEE Trans. Electromagn. Compat.*, vol. 32, pp. 300–303, 1990.

[27] C. F. Bohren, "Light Scattering by an Optically Active Sphere," *Chem. Phys. Lett.*, vol. 29, pp. 458–462, 1974.

[28] C. F. Bohren, "Scattering of Electromagnetic Waves by an Optically Active spherical shell," *Chem. Phys. Lett.*, vol. 62, pp. 1566–1571, 1975.

[29] C. F. Bohren, "Scattering of Electromagnetic Waves by an Optically Active cylinder," *J. Colloid Interface Sci.*, vol. 66, pp. 105–109, 1978.

[30] V. K. Varadan, V. V. Varadan, and A. Lakhtakia, "On the Possibility of Designing Anti-Reflection Coating Using Chiral Composites," *Journal Wave-Matter Interact.*, vol. 2, pp. 71–81, 1987.

[31] A. Lakhtakia, V. K. Varadan, and V. V. Varadan, "Scattering and absorption characteristics of lossy dielectric, chiral, nonspherical objects," *Appl. Opt*, vol. 24, no. 23, pp. 4146–4154, 1985.

[32] E. J. Post, "Formal Structure o f Electromagnetics," *Amsterdam*, 1962.

[33] V. K. Varadan, A. Lakhtakia, and V. V. Varadan, "Scattering by beaded helices: anisotropy and chirality," *J. Wave-Material Interaction*, vol. 2, pp. 153–160, 1987.

[34] V. K. Varadan, A. Lakhtakia, and V. V. Varadan, "Equivalent dipole moments of helical arrangements of small, isotropic, point-polarizable scatters: Application to chiral polymer design," *J. Appl. Phys.*, vol. 63, no. 2, pp. 280–284, 1988.

[35] V. K. Varadan, Y. Ma, and V. V. Varadan, "Effects of chiral microstructure on em wave propagation in discrete random media," *Radio Sci.*, vol. 24, no. 6, pp. 785–792, 1989.

[36] E. O. Kamenetskii, "On the technology of making chiral and bianisotropic waveguides for microwave propagation," *Microwave Opt. Technol. Lett.*, vol. 11, no. 2, pp. 103–107, 1996.

[37] E. O. Kamenetskii, "Magnetostatically controlled bianisotropic media: A novel class of artificial magneto-electric materials," *Advances in complex electromagnetic materials*, pp. 359–376, 1997.

[38] M. S. Kluskens and E. H. Newman, "Scatterig by a Chiral Cylinder of Arbitrary Cross-Section," *IEEE Transactions on Antenna. and Propagation*, vol. 38, pp. 1448–1455, 1990.

[39] M. S. Kluskens and E. H. Newman, "Scattering by a multilayer chiral cylinder," *IEEE Trans. Antennas Propagat.*, vol. 39, pp. 91–96, 1991.

[40] S. Bassiri, N. Engheta, and C. H. Papas, "Dyadic Green's Function and Dipole Radiation in Chiral Media," *Alta Freq.*, vol. 5, pp. 83–88, 1986.

[41] N. Engheta and S. Bassiri, "One- and Two-Dimensional Dyadic Green's Functions in Chiral Media," *IEEE Trans. Antennas Propagat.*, vol. 37, pp. 512–515, 1989.

[42] D. L. Jaggard, X. Sun, and N. Engheta, "Canonical Sources and Duality in Chiral Media," *IEEE Trans. Antennas Propagat.*, vol. 36, pp. 1007–1013, 1988.

[43] H. Cory, "Chiral devices - An overview of canonical problems," *J. Electromagnet. Wave Applicat.*, vol. 9, no. 5, pp. 805–829, 1995.

[44] M. A. Alkanhal, "Electromagnetic Scattering from an Chiral Cylinders of Arbitrary Cross-Section," *PhD Dissertation, Syracuse University*, 1994.

[45] T. Buber, E. Arvas, and M. Al-Kanhal, "Scattering from a Chiral-Coated Metal Cylinder of Arbitrary Cross Section," *Electromagnetics*, vol. 19, pp. 363–371, 1999.

[46] D. Worasawate, "Electromagnetic Scattering from an Arbitrarily Shaped Three Dimensional Chiral Body," *PhD Dissertation, Syracuse University*, 2002.

[47] M. Yuceer, "Electromagnetic Scattering from an Arbitrary Shaped Chiral Body of Revolution," *PhD Dissertation, Syracuse University*, 2004.

[48] P. J. Valle, F. Gonz'alez, and F. Moreno, "Electromagnetic wave scattering from conducting cylindrical structures on flat substrates: study by means of the extinction theorem," *Appl. Opt.*, vol. 33, pp. 512–523, 1994.

[49] A. Madrazo and M. Nieto-Vesperinas, "Scattering of electromagnetic waves from a cylinder in front of a conducting plane," *J. Opt. Soc. Am. A*, vol. 12, pp. 1298–1309, 1995.

[50] P. G. Cottis and J. D. Kanellopoulos, "Scattering from a conducting cylinder above a lossy medium," *Int. J. Electron.*, vol. 65, pp. 1031–1038, 1988.

[51] M. A. Taubenblatt, "Light scattering from cylindrical structures on surfaces," *Opt. Lett.*, vol. 15, pp. 255–257, 1990.

[52] E.Arvas, R. Harrington, and J. Mautz, "Radiation and Scattering from Electrically Small Conducting Bodies of Arbitrary Shape Above an Infinite Ground Plane," *IEEE Trans.*, vol. 35, pp. 378–383, 1987.

[53] O. R. B. Alavikia, "Electromagnetic Scattering from Cylindrical Objects above a Conductive Surface using a Hybrid Finite-element surface Integral Equation Method," *J. Opt. Soc. Am. A.*, vol. 28, pp. 2510–2518, 2011.

[54] F. R. J. Chao, I. Elshafiey, Y. L. Upda, and P. Martin, "General Formulation for Light Scattering by a Dielectric Body Near a Perfectly Conducting Surface," *J. Opt. Soc. Am. A.*, vol. 13, pp. 338–344, 1996.

[55] X. B. Xu, C. M. Butler, G. Videen, , and D. Ngo, "Light Scattering From a Cylinder Near a Plane Interface: Theory and Comparison with Experimental Data," *J. Opt. Soc. Am. A.*, vol. 14, pp. 70–78, 1997.

[56] R. Borghi, F. Gori, M. Santarsiero, F. Frezza, and G. Schettini, "Plane-wave scattering by a perfectly conducting circular cylinder near a plane surface: cylindrical-wave approach," *J. Opt. Soc. Am. A.*, vol. 13, no. 3, p. 483, 1996.

[57] P. B. Wong, G. L. Tyler, J. E. Baron, E. M. Gurrola, and R. A. Simpson, "A Three-wave FDTD Approach to Surface Scattering with Applications to Remote Sensing of Geophysical Surfaces," *IEEE Trans. Antenn. Propag.*, vol. 44, no. 4, pp. 504–514, 1996.

[58] S. C. Lee, "Scattering at Oblique Incidence by Multiple Cylinders in Front of a Surface," *J.Quant. Spectrosc. Radiat. Transf.*, vol. 182, pp. 119–127, 2016.

[59] R. Lee and A. C. Cangellaris, "Scattering from an Arbitrary Cylinder in the Presence of a Parallel Planar Media Interface Using the by Moment Method," *PIER*, vol. 4, pp. 345–372, 1991.

[60] A. Kizilay and E. Rothwell, "Transient Te Scattering from a Cylinder Above an Infinite Periodic Surface Using a Decomposition Method," *Journal of Electromagnetic Waves and Applications*, vol. 15, no. 3, pp. 293–314, 2001.

[61] C. Ozzaim, "Plane wave scattering by a conducting cylinder located near an interface between two dielectric half-spaces: a perturbation method," *IEEE Trans. Antennas Propag.*, vol. 65, no. 5, pp. 2754–2758, 2017.

[62] C. Ozzaim, "A MoM solution for TM scattering by dielectric cylinders above an infinite flat surface," *Journal of Modern Optics*, vol. 60, no. 15, pp. 1550–1557, 2019.

[63] G. Videen and W. S. Bickel, "Light-scattering Mueller matric for a rough fiber," *Appl. Opt.*, vol. 31, pp. 3488–3492, 1992.

[64] D. W. Pohl and D. Courjon, "Near Field optics," *NATO Advanced Science Institutes Series*, vol. 242, 1993.

[65] F. Frezza, F. Gori, M. Santarsiero, F. Santini, and G. S. tini, "Quasi-optical launchers for lower hybrid waves: a full-wave approach," *Nucl. Fusion*, vol. 34, no. 1239-1246, 1994.

[66] R. Petit, "Electromagnetic Theory of Gratings," *Nucl. Fusion*, vol. 34, 1980.

[67] D. W. Pohl, "Scanning near field optical microscopy (SNOM)," *Advances in Optical and Electron Microscopy*, 1990.

[68] C. Girard and D. Courjon, "Model for scanning tunneling optical microscopy: a microscopic self-consistent approach," *Phys. Rev. B*, vol. 42, no. 9340-9349, 1990.

[69] D. V. Labeke and D. Barchiesi, "Scanning tunneling optical microscopy: a theoretical macroscopic approach," *J. Opt. Soc. Am. A*, vol. 9, no. 732-739, 1992.

[70] B. Tian, T. Kempa, and C. Lieber, "Single nanowire photovoltaics," *Chem. Soc. Rev.*, vol. 38, no. 16-24, 2009.

[71] J. Wang, M. S. Gudiksen, X. Duan, Y. Cui, and C. M. Lieber, "Highly polarized photoluminescence and photodetection from single indium phosphide nanowires," *Science*, vol. 293, no. 1455-1457, 2001.

[72] O. Muskens, J. Rivas, R. Algra, E. Bakkers, and A. Lagendijk, "Design of light scattering in nanowire materials for photovoltaic applications," *Nano Lett.*, vol. 8, no. 2638-2642, 2008.

[73] M. Kelzenberg, S. Boettcher, J. Petykiewicz, D. Turner-Evans, M. Putnam, E. Warren, J. Spurgeon, R. Briggs, N. Lewis, and H. Atwater, "Enhanced absorption and carrier collection in si wire arrays for photovoltaic applications," *Nat. Mater.*, vol. 9, no. 239-244, 2010.

[74] L. Cao, P. Fan, A. Vasudev, J. White, Z. Yu, W. Cai, J. Schuller, S. Fan, and M. Brongersma, "Semiconductor nanowire optical antenna solar absorbers," *Nano Lett.*, vol. 10, no. 439-445, 2010.

[75] M. Apra, M. D. Amore, K. Gigliotti, M. S. Sarto, and V. Volpi, "Lightning indirect effects certification of a transport aircraft by numerical simulation," *IEEE Trans. Electromagn. Compat.*, vol. 50, no. 513-523, 2008.

[76] R. Holland and R. S. John, "EM pickup and scattering by a wire," *IEEE Trans. Electromagn. Compat.*, vol. 42, no. 461-469, 2000.

[77] M. S. Sarto, "Electromagnetic interference from carrier channels on finite-length power lines above a lossy ground in a wide frequency range," *IEEE Trans. Power Deliv.*, vol. 13, no. 336-343, 1998.

[78] R. F. Harrington, "Time-Harmonic Electromagnetic Fields," *Wiley-IEEE Press*, 2001.

[79] M. S. Kluskens and E. H. Newman, "Image theory for chiral bodies," *IEEE Transactions on Antenna. and Propagation*, vol. 39, no. 5, pp. 676–677, 1991.

[80] C. Caloz and A. Sihvola, "Electromagnetic chirality," *Physics, Optics, arXiv:1903.09087*, 2019.

[81] C. Caloz and A. Sihvola, "Electromagnetic chirality, part 1: The microscopic perspective," *IEEE Antennas and Propagation Magazine*, vol. 62, no. 1, pp. 58–72, 2020.

[82] C. Caloz and A. Sihvola, "Electromagnetic chirality, part 2: The macroscopic perspective [electromagnetic perspectives]," *IEEE Antennas and Propagation Magazine*, vol. 62, no. 2, pp. 82–98, 2020.

[83] D. L. Jaggard and N. Engheta, "CHIROSORB as an invisible medium," *IEEE Electronics Letters*, vol. 25, no. 3, 1989.

[84] MATLAB, "Function Reference," *Natick, MA, The MathWorks, Inc.*, 2020.

[85] R. F. Harrington, "Matrix Methods for Field Problems," *Proc. IEEE*, vol. 55, pp. 136–149, 1967.

[86] J. R. Mautz and R. F. Harrington, "Radiation and Scattering from Bodies of Revolution," *Appl. Sci. Res.*, vol. 20, pp. 405–435, 1969.

[87] A. W. Gilsson and D. R. Wilton, "Simple and Efficient Numerical Methods for Problems of Electromagnetic Radiation and Scattering from Surfaces," *IEEE Trans. Antennas Propagation*, vol. 28, pp. 593–603, 1980.

[88] E. Arvas and T. K. Sarkar, "RCS of two-dimensional structures consisting of both dielectrics and conductors of arbitrary cross section," *IEEE Trans. Antennas Propagation*, vol. 37, pp. 546–554, 1989.

[89] E. Arvas, S.M.Rao, and T.K.Sarkar, "E-field solution of TM-scattering from multiple perfectly conducting and lossy dielectric cylinders of arbitrary cross-section," *IEEE Proceedings*, vol. 133, no. 2, 1986.

[90] E. Arvas and J. R. Mautz, "On the Non-Uniqueness of the Surface EFIE Applied to Multiple Conducting and/or Dielectric Bodies," *AEU. Archiv fur Elektronik und Ubertragungstechnik*, vol. 42, no. 6, 1988.

Appendix A

Plane Waves in a Chiral Medium

In this appendix, a brief introduction to plane waves in a chiral medium will be given. Then, the plane waves produced by an infinite electric current sheet will be introduced.

A.0.1 General Plane Waves

The source-free Maxwell's equations are as follows (e^{jwt} time dependence assumed);

$$\boldsymbol{\nabla} \times \mathbf{E} = -j\omega\mathbf{B} \tag{A.1}$$

$$\boldsymbol{\nabla} \times \mathbf{H} = j\omega\mathbf{D} \tag{A.2}$$

For a chiral material, there exists a few different set of constitutive relations. Here, the following two equations will be used.

$$\mathbf{D} = \epsilon\mathbf{E} - j\gamma\mathbf{B} \tag{A.3}$$

$$\mathbf{B} = \mu\mathbf{H} + j\gamma\mu\mathbf{E} \tag{A.4}$$

Where, γ is known as chiral admittance. Using (A.3) and (A.4) in (A.1) and (A.2) gives the following source-free Maxwell's equations in a chiral medium.

$$\boldsymbol{\nabla} \times \mathbf{E} = \omega(\gamma\mu\mathbf{E} - j\mu\mathbf{H}) \tag{A.5}$$

$$\boldsymbol{\nabla} \times \mathbf{H} = \omega\big[j(\epsilon + \mu\gamma^2)\mathbf{E} + \gamma\mu\mathbf{H}\big] \tag{A.6}$$

Lets us find that for which real values of h, a plane wave exists as follows

$$\mathbf{E}(z) = \big(\hat{x}E_x + \hat{y}E_y\big)e^{-jhz} \tag{A.7}$$

$$\mathbf{H}(z) = \big(\hat{x}H_x + \hat{y}H_y\big)e^{-jhz} \tag{A.8}$$

Then (A.7) and (A.8) in (A.5) gives:

$$\hat{x}jhE_y - \hat{y}jhE_x = -j\omega\mu\big(\hat{x}H_x + \hat{y}H_y\big) + \omega\mu\gamma\big(\hat{x}E_x + \hat{y}E_y\big) \tag{A.9}$$

$$\hat{x}jhH_y - \hat{y}jhH_x = j\omega\big(\epsilon + \mu\gamma^2\big)\big(\hat{x}E_x + \hat{y}E_y\big) + \omega\mu\gamma\big(\hat{x}H_x + \hat{y}H_y\big) \tag{A.10}$$

(A.9) and (A.10) gives;

$$jhE_y + j\omega\mu H_x - \omega\mu\gamma E_x = 0 \tag{A.11}$$

$$-jhE_x + j\omega\mu H_y - \omega\mu\gamma E_y = 0 \tag{A.12}$$

$$jhH_y - j\omega\big(\epsilon + \mu\gamma^2\big)E_x - \omega\mu\gamma H_x = 0 \tag{A.13}$$

$$-jhH_x - j\omega\big(\epsilon + \mu\gamma^2\big)E_y - \omega\mu\gamma H_y = 0 \tag{A.14}$$

Equations (A.11) – (A.14) can be written in matrix form as;

$$\begin{bmatrix} -\omega\mu\gamma & jh & j\omega\mu & 0 \\ -jh & -\omega\mu\gamma & 0 & j\omega\mu \\ -j\omega\big(\epsilon + \mu\gamma^2\big) & 0 & -\omega\mu\gamma & jh \\ 0 & -j\omega\big(\epsilon + \mu\gamma^2\big) & -jh & -\omega\mu\gamma \end{bmatrix} \begin{bmatrix} E_x \\ E_y \\ H_x \\ H_y \end{bmatrix} = \begin{bmatrix} 0 \\ 0 \\ 0 \\ 0 \end{bmatrix} \tag{A.15}$$

To find h, the determinant of the matrix must be zero. By solving the matrix we obtained;

$$h_1 = \omega\mu\gamma + \sqrt{\omega^2\mu\epsilon + (\omega\mu\gamma)^2} \tag{A.16}$$

$$h_2 = -\omega\mu\gamma + \sqrt{\omega^2\mu\epsilon + (\omega\mu\gamma)^2} \tag{A.17}$$

It can be shown that $h_3 = -h_1$ and $h_4 = -h_2$ are also solutions. Note that h_1 and h_2 are wave numbers for $+z$ traveling waves. Similarly, h_3 and h_4 are corresponding wave numbers for $-z$ traveling waves.

Replacing h_1 in eqns. (A.11) – (A.14) gives;

$$jh_1E_y + j\omega\mu H_x - \omega\mu\gamma E_x = 0 \tag{A.18}$$

$$-jh_1E_x + j\omega\mu H_y - \omega\mu\gamma E_y = 0 \tag{A.19}$$

$$jh_1H_y - j\omega\big(\epsilon + \mu\gamma^2\big)E_x - \omega\mu\gamma H_x = 0 \tag{A.20}$$

$$-jh_1H_x - j\omega\big(\epsilon + \mu\gamma^2\big)E_y - \omega\mu\gamma H_y = 0 \tag{A.21}$$

Rearranging eqns. (A.18) and (A.19) give:

$$H_x = \frac{\omega\mu\gamma E_x - jh_1E_y}{j\omega\mu} \tag{A.22}$$

$$H_y = \frac{\omega\mu\gamma E_y + jh_1E_x}{j\omega\mu} \tag{A.23}$$

Replacing the values of H_x and H_y in eqn. (A.20) gives:

$$E_y = -jE_x \tag{A.24}$$

Replacing E_y in (A.23) reveals that

$$H_y = \frac{E_x}{\eta_c} \tag{A.25}$$

Similarly, one can show that

$$H_x = jH_y \tag{A.26}$$

With these new definitions, eqns. (A.7) and (A.8) can be rewritten as:

$$\mathbf{E}_R^+ = A(\hat{x} - j\hat{y})e^{-jh_1z} \tag{A.27}$$

$$\mathbf{H}_R^+ = \frac{A}{\eta_c}(j\hat{x} + \hat{y})e^{-jh_1z} \tag{A.28}$$

It can be shown that the following $(\mathbf{E}_R^+, \mathbf{H}_R^+)$ is a solution to (A.5) and (A.6). Where, A is an arbitrary constant, and the wavenumber (h_1) and the wave impedance (η_c) are given by;

$$h_1 = \omega\mu\gamma + \sqrt{k^2 + (\omega\mu\gamma)^2} \tag{A.29}$$

$$\eta_c = \frac{\eta}{\sqrt{1 + (\eta\gamma)^2}} \tag{A.30}$$

here, $k = \omega\sqrt{\mu\epsilon}$ and $\eta = \sqrt{\mu/\epsilon}$.

The $(\mathbf{E}_R^+, \mathbf{H}_R^+)$ in (A.27) and (A.28) represent a right-hand circularly polarized (RHCP) uniform ($\frac{\partial}{\partial x} = 0 = \frac{\partial}{\partial y}$) plane wave travelling in $+z$ direction with the wave number h_1.

Similar procedure can be followed, and it can be demonstrate that by replacing h_2 in eqns. (A.11) − (A.14) gives

$$E_y = jE_x \tag{A.31}$$

$$H_y = \frac{E_x}{\eta_c} \tag{A.32}$$

and

$$H_x = -jH_y \tag{A.33}$$

Similarly, it can be shown that the following $(\mathbf{E}_L^+, \mathbf{H}_L^+)$ is also a solution to (A.5) and (A.6).

$$\mathbf{E}_L^+ = C(\hat{x} + j\hat{y})e^{-jh_2 z} \tag{A.34}$$

$$\mathbf{H}_L^+ = \frac{C}{\eta_c}(\hat{y} - j\hat{x})e^{-jh_2 z} \tag{A.35}$$

Where, C is an arbitrary constant, and the wavenumber (h_2) is given by;

$$h_2 = -\omega\mu\gamma + \sqrt{k^2 + (\omega\mu\gamma)^2} \tag{A.36}$$

The $(\mathbf{E}_L^+, \mathbf{H}_L^+)$ in (A.34) and (A.35) represent a left-hand circularly polarized (LHCP) uniform ($\frac{\partial}{\partial x} = 0 = \frac{\partial}{\partial y}$) plane wave travelling in $+z$ direction with the wave number h_2.

Note that if h_1 in (A.27) and (A.28) is replaced with h_2, the resulting fields will not satisfy (A.5) and (A.6). Similarly, if h_2 in (A.34) and (A.35) is replaced with h_1, the resulting fields will not satisfy (A.5) and (A.6). In other words, h_1 is the wave number for a RHCP wave and h_2 is the wave number for a LHCP wave. Note also that a uniform plane wave of the following form with arbitrary E_x and E_y and $h = h_1$ or $h = h_2$ will not satisfy (A.5) and (A.6).

$$\mathbf{E}(z) = \big(\hat{x}E_x + \hat{y}E_y\big)e^{-jhz} \tag{A.37a}$$

$$\mathbf{H}(z) = \big(\hat{x}H_x + \hat{y}H_y\big)e^{-jhz} \tag{A.37b}$$

In other words, the uniform plane wave cannot be linearly or elliptically polarized. It has to be circularly polarized.

Since (A.5) and (A.6) are homogeneous the sum of $(\mathbf{E}_R^+, \mathbf{H}_R^+)$ and $(\mathbf{E}_L^+, \mathbf{H}_L^+)$ given below will be the general form of a uniform plane wave traveling in a chiral medium (ϵ, μ, γ) in $+z$ direction.

$$\mathbf{E}^+ = A(\hat{x} - j\hat{y})e^{-jh_1 z} + C(\hat{x} + j\hat{y})e^{-jh_2 z} \tag{A.38}$$

$$\mathbf{H}^+ = \frac{A}{\eta_c}(\hat{y} + j\hat{x})e^{-jh_1 z} + \frac{C}{\eta_c}(\hat{y} - j\hat{x})e^{-jh_2 z} \tag{A.39}$$

Similarly, $(\mathbf{E}^-, \mathbf{H}^-)$ given below is the general form a plane wave traveling in $-z$ direction in a chiral medium (ϵ, μ, γ).

$$\mathbf{E}^- = F(\hat{x} + j\hat{y})e^{jh_1 z} + G(\hat{x} - j\hat{y})e^{jh_2 z} \tag{A.40}$$

$$\mathbf{H}^- = \frac{F}{\eta_c}(-\hat{y} + j\hat{x})e^{jh_1 z} + \frac{G}{\eta_c}(-\hat{y} - j\hat{x})e^{jh_2 z} \tag{A.41}$$

Note that the first terms (with wave number h_1) in (A.40) and (A.41) represent a RHCP wave and the second terms (with wave number h_2) represent a LHCP wave traveling in $-z$ direction.

Since the RHCP wave and LHCP wave in (A.38) and (A.39) travel with different velocities, the polarization of the total wave rotates as the wave travels in $+z$ direction. Similarly, polarization rotation exists for the fields in (A.38) and (A.39). For details and much more the reader is referred to elegant papers [80–82].

A.0.2 Plane Waves Produced By an Electric Current Sheet in a Chiral Medium

Figure A.1 shows an infinite current sheet

$$\mathbf{J} = -4J_0\hat{x} \tag{A.42}$$

placed at $z = -d$ plane in an unbounded chiral medium (ϵ, μ, γ). Where J_0 is a constant. The field produced by this source, for $z < -d$ is given by;

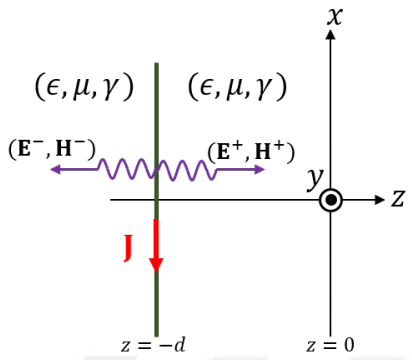

Figure A.1: An infinite current sheet in an unbounded chiral medium.

$$\mathbf{E}^{-}(\mathbf{J}) = \eta_c J_0 \Big\{ (\hat{x} + j\hat{y}) e^{jh_1(z+d)} + (\hat{x} - j\hat{y}) e^{jh_2(z+d)} \Big\} \tag{A.43}$$

$$\mathbf{H}^{-}(\mathbf{J}) = J_0 \Big\{ (-\hat{y} + j\hat{x}) e^{jh_1(z+d)} + (-\hat{y} - j\hat{x}) e^{jh_2(z+d)} \Big\} \tag{A.44}$$

The superscript $-$ represents the field traveling in $-z$ direction. Similarly, the fields for $z > -d$ is given by;

$$\mathbf{E}^{+}(\mathbf{J}) = \eta_c J_0 \Big\{ (\hat{x} - j\hat{y}) e^{-jh_1(z+d)} + (\hat{x} + j\hat{y}) e^{-jh_2(z+d)} \Big\} \tag{A.45}$$

$$\mathbf{H}^{+}(\mathbf{J}) = J_0 \Big\{ (\hat{y} + j\hat{x}) e^{-jh_1(z+d)} + (\hat{y} - j\hat{x}) e^{-jh_2(z+d)} \Big\} \tag{A.46}$$

Note that the pairs (A.43) and (A.44), and (A.45) and (A.46) satisfy (A.5) and (A.6). Furthermore,

$$\mathbf{E}^{+}(\mathbf{J}) = \mathbf{E}^{-}(\mathbf{J}) \quad at \quad z = -d, \tag{A.47}$$

and

$$\hat{z} \times \big[\mathbf{H}^{+}(\mathbf{J}) - \mathbf{H}^{-}(\mathbf{J}) \big] = \mathbf{J} \quad at \quad z = -d. \tag{A.48}$$

Appendix B

Two-Dimensional Fields in Chiral Media

In a chiral medium, a uniform plane wave cannot be linearly or elliptically polarized. It has to be circularly polarized. Since the RHCP wave and LHCP wave travel with different velocities, the polarization of the total wave rotates as the wave travels in a chiral medium. Here, a simple and elegant procedure is followed to derive expressions for the fields produced by sources in a chiral medium. For a chiral material, there exists a few different sets of constitutive relations. Here, the following two equations will be used.

$$\mathbf{D} = \epsilon\mathbf{E} - j\gamma\mathbf{B} \tag{B.1}$$

$$\mathbf{H} = \frac{1}{\mu}\mathbf{B} - j\gamma\mathbf{E} \tag{B.2}$$

where ϵ represents the permittivity and μ represents the permeability of the medium, respectively. The γ is known as chiral admittance. It provides an extra degree of freedom. The positive chiral admittance ($\gamma > 0$) specifies right-handedness while the negative chiral admittance ($\gamma < 0$) defines left-handedness. When γ is zero, the medium is simply dielectric or achiral.

The Maxwell's equations are as follows ($e^{j\omega t}$ time dependence assumed):

$$-\boldsymbol{\nabla} \times \mathbf{E} = j\omega\mathbf{B} + \mathbf{M} \tag{B.3}$$

$$\boldsymbol{\nabla} \times \mathbf{H} = j\omega\mathbf{D} + \mathbf{J} \tag{B.4}$$

Where the electric and magnetic currents are denoted by $\mathbf{J}$ and $\mathbf{M}$, respectively. Maxwell's equation for a chiral medium can be obtained by substituting $(B.1)$ and $(B.2)$ into $(B.3)$ and $(B.4)$:

$$-\boldsymbol{\nabla} \times \mathbf{E} = j\omega\mu\mathbf{H} - \omega\mu\gamma\mathbf{E} + \mathbf{M} \tag{B.5}$$

$$\boldsymbol{\nabla} \times \mathbf{H} = j\omega(\epsilon + \mu\gamma^2)\mathbf{E} + \omega\mu\gamma\mathbf{H} + \mathbf{J} \tag{B.6}$$

These equations can be expressed in matrix form as:

$$\boldsymbol{\nabla} \times \begin{bmatrix} \mathbf{E} \\ \mathbf{H} \end{bmatrix} = K \begin{bmatrix} \mathbf{E} \\ \mathbf{H} \end{bmatrix} + \begin{bmatrix} -\mathbf{M} \\ \mathbf{J} \end{bmatrix} \tag{B.7}$$

where

$$K = \begin{bmatrix} \omega\mu\gamma & -j\omega\mu \\ j\omega(\epsilon + \mu\gamma^2) & \omega\mu\gamma \end{bmatrix} \tag{B.8}$$

The coupling caused by K in the wave equations can be removed by diagonalising such that

$$K = A \begin{bmatrix} h_1 & 0 \\ 0 & -h_2 \end{bmatrix} A^{-1} \tag{B.9}$$

where

$$A = \begin{bmatrix} 1 & 1 \\ \frac{j}{\eta_c} & -\frac{j}{\eta_c} \end{bmatrix} \tag{B.10}$$

$$A^{-1} = \frac{1}{2} \begin{bmatrix} 1 & -j\eta_c \\ 1 & j\eta_c \end{bmatrix} \quad , \tag{B.11}$$

and the chiral admittance of the chiral medium is given by;

$$\eta_c = \frac{\eta}{\sqrt{1 + (\eta\gamma)^2}} \tag{B.12}$$

with

$$\eta = \sqrt{\mu/\epsilon} \quad , \tag{B.13}$$

and h_1 and h_2 are the right- and left-handed wave numbers and are given by,

$$h_1 = \omega\mu\gamma + \sqrt{k^2 + (\omega\mu\gamma)^2} \tag{B.14}$$

$$h_2 = -\omega\mu\gamma + \sqrt{k^2 + (\omega\mu\gamma)^2} \tag{B.15}$$

where $k = \omega\sqrt{\mu\epsilon}$. Premultiplying both sides of $B.7$ by A^{-1}, we obtain

$$\boldsymbol{\nabla} \times A^{-1} \begin{bmatrix} \mathbf{E} \\ \mathbf{H} \end{bmatrix} = A^{-1} K A A^{-1} \begin{bmatrix} \mathbf{E} \\ \mathbf{H} \end{bmatrix} + A^{-1} \begin{bmatrix} -\mathbf{M} \\ \mathbf{J} \end{bmatrix} \tag{B.16}$$

The RHCP $(+)$ and LHCP $(-)$ fields and currents in a chiral medium are given by;

$$\begin{bmatrix} \mathbf{E}^+ \\ \mathbf{E}^- \end{bmatrix} = A^{-1} \begin{bmatrix} \mathbf{E} \\ \mathbf{H} \end{bmatrix} \tag{B.17}$$

$$\begin{bmatrix} \mathbf{M}^+ \\ \mathbf{M}^- \end{bmatrix} = -A^{-1} \begin{bmatrix} -\mathbf{M} \\ \mathbf{J} \end{bmatrix} \tag{B.18}$$

$$\mathbf{H}^{\pm} = \pm \frac{j\mathbf{E}^{\pm}}{\eta_c} \tag{B.19}$$

$$\mathbf{J}^{\pm} = \mp \frac{j\mathbf{M}^{\pm}}{\eta_c} \tag{B.20}$$

Substituting $(B.11)$ into $(B.17)$ yields;

$$\mathbf{E}^{\pm} = \frac{1}{2}(\mathbf{E} \mp j\eta_c \mathbf{H}) \tag{B.21}$$

Substituting $(B.21)$ into $(B.19)$ gives;

$$\mathbf{H}^{\pm} = \frac{1}{2}(\mathbf{H} \pm \frac{j}{\eta_c}\mathbf{E}) \tag{B.22}$$

Similarly, for right-handed and left-handed currents, substituting $(B.11)$ into $(B.18)$, we obtain

$$\mathbf{M}^{\pm} = \frac{1}{2}(\mathbf{M} \pm j\eta_c \mathbf{J}) \tag{B.23}$$

Substituting $(B.23)$ into $(B.20)$ gives;

$$\mathbf{J}^{\pm} = \frac{1}{2}(\mathbf{J} \mp \frac{j}{\eta_c}\mathbf{M}) \tag{B.24}$$

To express Maxwell's equations ($B.7$) in terms of $\mathbf{E}^{\pm}$ and $\mathbf{H}^{\pm}$, we obtain

$$\boldsymbol{\nabla} \times \mathbf{E}^{\pm} = -j\omega\mu\mathbf{H}^{\pm} - \mathbf{M}^{\pm} \tag{B.25}$$

$$\boldsymbol{\nabla} \times \mathbf{H}^{\pm} = j\omega\epsilon\mathbf{E}^{\pm} + \mathbf{J}^{\pm} \tag{B.26}$$

With these new definitions for fields and currents, Maxwell's equations must be satisfied. In Maxwell's equations ($B.3$) and ($B.4$) replacing $\mathbf{E}$ by

$$\mathbf{E} = \mathbf{E}^{+} + \mathbf{E}^{-} \tag{B.27}$$

and replacing $\mathbf{H}$ by

$$\mathbf{H} = \mathbf{H}^{+} + \mathbf{H}^{-} \tag{B.28}$$

and replacing $\mathbf{J}$ by

$$\mathbf{J} = \mathbf{J}^{+} + \mathbf{J}^{-} \tag{B.29}$$

and replacing $\mathbf{M}$ by

$$\mathbf{M} = \mathbf{M}^{+} + \mathbf{M}^{-} \tag{B.30}$$

gives the following equations:

$$\begin{aligned}\boldsymbol{\nabla} \times \frac{(\mathbf{E} - j\eta_c\mathbf{H})}{2} + \boldsymbol{\nabla} \times \frac{(\mathbf{E} + j\eta_c\mathbf{H})}{2} \\ = -j\omega\mu\frac{(\mathbf{H} + \frac{j}{\eta_c}\mathbf{E})}{2} - \frac{(\mathbf{M} + j\eta_c\mathbf{J})}{2} - j\omega\mu\frac{(\mathbf{H} - \frac{j}{\eta_c}\mathbf{E})}{2} - \frac{(\mathbf{M} - j\eta_c\mathbf{J})}{2}\end{aligned} \tag{B.31}$$

$$\begin{aligned}\boldsymbol{\nabla} \times \frac{(\mathbf{H} + \frac{j}{\eta_c}\mathbf{E})}{2} + \boldsymbol{\nabla} \times \frac{(\mathbf{H} - \frac{j}{\eta_c}\mathbf{E})}{2} \\ = j\omega\epsilon\frac{(\mathbf{E} - j\eta_c\mathbf{H})}{2} + \frac{(\mathbf{J} - \frac{j}{\eta_c}\mathbf{M})}{2} + j\omega\epsilon\frac{(\mathbf{E} + j\eta_c\mathbf{H})}{2} + \frac{(\mathbf{J} + \frac{j}{\eta_c}\mathbf{M})}{2}\end{aligned} \tag{B.32}$$

Rearranging the above equations give:

$$-\boldsymbol{\nabla} \times \mathbf{E} = j\omega\mu\mathbf{H} - \omega\mu\gamma\mathbf{E} + \mathbf{M} \tag{B.33}$$

$$\boldsymbol{\nabla} \times \mathbf{H} = j\omega(\epsilon + \mu\gamma^2)\mathbf{E} + \omega\mu\gamma\mathbf{H} + \mathbf{J} \tag{B.34}$$

The equations ($B.33$) and ($B.34$) are obtained using RHCP and LHCP fields $(\mathbf{E}^{\pm}, \mathbf{H}^{\pm})$ and currents $(\mathbf{J}^{\pm}, \mathbf{M}^{\pm})$, and are identical to the Maxwell's equations in

a chiral medium given by $(B.5)$ and $(B.6)$. It is now clear that only a circularly polarized wave of two opposite handedness exists in a chiral medium. These waves have different phase velocities, wavenumbers, and attenuation rates. In other words, a linearly or elliptically polarized wave cannot exist in a chiral medium. By using two-dimensional Green's functions with some algebraic manipulations, one can find the electric and magnetic fields due to electric and magnetic sources radiating in an unbounded chiral medium [44]. For the sake of completeness, the electric and magnetic fields due to the electric and magnetic current sources, radiating in an unbounded chiral region are given by;

$$\begin{aligned}
\mathbf{E}(\mathbf{J},\mathbf{M}) = &-\frac{\eta_c}{8}\int_C \Big\{h_1 H_0^{(2)}(h_1|\boldsymbol{\rho}-\boldsymbol{\rho}'|) + h_2 H_0^{(2)}(h_2|\boldsymbol{\rho}-\boldsymbol{\rho}'|)\Big\}\mathbf{J}(\boldsymbol{\rho}')dl' \\
&-\frac{\eta_c}{8}\int_C \Big\{\boldsymbol{\nabla} H_0^{(2)}(h_1|\boldsymbol{\rho}-\boldsymbol{\rho}'|) - \boldsymbol{\nabla} H_0^{(2)}(h_2|\boldsymbol{\rho}-\boldsymbol{\rho}'|)\Big\}\times\mathbf{J}(\boldsymbol{\rho}')dl' \\
&-\frac{\eta_c}{8}\boldsymbol{\nabla}\int_C \Big\{h_1^{-1} H_0^{(2)}(h_1|\boldsymbol{\rho}-\boldsymbol{\rho}'|) + h_2^{-1} H_0^{(2)}(h_2|\boldsymbol{\rho}-\boldsymbol{\rho}'|)\Big\}\boldsymbol{\nabla}'\cdot\mathbf{J}(\boldsymbol{\rho}')dl' \\
&+\frac{j}{8}\int_C \Big\{h_1 H_0^{(2)}(h_1|\boldsymbol{\rho}-\boldsymbol{\rho}'|) - h_2 H_0^{(2)}(h_2|\boldsymbol{\rho}-\boldsymbol{\rho}'|)\Big\}\mathbf{M}(\boldsymbol{\rho}')dl' \\
&+\frac{j}{8}\int_C \Big\{\boldsymbol{\nabla} H_0^{(2)}(h_1|\boldsymbol{\rho}-\boldsymbol{\rho}'|) + \boldsymbol{\nabla} H_0^{(2)}(h_2|\boldsymbol{\rho}-\boldsymbol{\rho}'|)\Big\}\times\mathbf{M}(\boldsymbol{\rho}')dl' \\
&+\frac{j}{8}\boldsymbol{\nabla}\int_C \Big\{h_1^{-1} H_0^{(2)}(h_1|\boldsymbol{\rho}-\boldsymbol{\rho}'|) - h_2^{-1} H_0^{(2)}(h_2|\boldsymbol{\rho}-\boldsymbol{\rho}'|)\Big\}\boldsymbol{\nabla}'\cdot\mathbf{M}(\boldsymbol{\rho}')dl'
\end{aligned} \tag{B.35}$$

$$\begin{aligned}
\mathbf{H}(\mathbf{J},\mathbf{M}) = &-\frac{j}{8}\int_C \Big\{h_1 H_0^{(2)}(h_1|\boldsymbol{\rho}-\boldsymbol{\rho}'|) - h_2 H_0^{(2)}(h_2|\boldsymbol{\rho}-\boldsymbol{\rho}'|)\Big\}\mathbf{J}(\boldsymbol{\rho}')dl' \\
&-\frac{j}{8}\int_C \Big\{\boldsymbol{\nabla} H_0^{(2)}(h_1|\boldsymbol{\rho}-\boldsymbol{\rho}'|) + \boldsymbol{\nabla} H_0^{(2)}(h_2|\boldsymbol{\rho}-\boldsymbol{\rho}'|)\Big\}\times\mathbf{J}(\boldsymbol{\rho}')dl' \\
&-\frac{j}{8}\boldsymbol{\nabla}\int_C \Big\{h_1^{-1} H_0^{(2)}(h_1|\boldsymbol{\rho}-\boldsymbol{\rho}'|) - h_2^{-1} H_0^{(2)}(h_2|\boldsymbol{\rho}-\boldsymbol{\rho}'|)\Big\}\boldsymbol{\nabla}'\cdot\mathbf{J}(\boldsymbol{\rho}')dl' \\
&-\frac{1}{8\eta_c}\int_C \Big\{h_1 H_0^{(2)}(h_1|\boldsymbol{\rho}-\boldsymbol{\rho}'|) + h_2 H_0^{(2)}(h_2|\boldsymbol{\rho}-\boldsymbol{\rho}'|)\Big\}\mathbf{M}(\boldsymbol{\rho}')dl' \\
&-\frac{1}{8\eta_c}\int_C \Big\{\boldsymbol{\nabla} H_0^{(2)}(h_1|\boldsymbol{\rho}-\boldsymbol{\rho}'|) - \boldsymbol{\nabla} H_0^{(2)}(h_2|\boldsymbol{\rho}-\boldsymbol{\rho}'|)\Big\}\times\mathbf{M}(\boldsymbol{\rho}')dl' \\
&-\frac{1}{8\eta_c}\boldsymbol{\nabla}\int_C \Big\{h_1^{-1} H_0^{(2)}(h_1|\boldsymbol{\rho}-\boldsymbol{\rho}'|) + h_2^{-1} H_0^{(2)}(h_2|\boldsymbol{\rho}-\boldsymbol{\rho}'|)\Big\}\boldsymbol{\nabla}'\cdot\mathbf{M}(\boldsymbol{\rho}')dl'
\end{aligned} \tag{B.36}$$

The equations derived in $(B.35)$ and $(B.36)$ are the two dimensional field equations for an unbounded chiral medium. Here, C denotes the contour describing a cross-section of the surface in the $xy-$plane, $|\boldsymbol{\rho} - \boldsymbol{\rho}'|$ is the distance between the field and source point, and $H_0^{(2)}$ is the Hankel function of zeroth order and second kind. These equations reduce to achiral medium field equations for $\gamma = 0$.

Appendix C

Detailed Computation of Some Moment Matrix Elements

The moment matrix in (3.9) is $8N \times 8N$ square matrix. Each element in a moment matrix is $N \times N$ sub-matrice. The purpose of this appendix is to understand typical elements of different sub-matrices, and obtain expression to compute these elements.

Consider a surface S with constant cross-section in the z-direction. Let C be the contour describing a cross−section of S. The electric field produced by currents $\mathbf{J}$ and $\mathbf{M}$ residing on S in an unbounded medium is given by:

$$\mathbf{E}(\mathbf{J}, \mathbf{M}) = \mathbf{E}(\mathbf{J}, 0) + \mathbf{E}(0, \mathbf{M}) \tag{C.1}$$

where,

$$\mathbf{E}(\mathbf{J}, 0) = -j\omega\mu\mathbf{A} \tag{C.2}$$

and,

$$\mathbf{E}(0, \mathbf{M}) = -\boldsymbol{\nabla} \times \mathbf{F}. \tag{C.3}$$

Here,

$$\mathbf{A}(\boldsymbol{\rho}) = \frac{1}{4j} \int_C \mathbf{J}(\boldsymbol{\rho}') H_0^{(2)}(k_\rho |\boldsymbol{\rho} - \boldsymbol{\rho}'|) dl' \tag{C.4}$$

and,

$$\mathbf{F}(\boldsymbol{\rho}) = \frac{1}{4j}\int_C \mathbf{M}(\boldsymbol{\rho}')H_0^{(2)}(k_\rho|\boldsymbol{\rho}-\boldsymbol{\rho}'|)dl' \tag{C.5}$$

$\mathbf{ZJ_Z110}$:

An element in the m^{th} row and the n^{th} column of the sub-matrix $\mathrm{ZJ_Z}110$ is the z-component of the electric field on the m^{th} segment of S_1, produced by $\mathrm{J_Z}$ on the n^{th} segment of S_1, when this $\mathrm{J_Z}$ radiates in the unbounded medium (ϵ_0, μ_0). This element is given by

$$\mathrm{ZJ_Z}110(m,n) = \frac{-\eta_0 k_0 l_{m_1}}{4}\int_{C_{n_1}} H_0^{(2)}(k_0|\boldsymbol{\rho}_{cm_1}-\boldsymbol{\rho}'|)dl' \tag{C.6}$$

Here, η_0 and k_0 denote the wave impedance and the wave number of free space respectively. C_{n_1} represents the n^{th} segment on S_1, and l_{m_1} represents the length of the m^{th} field segment on S_1. The position vector $\boldsymbol{\rho}'$ represents an arbitrary point on C_{n_1} and the position vector $\boldsymbol{\rho}_{cm}$ represents the center of the field segment C_{m_1} on S_1, and $H_0^{(2)}$ is the zeroth order Hankel function of the second kind. When field and source are on the same segment ($m = n$), the small argument approximation for the Hankel function given by

$$H_0^{(2)}(R) \cong 1 - j\frac{2}{\pi}\ln\frac{\gamma R}{2} \tag{C.7}$$

is used. Here, $\ln(\gamma) = 0.5772...$, is the Euler constant.

To compute the mn^{th} element of $\mathrm{ZJ_Z}120(m,n)$, we replace C_{n_1} in (C.6) with C_{n_2}. Similarly, when we replace in (C.6), $l_{m_1}, C_{n_1}, \boldsymbol{\rho}_{cm_1}$ with $l_{m_2}, C_{n_2}, \boldsymbol{\rho}_{cm_2}$ respectively, we obtain $\mathrm{ZJ_Z}220(m,n)$. The elements of $\mathrm{ZJ_Z}210$ contain the fields on S_2 produced by the sources on S_1.

The sub-matrices $\mathrm{ZJ_L}110, \mathrm{ZM_Z}110, \mathrm{ZJ_L}120, \mathrm{ZM_Z}120, \mathrm{ZJ_L}210, \mathrm{ZM_Z}210, \mathrm{ZJ_L}220$, and $\mathrm{ZM_Z}220$ are identically zero.

The sub-matrices in the 2^{nd} row of (3.9) contain the lateral field on S_1, produced by different sources radiating in the unbounded medium (ϵ_0, μ_0). Therefore, $\mathrm{LJ_Z}110, \mathrm{LM_L}110$, $\mathrm{LJ_Z}120$, and $\mathrm{LM_L}120$ are identically zero. Similarly, the sub-matrices $\mathrm{LJ_Z}210, \mathrm{LM_L}210, \mathrm{LJ_Z}220$, and $\mathrm{LM_L}220$ are identically zero.

$\mathbf{ZM_L110}$:

An element in the m^{th} row and the n^{th} column of the sub-matrix $\mathrm{ZM_L}110$ is the z-component of the electric field on the m^{th} segment of S_1, produced by $\mathrm{M_L}$ on the n^{th} segment of S_1, when this $\mathrm{M_L}$ radiates in the unbounded medium (ϵ_0, μ_0). This element is given by

$$\mathrm{ZM_L}110(m,n) = -j\frac{k_0 l_{m_1}}{4}\int_{C_{n_1}} \hat{n}_1.\frac{(\boldsymbol{\rho}_{cm_1} - \boldsymbol{\rho}')}{|\boldsymbol{\rho}_{cm_1} - \boldsymbol{\rho}'|} \times H_1^{(2)}(k_0|\boldsymbol{\rho}_{cm_1} - \boldsymbol{\rho}'|)dl' \quad \text{(C.8)}$$

Here, $\hat{n}_1 = \hat{t}_{n_1} \times \hat{z}$ is the unit vector normal to the source segment C_{n_1} on S_1, and $\hat{t}_{n_1}$ is the unit vector tangent to the same segment, and $H_1^{(2)}$ is the first order Hankel function of the second kind. The typical elements of the sub-matrices $\mathrm{ZM_L}120, \mathrm{ZM_L}210$, and $\mathrm{ZM_L}220$ have similar form as (C.8).

The charge associated with the lateral current of the m^{th} segment is approximated by two displaced pulses as shown in Fig. C.1.

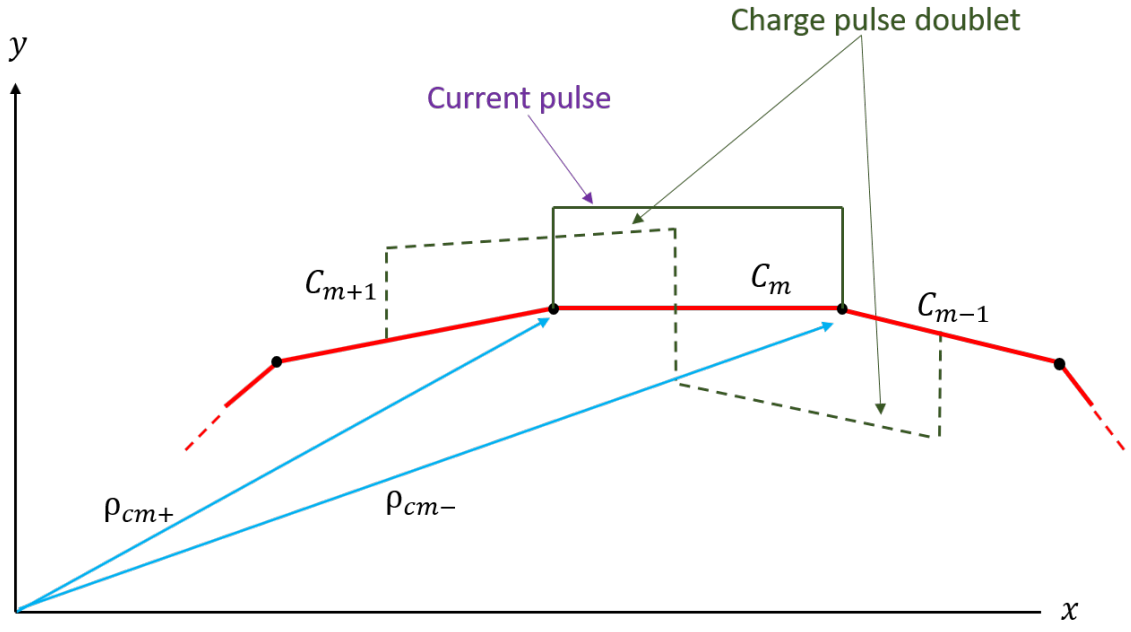

Figure C.1: The lateral current on the m^{th} segment of surface S and the charge associated with it.

$\mathbf{LJ_L110}$:

An element in the m^{th} row and the n^{th} column of the sub-matrix $\mathrm{LJ_L}110$ is the lateral component of the electric field on the m^{th} segment of S_1, produced by $\mathrm{J_L}$ on the n^{th} segment of S_1, when this $\mathrm{J_L}$ radiates in the unbounded medium (ϵ_0, μ_0). This element is approximately given by

$$\begin{aligned}\mathrm{LJ_L}110(m,n) = &-\frac{k_0\eta_0}{4}(\hat{t}_{m_1}\cdot\hat{t}_{n_1})l_{m_1}\int_{C_{n_1}} H_0^{(2)}(k_0|\boldsymbol{\rho}_{cm_1}-\boldsymbol{\rho}^{'}|)dl^{'}\\ &-\frac{\eta_0}{4k_0l_{n_1}}\Big\{\int_{\left[C_{n_1-\frac{1}{2}}+C_{n_1+\frac{1}{2}}\right]} H_0^{(2)}(k_0|\boldsymbol{\rho}_{cm_1+}-\boldsymbol{\rho}^{'}|)dl^{'}\\ &-\int_{\left[C_{n_1-\frac{1}{2}}+C_{n_1+\frac{1}{2}}\right]} H_0^{(2)}(k_0|\boldsymbol{\rho}_{cm_1-}-\boldsymbol{\rho}^{'}|)dl^{'}\Big\} \quad \text{(C.9)}\end{aligned}$$

Where, $C_{n_1-\frac{1}{2}}+C_{n_1+\frac{1}{2}}$ shows the domain of the two charge pulses (shown by the dotted lines) as in Fig. C.1. In (C.9), $\boldsymbol{\rho}_{cm_1-}$ and $\boldsymbol{\rho}_{cm_1+}$, respectively denote the beginning and the end of n^{th} segment on S_1 as shown in Fig. C.1. The typical elements of the sub-matrices $\mathrm{LJ_L}120, \mathrm{LJ_L}210$, and $\mathrm{LJ_L}220$ have similar form as (C.9).

$\mathbf{LM_Z110}$:

An element in the m^{th} row and the n^{th} column of the sub-matrix $\mathrm{LM_Z}110$ is the lateral component of the electric field on the m^{th} segment of S_1, produced by $\mathrm{M_Z}$ on the n^{th} segment of S_1, when this $\mathrm{M_Z}$ radiates in the unbounded medium (ϵ_0, μ_0). This element is approximately given by

$$\mathrm{LM_Z}110(m,n) = j\frac{k_0 l_{m_1}}{4}\int_{C_{n_1}} \hat{n}_f\cdot\frac{(\boldsymbol{\rho}_{cm_1}-\boldsymbol{\rho}^{'})}{|\boldsymbol{\rho}_{cm_1}-\boldsymbol{\rho}^{'}|}\times H_1^{(2)}(k_0|\boldsymbol{\rho}_{cm_1}-\boldsymbol{\rho}^{'}|)dl^{'} \quad \text{(C.10)}$$

Where $\hat{n}_f$ is the unit vector normal to the field segment. The typical elements of the sub-matrices $\mathrm{LM_Z}120, \mathrm{LM_Z}210$, and $\mathrm{LM_Z}220$ have similar form as (C.10).

$\mathbf{ZJ_Z111}$:

An element in the m^{th} row and the n^{th} column of the sub-matrix $\mathrm{ZJ_Z}111$ is the z-component of the electric field on the m^{th} segment of S_1, produced by $\mathrm{J_Z}$ on the n^{th} segment of S_1, when this $\mathrm{J_Z}$ radiates in the unbounded medium $(\epsilon_1, \mu_1, \gamma_1)$. This element is given by

$$\mathrm{ZJ_Z}111(m,n) = -\frac{\eta_{c_1} l_{m_1}}{8}\Big\{h_1 \int_{C_{n_1}} H_0^{(2)}(h_1|\boldsymbol{\rho}_{cm_1} - \boldsymbol{\rho}^{'}|)dl^{'} + h_2 \int_{C_{n_1}} H_0^{(2)}(h_2|\boldsymbol{\rho}_{cm_1} - \boldsymbol{\rho}^{'}|)dl^{'}\Big\} \quad \text{(C.11)}$$

Where, η_{c_1} is the wave impedance associated with the chiral medium $(\epsilon_1, \mu_1, \gamma_1)$ and is given by the following

$$\eta_{c_1} = \frac{\eta_1}{\sqrt{1 + (\eta_1\gamma_1)^2}}. \quad \text{(C.12)}$$

Here, $\eta_1 = \sqrt{\frac{\mu_1}{\epsilon_1}}$. The two wave number h_1 and h_2 associated with the chiral material $(\epsilon_1, \mu_1, \gamma_1)$ are given by the following

$$h_1 = \omega\mu_1\gamma_1 + \sqrt{(k_1)^2 + (\omega\mu_1\gamma_1)^2} \quad \text{(C.13)}$$

$$h_2 = -\omega\mu_1\gamma_1 + \sqrt{(k_1)^2 + (\omega\mu_1\gamma_1)^2} \quad \text{(C.14)}$$

Where,

$$k_1 = \omega\sqrt{\epsilon_1\mu_1}. \quad \text{(C.15)}$$

$\mathbf{ZJ_L111}$:

An element in the m^{th} row and the n^{th} column of the sub-matrix $\mathrm{ZJ_L}111$ is the z-component of the electric field on the m^{th} segment of S_1, produced by $\mathrm{J_L}$ on the n^{th} segment of S_1, when this $\mathrm{J_L}$ radiates in the unbounded medium $(\epsilon_1, \mu_1, \gamma_1)$. This element is approximately given by

$$\mathrm{ZJ_L}111(m,n) = \frac{\eta_{c_1} l_{m_1}}{8}\Big\{h_1 \int_{C_{n_1}} \Big(\hat{n}_1 \cdot \frac{(\boldsymbol{\rho}_{cm_1} - \boldsymbol{\rho}^{'})}{|\boldsymbol{\rho}_{cm_1} - \boldsymbol{\rho}^{'}|}\Big) H_1^{(2)}(h_1|\boldsymbol{\rho}_{cm_1} - \boldsymbol{\rho}^{'}|)dl^{'} - h_2 \int_{C_{n_1}} \Big(\hat{n}_1 \cdot \frac{(\boldsymbol{\rho}_{cm_1} - \boldsymbol{\rho}^{'})}{|\boldsymbol{\rho}_{cm_1} - \boldsymbol{\rho}^{'}|}\Big) H_1^{(2)}(h_2|\boldsymbol{\rho}_{cm_1} - \boldsymbol{\rho}^{'}|)dl^{'}\Big\} \quad \text{(C.16)}$$

$\mathbf{ZM_Z111}$:

An element in the m^{th} row and the n^{th} column of the sub-matrix $\mathrm{ZM_Z}111$ is the z-component of the electric field on the m^{th} segment of S_1, produced by $\mathrm{M_Z}$ on the n^{th} segment of S_1, when this $\mathrm{M_Z}$ radiates in the unbounded medium $(\epsilon_1, \mu_1, \gamma_1)$. This element is approximately given by

$$\mathrm{ZM_Z}111(m,n) = \frac{jl_{m_1}}{8}\Big\{h_1 \int_{C_{n_1}} H_0^{(2)}(h_1|\boldsymbol{\rho}_{cm_1} - \boldsymbol{\rho}^{'}|)dl^{'} - h_2 \int_{C_{n_1}} H_0^{(2)}(h_2|\boldsymbol{\rho}_{cm_1} - \boldsymbol{\rho}^{'}|)dl^{'}\Big\} \quad \text{(C.17)}$$

$\mathbf{ZM_L111}$:

An element in the m^{th} row and the n^{th} column of the sub-matrix $\mathrm{ZM_L}111$ is the z-component of the electric field on the m^{th} segment of S_1, produced by $\mathrm{M_L}$ on the n^{th} segment of S_1, when this $\mathrm{M_L}$ radiates in the unbounded medium $(\epsilon_1, \mu_1, \gamma_1)$. This element is approximately given by

$$\mathrm{ZM_L}111(m,n) = -\frac{jl_{m_1}}{8}\Big\{h_1 \int_{C_{n_1}} \Big(\hat{n}_1 \cdot \frac{(\boldsymbol{\rho}_{cm_1} - \boldsymbol{\rho}^{'})}{|\boldsymbol{\rho}_{cm_1} - \boldsymbol{\rho}^{'}|}\Big) H_1^{(2)}(h_1|\boldsymbol{\rho}_{cm_1} - \boldsymbol{\rho}^{'}|)dl^{'} + h_2 \int_{C_{n_1}} \Big(\hat{n}_1 \cdot \frac{(\boldsymbol{\rho}_{cm_1} - \boldsymbol{\rho}^{'})}{|\boldsymbol{\rho}_{cm_1} - \boldsymbol{\rho}^{'}|}\Big) H_1^{(2)}(h_2|\boldsymbol{\rho}_{cm_1} - \boldsymbol{\rho}^{'}|)dl^{'}\Big\} \quad \text{(C.18)}$$

$\mathbf{LJ_Z111}$:

An element in the m^{th} row and the n^{th} column of the sub-matrix $\mathrm{LJ_Z}111$ is the lateral component of the electric field on the m^{th} segment of S_1, produced by $\mathrm{J_Z}$ on the n^{th} segment of S_1, when this $\mathrm{J_Z}$ radiates in the unbounded medium $(\epsilon_1, \mu_1, \gamma_1)$. This element is approximately given by

$$\mathrm{LJ_Z}111(m,n) = -\frac{\eta_{c_1} l_{m_1}}{8}\Big\{h_1 \int_{C_{n_1}} \Big(\hat{n}_f \cdot \frac{(\boldsymbol{\rho}_{cm_1} - \boldsymbol{\rho}^{'})}{|\boldsymbol{\rho}_{cm_1} - \boldsymbol{\rho}^{'}|}\Big) H_1^{(2)}(h_1|\boldsymbol{\rho}_{cm_1} - \boldsymbol{\rho}^{'}|)dl^{'} - h_2 \int_{C_{n_1}} \Big(\hat{n}_f \cdot \frac{(\boldsymbol{\rho}_{cm_1} - \boldsymbol{\rho}^{'})}{|\boldsymbol{\rho}_{cm_1} - \boldsymbol{\rho}^{'}|}\Big) H_1^{(2)}(h_2|\boldsymbol{\rho}_{cm_1} - \boldsymbol{\rho}^{'}|)dl^{'}\Big\} \quad \text{(C.19)}$$

$\mathbf{LJ_L111}$:

An element in the m^{th} row and the n^{th} column of the sub-matrix $\mathrm{LJ_L}111$ is the lateral component of the electric field on the m^{th} segment of S_1, produced by $\mathrm{J_L}$ on the n^{th} segment of S_1, when this $\mathrm{J_L}$ radiates in the unbounded medium $(\epsilon_1, \mu_1, \gamma_1)$. This element is approximately given by

$$\begin{aligned}
\mathrm{LJ_L}111(m,n) &= -\frac{\eta_{c_1} l_{m_1}}{8}(\hat{t}_{n_1} \cdot \hat{t}_{m_1}) \\
&\times \Big\{ h_1 \int_{C_{n_1}} H_0^{(2)}(h_1|\boldsymbol{\rho}_{cm_1} - \boldsymbol{\rho}^{'}|)dl^{'} + h_2 \int_{C_{n_1}} H_0^{(2)}(h_2|\boldsymbol{\rho}_{cm_1} - \boldsymbol{\rho}^{'}|)dl^{'} \Big\} \\
&- \frac{\eta_{c_1}}{8l_{n_1}} \Big\{ h_1^{-1} \int_{\left[C_{n_1-\frac{1}{2}} + C_{n_1+\frac{1}{2}}\right]} H_0^{(2)}(h_1|\boldsymbol{\rho}_{cm_1+} - \boldsymbol{\rho}^{'}|)dl^{'} \\
&+ h_2^{-1} \int_{\left[C_{n_1-\frac{1}{2}} + C_{n_1+\frac{1}{2}}\right]} H_0^{(2)}(h_2|\boldsymbol{\rho}_{cm_1+} - \boldsymbol{\rho}^{'}|)dl^{'} \Big\} \\
&+ \frac{\eta_{c_1}}{8l_{n_1}} \Big\{ h_1^{-1} \int_{\left[C_{n_1-\frac{1}{2}} + C_{n_1+\frac{1}{2}}\right]} H_0^{(2)}(h_1|\boldsymbol{\rho}_{cm_1-} - \boldsymbol{\rho}^{'}|)dl^{'} \\
&+ h_2^{-1} \int_{\left[C_{n_1-\frac{1}{2}} + C_{n_1+\frac{1}{2}}\right]} H_0^{(2)}(h_2|\boldsymbol{\rho}_{cm_1-} - \boldsymbol{\rho}^{'}|)dl^{'} \Big\} \quad \text{(C.20)}
\end{aligned}$$

$\mathbf{LM_Z111}$:

An element in the m^{th} row and the n^{th} column of the sub-matrix $\mathrm{LM_Z}111$ is the lateral component of the electric field on the m^{th} segment of S_1, produced by $\mathrm{M_Z}$ on the n^{th} segment of S_1, when this $\mathrm{M_Z}$ radiates in the unbounded medium $(\epsilon_1, \mu_1, \gamma_1)$. This element is approximately given by

$$\begin{aligned}
\mathrm{LM_Z}111(m,n) &= \frac{j l_{m_1}}{8} \Big\{ h_1 \int_{C_{n_1}} \Big(\hat{n}_f \cdot \frac{(\boldsymbol{\rho}_{cm_1} - \boldsymbol{\rho}^{'})}{|\boldsymbol{\rho}_{cm_1} - \boldsymbol{\rho}^{'}|} \Big) H_1^{(2)}(h_1|\boldsymbol{\rho}_{cm_1} - \boldsymbol{\rho}^{'}|)dl^{'} \\
&+ h_2 \int_{C_{n_1}} \Big(\hat{n}_f \cdot \frac{(\boldsymbol{\rho}_{cm_1} - \boldsymbol{\rho}^{'})}{|\boldsymbol{\rho}_{cm_1} - \boldsymbol{\rho}^{'}|} \Big) H_1^{(2)}(h_2|\boldsymbol{\rho}_{cm_1} - \boldsymbol{\rho}^{'}|)dl^{'} \Big\} \quad \text{(C.21)}
\end{aligned}$$

$\mathbf{LM_L111}$:

An element in the m^{th} row and the n^{th} column of the sub-matrix $\mathrm{LM_L}111$ is the lateral component of the electric field on the m^{th} segment of S_1, produced by $\mathrm{M_L}$ on the n^{th} segment of S_1, when this $\mathrm{M_L}$ radiates in the unbounded medium $(\epsilon_1, \mu_1, \gamma_1)$. This element is approximately given by

$$\begin{aligned}
\mathrm{LM_L}111(m,n) = -\frac{jl_{m_1}}{8}(\hat{t}_{n_1}\cdot\hat{t}_{m_1})\Big\{h_1\int_{C_{n_1}} H_0^{(2)}(h_1|\boldsymbol{\rho}_{cm_1}-\boldsymbol{\rho}^{'}|)dl^{'} \\
- h_2\int_{C_{n_1}} H_0^{(2)}(h_2|\boldsymbol{\rho}_{cm_1}-\boldsymbol{\rho}^{'}|)dl^{'}\Big\} \\
+\frac{j}{8l_{n_1}}\Big\{h_1^{-1}\int_{\left[C_{n_1-\frac{1}{2}}+C_{n_1+\frac{1}{2}}\right]} H_0^{(2)}(h_1|\boldsymbol{\rho}_{cm_1+}-\boldsymbol{\rho}^{'}|)dl^{'} \\
+h_2^{-1}\int_{\left[C_{n_1-\frac{1}{2}}+C_{n_1+\frac{1}{2}}\right]} H_0^{(2)}(h_2|\boldsymbol{\rho}_{cm_1+}-\boldsymbol{\rho}^{'}|)dl^{'}\Big\} \\
-\frac{j}{8l_{n_1}}\Big\{h_1^{-1}\int_{\left[C_{n_1-\frac{1}{2}}+C_{n_1+\frac{1}{2}}\right]} H_0^{(2)}(h_1|\boldsymbol{\rho}_{cm_1-}-\boldsymbol{\rho}^{'}|)dl^{'} \\
+h_2^{-1}\int_{\left[C_{n_1-\frac{1}{2}}+C_{n_1+\frac{1}{2}}\right]} H_0^{(2)}(h_2|\boldsymbol{\rho}_{cm_1-}-\boldsymbol{\rho}^{'}|)dl^{'}\Big\} \quad \text{(C.22)}
\end{aligned}$$

The elements in the sub-matrices in the last two rows of the moment matrix of (3.9) contain the fields computed in the unbounded chiral medium $(\epsilon_2, \mu_2, \gamma_2)$, when these fields are radiated by surface currents $(\mathbf{J}_2, \mathbf{M}_2)$. The expressions for such elements are similar to those in $(\mathrm{C.11}-\mathrm{C.22})$. For example,

$$\begin{aligned}
\mathrm{ZJ_Z}222(m,n) = -\frac{\eta_{c_2}l_{m_2}}{8}\Big\{h_3\int_{C_{n_2}} H_0^{(2)}(h_3|\boldsymbol{\rho}_{cm_2}-\boldsymbol{\rho}^{'}|)dl^{'} \\
+h_4\int_{C_{n_2}} H_0^{(2)}(h_4|\boldsymbol{\rho}_{cm_2}-\boldsymbol{\rho}^{'}|)dl^{'}\Big\} \quad \text{(C.23)}
\end{aligned}$$

Where, η_{c_2} is the wave impedance associated with the chiral medium $(\epsilon_2, \mu_2, \gamma_2)$ and is given by the following

$$\eta_{c_2} = \frac{\eta_2}{\sqrt{1+(\eta_2\gamma_2)^2}}. \quad \text{(C.24)}$$

Here, $\eta_2 = \sqrt{\frac{\mu_2}{\epsilon_2}}$. The two wave number h_3 and h_4 associated with the chiral

material $(\epsilon_2, \mu_2, \gamma_2)$ are given by the following

$$h_3 = \omega\mu_2\gamma_2 + \sqrt{(k_2)^2 + (\omega\mu_2\gamma_2)^2} \tag{C.25}$$

$$h_4 = -\omega\mu_2\gamma_2 + \sqrt{(k_2)^2 + (\omega\mu_2\gamma_2)^2} \tag{C.26}$$

Where,

$$k_2 = \omega\sqrt{\epsilon_2\mu_2}. \tag{C.27}$$

SCATTERING FROM A CHIRAL CYLINDER OF ARBITRARY CROSS-SECTION ABOVE A GROUND PLANE

ORIJINALLIK RAPORU

%13	%7	%11	%1
BENZERLIK ENDEKSI	İNTERNET KAYNAKLARI	YAYINLAR	ÖĞRENCI ÖDEVLERI

BIRINCIL KAYNAKLAR

1	M.A. Al-Kanhal, E. Arvas. "Electromagnetic scattering from a chiral cylinder of arbitrary cross section", IEEE Transactions on Antennas and Propagation, 1996 Yayın	%3
2	Jian-Ming Jin. "Theory and Computation of Electromagnetic Fields", Wiley, 2010 Yayın	<%1
3	www.dtic.mil İnternet Kaynağı	<%1
4	www.jpier.org İnternet Kaynağı	<%1
5	Submitted to Eastern Mediterranean University Öğrenci Ödevi	<%1
6	E. Arvas, Y. Qian, A. Sadigh, T.K. Sarkar, F. Aslan. "E-Field and H-Field Solutions of TE Scattering from Multiple Conducting and Dielectric Cylinders of Arbitrary Cross-Section",	<%1